HOPPING OF AN IMPURITY DEFECT IN ION CRYSTALS IN LINEAR TRAPS

by

Jixin Liang
B.Sc., Sun Yet-Sen University, 2008

THESIS SUBMITTED IN PARTIAL FULFILLMENT

OF THE REQUIREMENTS FOR THE DEGREE OF

MASTER OF SCIENCE

IN THE

DEPARTMENT OF PHYSICS

Faculty of Science

SIMON FRASER UNIVERSITY
Spring 2012

APPROVAL

Name:	Jixin Liang
Degree:	Master of Science
Title of Thesis:	Hopping of an Impurity Defect in Ion Crystals in Linear Traps
Examining Committee:	Dr. J. Steven Dodge Associate Professor (Chair)
	Dr. Paul C. Haljan Senior Supervisor Associate Professor
	Dr. Mike Hayden Supervisor Professor
	Dr. Jeffrey McGuirk Supervisor Assistant Professor
	Dr. Malcolm Kennett Internal Examiner Associate Professor
Date Approved:	December 1, 2011

Partial Copyright Licence

Abstract

Ordered arrays of laser-cooled, trapped ions or "ion crystals" are a novel form of matter with a rich variety of equilibrium structures and dynamics. In this thesis, we investigate the hopping mobility of a $^{172}Yb^{+}$ impurity ion within a crystal of $^{171}Yb^{+}$ ions, confined in a linear Paul trap. The site-to-site hopping of the impurity ion, distinguished by a lack of fluorescence, is studied as a function of the $^{171}Yb^{+}$ laser-cooling parameters and of the anisotropy of the trapping potential. The onset of rapid hopping is found to occur when average thermal energies become comparable to the Coulomb potential energy. Furthermore, the hopping rate is enhanced at trap anisotropies near the critical value for the structural phase transition to a two-dimensional zigzag phase. The impurity ion has the highest hopping mobility near the centre of the crystal, which may be intrinsic to the crystal structure and dynamics near the zigzag transition. Simplified molecular-dynamics simulations reproduce several features of the experimental results.

To my parents, my aunt and my girlfriend.

Acknowledgments

I would like to thank all the people who have helped me in my Master's degree.

My deepest gratitude goes to my supervisor, Dr. Paul C. Haljan, who spent countless hours guiding me through different phases of the research and ultimately made this thesis possible. I can always find encouragement and inspiration from his optimistic and insightful advice. Besides his profound knowledge, his patience is another quality that I am willing to spend my life learning. I am truly grateful to have such a warm and approachable mentor.

I would like to thank my committee members: Dr. Mike Hayden and Dr. Jeffrey McGuirk, for giving me very useful suggestions during the course of my Master's and spending their valuable time reading my thesis. My gratitude also goes to Dr. Malcolm Kennett, who gladly agreed to correct my thesis despite his busy schedule. I also want to thank Dr. J. Steven Dodge, for his friendly advice and for his work in organizing my thesis examination.

Special thanks go to my colleague, Sara Ejtemaee, for making our lab such a warm and nice place to work in.

I really cherish the friendship with Yiwei Zhang, Zhiwei Deng and Wen Huang, for the joys, the fun and the comfort they have provided.

Lastly, I wish to thank my parents, my aunt, and my girlfriend, for giving me unconditional love and support. I cannot imagine how dim life would be without all your encouraging words. Thank you for giving the irreplaceable meaning to every bit of my effort.

Contents

List of Figures

Chapter 1

Introduction

Since the advent of laser cooling, ordered arrays of cold, trapped atomic ions, or "ion crystals", have been realized in both radio-frequency (rf) Paul traps [1, 2] and Penning traps [3]. Applications include precision spectroscopy [4], quantum information processing [4, 5, 6] and quantum simulations of spin systems [7, 8]. The equilibrium crystal structure [9] has been studied both experimentally [2, 10, 11, 12] and theoretically [13, 14] as a function of ion number and trap parameters, and various crystal configurations have been identified [10]. For the specific example of a linear Paul trap [11, 15], strong transverse confinement aligns the ions into a linear crystal. Reducing the trap anisotropy induces a structural phase transition to a two-dimensional zigzag configuration, which grows first at the centre of the crystal where the ion density and Coulomb pressure are highest. A power-law scaling with the number of ions for the critical anisotropy at which the zigzag transition occurs has been predicted [13, 14] and measured experimentally [15].

Beginning with the earliest observations of ion crystals, the *dynamics* of crystallization and of the reverse transition to a disordered cloud phase have also been studied as a function of laser cooling and rf trap parameters [1, 16, 17, 18, 19]. The interplay between the nonlinearity due to Coulomb interactions and ion micro-motion arising from the rf potential gives rise to rf heating and chaotic motion. These effects have been investigated for two ions in the approach to the crystalline phase [16, 18], and in melting of two-ion crystals via an order-chaos transition [17, 19] near the Mathieu stability limit of the rf trap [20]. (For a summary of these experiments, see Ref. [18].) More recently, the thermally activated hopping dynamics for two ions in a double well has also been observed [21]. The Coulomb

barrier to hopping in this case is weak and regulated by a slight asymmetry in the trap, while the thermal energy is regulated by adjusting laser-cooling and -heating rates.

Building on the studies with two ions in Ref. [21], we investigate site-to-site hopping in linear crystals of multiple $^{171}Yb^{+}$ ions by introducing a single distinguishable impurity defect [2]. Tracking the trajectory of the impurity, we measure the hopping as a function of the $^{171}Yb^{+}$ laser cooling parameters and as a function of trap anisotropy, which strongly modifies the crystal dynamics near the zigzag transition [15, 22, 23]. For this first set of experiments, a $^{172}Yb^{+}$ isotope is chosen for the impurity to have a nearly identical mass [24]. The hopping dynamics, which are a prelude to full melting, are distinguished from the prior studies of the order-disorder transition in that the ion crystal appears well-localized during the majority of the hopping evolution.

The experimental results of this thesis have been previously published in Ref. [25]. The expanded discussion in the following chapters, which provide additional theoretical and experimental background information as well as some preliminary numerical simulations related to the hopping experiments, is organized as follows:

Chapter 2 provides theoretical background to the various aspects of the experiment. In the experiment, control of the trap voltages and the laser parameters enables us to investigate the hopping dynamics of ion crystals with different potential and kinetic energies. With this in mind, we first present a discussion of the ion trap and then consider the Coulomb interaction between multiple ions in the trap. This allows us to see that ion crystals with different structures can occur in a linear rf Paul trap and sets the stage for our studies of hopping dynamics near the zigzag structural phase transition. A summary of Doppler-cooling theory motivates our use of the power and detuning of a cooling laser to control the temperature of the ions in the hopping experiments.

Chapter 3 summarizes the technical implementation of the experiment. In particular, we emphasize the calibration of the confining potential, the setup of different lasers together with their sidebands, and the setup of the imaging system used to monitor the hopping dynamics of the ion crystals. A brief description of the experimental procedure is provided at the end of the chapter to outline how the hopping data is acquired.

Chapter 4 discusses the results of the experiment. We first develop an automatic way to extract the hopping trajectory of an impurity ion in the crystal. From the trajectory, various statistics describing different aspects of the hopping behaviour can be obtained,

such as hopping rate and destination. We then describe measurements of the hopping rate of the impurity as a function of laser power, laser detuning and trap anisotropy. Finally, we discuss several technical issues that can complicate our experiment but argue that some of the features of the hopping behaviour are likely to be intrinsic to the ion crystal itself and so of fundamental interest.

Chapter 5 presents the results of a simple version of molecular-dynamics simulation to aid in the interpretation of our experimental results. The simulations omit all technical aspects of the experiment and simply consider an ion crystal evolving with constant energy in a two-dimensional harmonic trap. We show that the results of these simple simulations reproduce important features of the observed hopping behaviour, consistent with our argument that they are intrinsic to the crystal structure and dynamics.

Finally, in the conclusions we discuss some possible future experiments motivated by these first hopping studies. The experience and techniques that we have acquired should also prove useful in pursuing other types of experiments near the zigzag transition. In fact, the structural phase transition has attracted a fair amount of theoretical attention in the past few years with proposals being put forward for the observation of the temperature dependence of the transition [26], the nucleation of structural "kink" defects in a zigzag chain [27, 28], and simulations of model quantum systems [29, 27].

Chapter 2

Theory

In this chapter, we review various theoretical concepts needed to understand the equilibrium structure of arrays of atomic ions, or "ion crystals", in a linear ion trap and the concepts needed to understand the dynamics of the crystal, including site-to-site hopping. In Sec. 2.1, we first describe the trap-ion interaction for a single ion in a linear rf Paul trap, and describe how the combination of static and oscillating electric fields generates a nominally harmonic confining potential in all three dimensions. In Sec. 2.2, we discuss how ion-ion interactions, together with the confining potential, determine the equilibrium structure of a multi-ion crystal. In particular, we are interested in the structural phase transition from a linear ion crystal to a two-dimensional zigzag pattern and the onset of the transition at a critical trap anisotropy. In Sec. 2.2, we summarize the small-oscillation dynamics of the crystal near equilibrium and review an alternate interpretation of the zigzag phase transition, which is associated with the frequency of the transverse zigzag vibrational mode going to zero.

In a hopping event, which far exceeds the limit of small oscillations, ions with enough energy can overcome the restoring forces of their local equilibrium and swap positions with each other. For a given equilibrium configuration, the confining potential and the Coulomb interactions between individual ions together set the potential barrier that the ions need to overcome in a hopping event. Near the zigzag transition, one might expect the hopping behaviour to be affected due to the change in crystal structure and dynamics.

The kinetic energy, which represents the energy available for the ions to surmount the potential barrier, is discussed in the final section, Sec. 2.3. By summarizing the Doppler

laser-cooling technique, we see that the kinetic energy can be controlled by the power and detuning of an applied cooling laser.

2.1 Ion-trap theory

Successful confinement of charged particles, including atomic ions such as Yb^+, needs to surmount the following basic problem, often referred to as Earnshaw's Theorem [30]. According to Gauss's law, there is no local minimum of potential in a three-dimensional (3-D) static electric field in a region free of charge; therefore, one cannot confine an ion by using static electric fields only. Two common solutions are proposed for ion trapping [30]. One is the Penning trap, where a homogeneous static magnetic field and an inhomogeneous static electric field are used to confine the ion. The other solution, called the Paul trap, uses a combination of static and oscillating inhomogeneous electric fields to provide confinement of an ion in three-dimensional space. The experiment we perform is based on a trap of this kind and, for an atomic ion, the trap operates with oscillating electric fields typically at radio frequency (rf).

The ion trap used in this experiment [31] is a millimeter-scale linear rf Paul trap [11, 32, 33] composed of four rods in a square configuration and two end-cap electrodes, as shown in Fig. 2.1. Two opposing rods are rf-grounded and the other two are driven at voltage $V_0 \cos \Omega t$. These four rods together confine the ion transversely, while the axial confinement comes from the two end-caps at potential U_0. For convenience, we use the trap centre as the origin, and let the z direction lie along the axial direction of the trap. We also set the transverse x and y directions to lie along the diagonals of the square configuration of the rods (see Fig. 2.1). Near the centre of the trap, the electric field can be expressed as follows [34, 20]:

$$\vec{E}(x,y,z,t) = -V_0 \left(\frac{x\hat{x} - y\hat{y}}{R'^2} \right) \cos(\Omega t) - \frac{\kappa U_0}{z_0^2} (2z\hat{z} - x\hat{x} - y\hat{y}). \tag{2.1}$$

Here, $\Omega/2\pi$ is the rf frequency ($\Omega/2\pi = 30$ MHz in our experiment); R' is an effective distance that is approximately the nearest distance from the trap axis to the surface of the rods; z_0 is half of the distance between the two endcaps; and κ (≤ 1) is a geometrical factor.

The equation above describes the electric field for a symmetric, square configuration of the rods, but in practice the coefficients for the x– and y–related terms are slightly different,

breaking the symmetry of the transverse confinement. Other real-life imperfections include different rf phases on the rods, imperfect rf-grounding, and an rf component in the axial direction, which are typically small effects. One can also dc-bias the rods, which adds more terms to Eqn. (2.1), but in practice these terms are close to zero and we ignore them here in this simplified discussion.

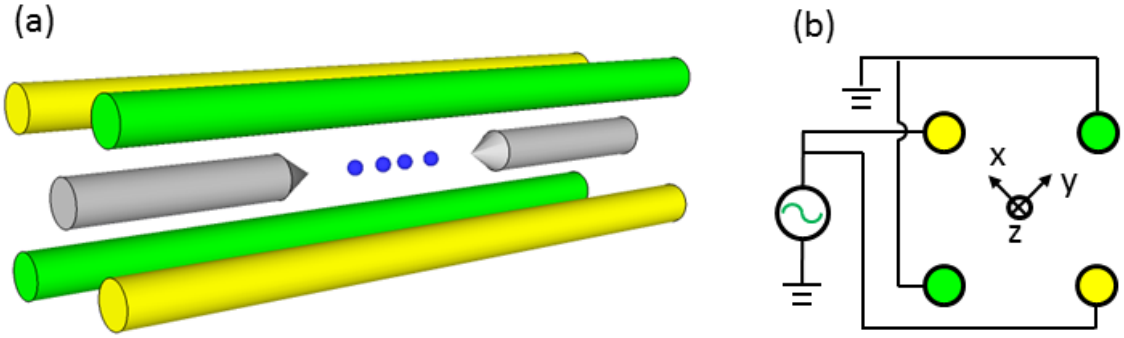

Figure 2.1: (a) Three-dimensional sketch of a linear rf Paul trap, composed of four rods and two end-cap needles. (b) A cross section of the four rods with electrical connections. Two opposing rods are rf-grounded and the other two are driven at voltage $V_0 \cos \Omega t$. Also shown is the coordinate system used in the trap discussion (see text).

In the presence of the electric field of Eqn. (2.1), an ion in the trap undergoes motion which can be described by the Mathieu equation as follows,

$$\ddot{u}_i + [a_i + 2q_i \cos(\Omega t)] \frac{\Omega^2}{4} u_i = 0, \tag{2.2}$$

where u_i is one of the three components of the ion's position, and

$$a_x = a_y = -\frac{a_z}{2} = -\frac{4\kappa U_0 q}{m z_0^2 \Omega^2}, \tag{2.3}$$

$$q_x = -q_y = \frac{2V_0 q}{m R'^2 \Omega^2}, q_z = 0, \tag{2.4}$$

and q and m are the charge and mass of the ion respectively. In the case of $|a_i| \ll 1$ and $|q_i| \ll 1$, the Mathieu equation has a first order solution,

$$u_i(t) \approx u_{0i} \cos(\omega_i t + \varphi_{Si})[1 + \frac{q_i}{2} \cos(\Omega t)], \tag{2.5}$$

where

$$\omega_i \approx \frac{1}{2}\Omega\sqrt{a_i + \frac{1}{2}q_i^2}. \tag{2.6}$$

Here, φ_{Si} is determined by the initial condition. From Eqn. (2.5), we can see that the main part of the ion's motion is a three-dimensional oscillation with "secular" frequency ω_i in the i^{th} direction. In practice, the frequencies in the transverse directions (x and y) are primarily determined by Ω and V_0, and $\omega_{x,y} \approx |q_{x,y}|\Omega/\sqrt{8}$. In the axial direction, $q_z \approx 0$ and the secular frequency is primarily determined by the end-cap voltages for the trap parameters considered in this thesis. In practice, the symmetry of the transverse confinement is also broken due to trap asymmetries and dc voltages applied to the rods. On top of the secular oscillation, there is a fast oscillation at radio frequency with a smaller amplitude $u_{0i}q_i/2$, which is commonly called "micro-motion". Although smaller in amplitude, micro-motion usually has roughly the same contribution as the secular motion to the kinetic energy of the ion, and is simultaneously reduced along with the secular motion by cooling. However, excess micro-motion arises if the ion deviates from the rf null along the trap axis, as well as for other reasons [34]. For a linear crystal of several ions and of moderate size, all the ions can be made to lie along the rf null of the linear ion trap. This is, in fact, one of the main reasons for the popularity of the linear Paul trap in quantum computing applications with trapped ions. For 2-D configurations of the ion crystal such as the zigzag configuration, excess micro-motion is unavoidable. The effects of micro-motion, for example on heating in the trap and on laser cooling, have been studied in detail – see the discussion in [6] and references therein; however, in understanding the properties of (near) 1-D ion crystals in linear rf Paul traps, it is common to ignore the micro-motion and only consider the secular motion in the time-averaged pseudo-potential. We do the same in the following sections, but return to discuss possible effects of micro-motion later in the thesis after the presentation of the experimental results.

2.2 Ion crystals in a linear trap

2.2.1 Equilibrium crystal structure

If ions in an ion trap are sufficiently laser cooled such that their kinetic energy is reduced below the typical Coulomb interaction energy, the ions can crystallize into an array [1, 2,

3]. For the common configuration of a linear Paul trap, the axial confinement is usually weak, and the stronger transverse confinement aligns the ions into a linear crystal along the axial direction (see Fig. 2.2) [11, 15]. For harmonic confinement, the array is non-uniform with the highest linear density at the centre of the crystal. As one strengthens the axial confinement or equivalently reduces the transverse strength, the anisotropy of the trap potential is reduced. Lower than a certain threshold of anisotropy, the linear configuration of the crystal will no longer have the lowest energy, and one expects a structural phase transition into a two-dimensional zigzag pattern [13], which will lie in a plane defined by the axial direction and the transverse direction with weakest confinement. (Normally the term "phase transition" is reserved for a physical system with $N \to \infty$ particles; however, we follow the literature cited above and describe the transition between configurations of an ion crystal with low numbers of ions ($N \lesssim 10$) as a phase transition.) As will be discussed in Chp. 3, the transverse principal axes of the pseudo-potential in our trap happen to coincide with the x and y directions defined in Sec. 2.1, and we choose the y-direction to correspond to the weaker transverse direction.

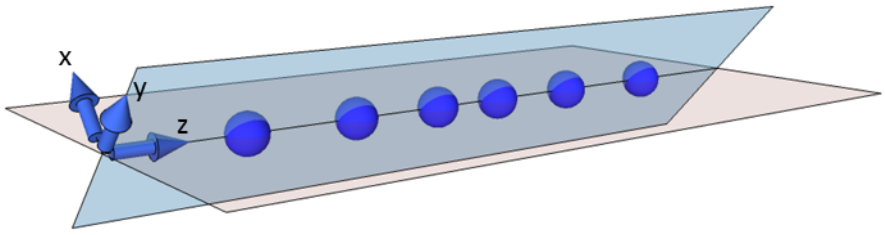

Figure 2.2: Sketch of a 1-D ion crystal in a linear Paul trap and coordinate system. The blue-colored plane is the $y-z$ plane defined in Fig. 2.1 and makes an angle of 45° with the horizontal plane (red).

We now review the theory of equilibrium structures for N ions in a linear Paul trap [13] and the onset of the zigzag transition with respect to trap anisotropy. We consider the pseudo-potential and determine the equilibrium configuration from the potential energy only. In other words, we ignore the effect of thermal fluctuations, which suppress the onset of the zigzag transition [26]. (A discussion of the thermal effect is provided in Chp. 4). For simplicity, we consider the crystal only in the $y-z$ plane. Assuming all N ions have the

same mass m and charge q, the potential energy E_p of the ion-crystal is described by

$$E_p(\mathbf{r}_1,\mathbf{r}_2,\ldots,\mathbf{r}_N) = \frac{m}{2}\sum_{n=1}^{N}(\omega_y^2 y_n^2+\omega_z^2 z_n^2)+\frac{1}{2}\frac{q^2}{4\pi\varepsilon_0}\sum_{n,m=1;m\neq n}^{N}\frac{1}{|\mathbf{r}_n-\mathbf{r}_m|}. \tag{2.7}$$

Here, $\mathbf{r}_i = (y_i, z_i)$ denotes the position vector of the i^{th} ion, and ω_y and ω_z denote the secular trap frequencies in the corresponding directions. The first sum in the above equation gives the energy due to the trap's potential, while the second sum comes from the ion-ion interactions. The factor of $1/2$ in the latter term accounts for double-counting of the ions.

After re-scaling the ions' positions with the unit length $a_0 = (q^2/4\pi\varepsilon_0 m\omega_y^2)^{1/3}$, the potential energy becomes

$$E_p = \frac{E_0}{2}\left[\sum_{n=1}^{N}({y'_n}^2+\alpha {z'_n}^2)+\sum_{n,m=1 m\neq n}^{N}\frac{1}{|\mathbf{r}_n{}'-\mathbf{r}_m{}'|}\right], \tag{2.8}$$

with $E_0 = q^2/4\pi\varepsilon_0 a_0 = (m\omega_y^2)^{\frac{1}{3}}(q^2/4\pi\varepsilon_0)^{\frac{2}{3}}$, while y',z' and $\mathbf{r}'$ are the coordinates divided by a_0. The parameter $\alpha = (\omega_z/\omega_y)^2$ is related to the anisotropy of the trap. Note here that higher anisotropy has lower α, as historically defined [13]. It is clear from the scaled expression above that the equilibrium structure and the transition between linear and 2-D zigzag structure only depends on α, which represents the control parameter for the zigzag transition.

The critical anisotropy parameter, α_{crit}, at which an ion crystal undergoes the transition from a 1-D to 2-D structure, depends on the number of ions, N. For $N = 2$, the crystal is aligned along the z-direction for $\omega_y > \omega_z$ (that is, for $\alpha < 1$), while for $N = 3$, the crystal is linear 1-D for $\alpha \leq 1/3$, above which the central ion displaces transversely to form a zigzag structure. For $N \geq 4$, the equilibrium structure of the crystal needs to be calculated numerically for a given α. Figure 2.3 shows the simulation result from Maple software for a seven-ion crystal in the $y-z$ plane. The equilibrium structure is calculated by minimizing the total potential energy. The value of α increases from Fig. 2.3(a) to (c), and we can see that the corresponding lowest-energy configuration changes from a linear crystal to a 2-D zigzag pattern. As can be seen, the structural transition first happens at the centre of crystal. This is where the ion density and axial Coulomb pressure are highest and where the linear configuration is easiest to break. The peak-to-peak magnitude of the transverse displacement, dy_{pp}, as indicated in the figure, corresponds to the order parameter for the structural phase transition.

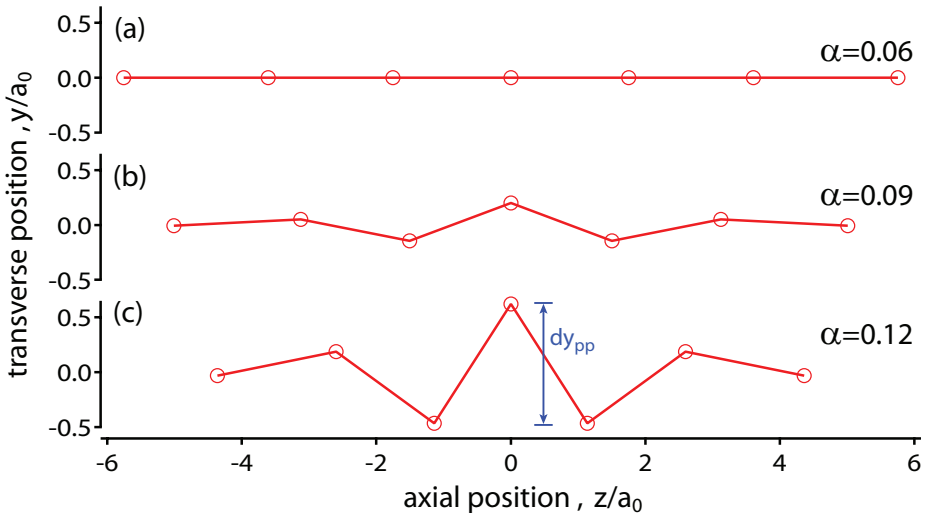

Figure 2.3: Numerical simulation of the equilibrium structure for a seven-ion crystal at different values of $\alpha = (\omega_z/\omega_y)^2$ as indicated. Lengths are scaled to characteristic length scale a_0 (see text).

A power-law dependence for α_{crit} on N was first theoretically predicted by Schiffer [13] and Dubin [14] as follows:

$$\alpha_{\text{crit}} = cN^{\beta}. \tag{2.9}$$

The power law behaviour has been confirmed experimentally by Enzer *et al.* [15], whose measured values of c and β were determined to be 3.23(6) and -1.83(4) in reasonable agreement with theory. The scaling with N can be qualitatively understood as follows: a larger number of ions gives a higher density and higher axial Coulomb pressure at the centre of a linear crystal. Because of the higher axial pressure, it is easier for the ions at the centre of the crystal to displace transversely at lower α (higher anisotropy). Calculated in Maple, Fig. 2.4 shows the transverse separation, dy_{pp}, of the centre two ions in a pure crystal of 5, 6 and 7 ions as a function of anisotropy parameter α. The values of dy_{pp}, which are obtained from the numerically determined equilibrium configurations at each value of α, show the characteristic rapid onset of the zigzag transition near a critical value of α. The critical values estimated from the plot are 0.1603, 0.1158, and 0.0883 for $N = 5$, 6 and 7 respectively, roughly matching the power law prediction of 0.170, 0.122, and 0.092.

In our experiments, we use an impurity defect to be able to observe hopping in a crys-

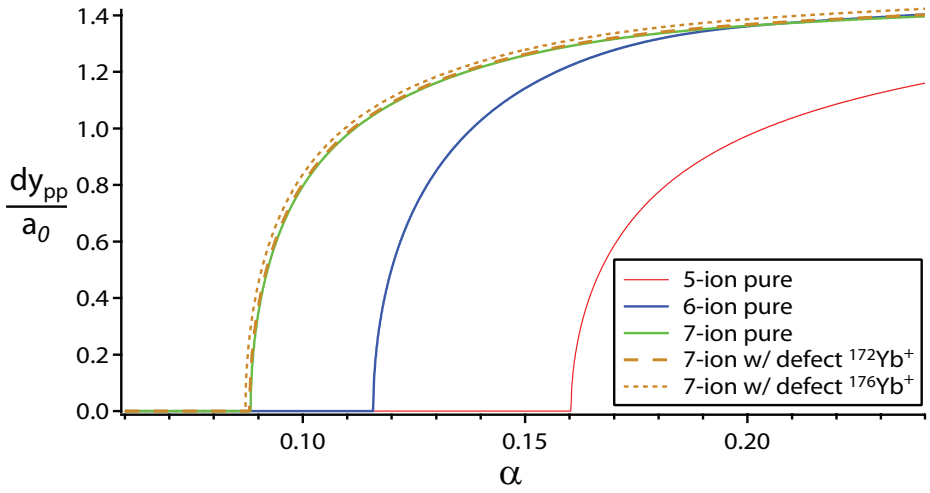

Figure 2.4: Theoretically calculated peak-to-peak zigzag displacement as a function of α for crystals with different numbers of ions and with or without an isotopic impurity (see legend). The critical values of α for pure crystals with 5, 6, and 7 $^{171}Yb^{+}$ ions are 0.1603, 0.1158, and 0.0883. Critical values for the 7-ion crystal change to 0.0880, and to 0.0871 when the central ion is replaced by $^{172}Yb^{+}$ and $^{176}Yb^{+}$, respectively.

tal of $^{171}Yb^{+}$ ions. Since we study how the hopping turns on near the structural phase transition, it is worth considering the effect of the impurity on the structural phase transition itself. The impurity that we use in the experiment is a $^{172}Yb^{+}$ ion, which experiences the same dc potential in the axial direction as the $^{171}Yb^{+}$ ions. However, the different mass of the impurity affects the time-averaged pseudo-potential the impurity experiences in the transverse direction and, for a larger mass, the strength of the pseudo-potential is reduced slightly. The long-dash line in Fig. 2.4 shows the zigzag transition when the $^{172}Yb^{+}$ impurity is present at the centre of a seven-ion crystal. The larger mass of the impurity shifts the onset of the transition towards lower α ($\alpha_{\text{crit}} = 0.0880$), but the shift is extremely small compared to the case of the pure crystal because of the small difference in mass. If the impurity is located at an outer site of the crystal, it has even less of an effect. To show the effect more clearly, we can consider the situation if we choose $^{176}Yb^{+}$ as the defect. The corresponding curve (the short-dashed line) is more clearly shifted downward ($\alpha_{\text{crit}} = 0.0871$ with the defect at the centre).

2.2.2 Collective vibrational modes near the zigzag transition

The structural phase transition can be viewed from a different perspective related to the collective vibrational modes of the crystal. We briefly review this approach from Ref. [15]. A discussion of the collective modes also serves to provide some background concepts that we will refer to in later chapters.

We study the simple case of pure crystals only and assume each of the N ions is undergoing small oscillations about its equilibrium position so that $y_i = \overline{y_i} + \eta_i$ and $z_i = \overline{z_i} + \zeta_i$ for $i = 1, 2, \ldots, N$. Here, $\overline{y_i}$ and $\overline{z_i}$ denote the equilibrium position for the i^{th} ion, and η_i and ζ_i are small displacements compared to the typical ion spacing in the crystal. The potential energy in Eqn. (2.7) can be expanded at the equilibrium configuration as follows:

$$E_p = E_{p,eq} + \frac{1}{2}\left(\sum_{n=1}^{N} \eta_n \frac{\partial}{\partial y_n} + \sum_{m=1}^{N} \zeta_m \frac{\partial}{\partial z_m}\right)^2 E_p|_{eq}. \tag{2.10}$$

The first order terms are omitted since they are zero at equilibrium, and the derivatives are assumed to be evaluated at the equilibrium position. For the region where $\alpha < \alpha_{\text{crit}}$, the crystal adopts a linear configuration, and so $\overline{y_i} = 0$ for all ions. In this specific case,

the cross terms proportional to $\eta_n \zeta_m$ are zero, which implies that the transverse and axial motions are decoupled.

The details of small-oscillation analysis for linear, 1-D crystals have been considered extensively in the literature [35, 36, 22]. One finds that the axial and transverse modes are closely related, and the corresponding modes in the two directions have matching eigenvectors and mode frequencies that are related by the following:

$$\frac{\omega_y^{(p)}}{\omega_y} = \sqrt{1 - \frac{\alpha}{2}\left[\left(\frac{\omega_z^{(p)}}{\omega_z}\right)^2 - 1\right]}, \qquad \omega_z^{(p)} \geq \omega_z \tag{2.11}$$

where ω_z and ω_y are the secular trap frequencies in the axial and transverse directions, while $\omega_z^{(p)}/\omega_z$ and $\omega_y^{(p)}/\omega_y$ are the scaled frequencies for the corresponding p^{th} modes in the two directions. The scaled values for the axial modes are easily obtained numerically from the eigenvalue problem, and Ref. [35] includes tables of collective-mode eigenvectors and their scaled frequencies for $N \leq 10$. Since $\omega_z^{(p)} \geq \omega_z$, we can see from Eqn. (2.11) that the frequency ordering for the transverse modes is opposite to that for the axial modes. For example, the centre-of-mass (COM) mode ($p = 0$) is the lowest-frequency mode in the axial direction ($\omega_z^{(0)} = \omega_z$) but is the highest-frequency mode in the transverse direction ($\omega_y^{(0)} = \omega_y$). The zigzag mode ($p = N$), however, is the highest-frequency axial mode but is lowest in frequency (or the "softest") in the transverse direction.

Since the values of $\omega_z^{(p)}/\omega_z$ are independent of α for $\alpha \leq \alpha_{\text{crit}}$ [15], the values of $\omega_y^{(p)}$ decrease with increasing α (see Eqn. (2.11)). The frequency, $\omega_y^{(N)}$, of the transverse zigzag mode will decrease to zero first at a critical α, which marks where the linear crystal structure becomes unstable against the formation of the zigzag phase. Following the procedure of Ref. [35], it is straightforward to determine α_{crit} for crystals with 5, 6 and 7 ions to be 0.1604, 0.1158 and 0.0883 respectively, matching the values obtained from Fig. 2.4 of 0.1603, 0.1158, and 0.0883 pretty well. In terms of α_{crit}, the frequency for the transverse zigzag mode ($p = N$) can be expressed as,

$$\omega_y^{(N)} = \omega_y \sqrt{1 - \frac{\alpha}{\alpha_{\text{crit}}}}, \qquad \alpha_{\text{crit}} = \frac{2}{\left(\frac{\omega_z^{(N)}}{\omega_z}\right)^2 - 1} \tag{2.12}$$

where $\omega_y^{(N)}$ goes to zero as α approaches α_{crit}.

To illustrate the basic features of the collective vibrational modes near the zigzag transition, we have numerically calculated the mode frequencies as a function of α. We use Maple software, starting from Eqn. (2.10) and assuming small oscillations. The results for a crystal of seven identical ions are shown in Fig. 2.5 along with the equilibrium zigzag displacement at the centre of the crystal. In the linear region ($\alpha \leq \alpha_{crit}$), the seven up-going curves are the axial modes while the down-going ones are the transverse modes. The frequency of the transverse zigzag mode goes to zero at α_{crit}, which is where the zigzag displacement starts to grow at the centre of the crystal (Fig. 2.5(a)). The blue dash curve in Fig. 2.5(b) is the theoretical prediction for the zigzag mode from Eqn. (2.12) and Ref. [35], with the critical value chosen to be 0.0883 as determined above. As can be seen, the numerical simulation matches the theory quite nicely below α_{crit}, where the theory for 1-D crystals of Ref. [35] applies.

When an impurity ion is present in the crystal, one needs to consider the effect of the different mass on the collective modes. However, the impurity ion, $^{172}Yb^{+}$, that we actually use in experiment is very close in mass to the other $^{171}Yb^{+}$ ions in the crystal. The effect of the impurity is small, as we have already demonstrated above for α_{crit}.

2.2.3 Ion-crystal structure and hopping barrier

So far we have discussed the equilibrium crystal structure and the behaviour of the transverse zigzag mode as the zigzag structural phase transition is approached. Our initial motivation for studying hopping near the zigzag transition was the intuitive idea that the interior ions can more easily move transversely outward as the critical α is approached, and this should enable the hopping of the interior ions. We in fact will show in Chp. 4 that hopping happens most readily at the centre of the crystal. Here, we make some brief arguments in an attempt to quantify the effect of the trap anisotropy on the energy barrier to hopping.

At the centre of an equilibrium 1-D crystal, where the ions are already axially closest together, the barrier to hopping will be the lowest. To obtain an estimate of the barrier, the two interior ions in a six-ion crystal are placed at $z = 0$ and a simple numerical search for the lowest barrier is performed by minimizing the energy with respect to the pair's transverse separation and with respect to the positions of the remaining ions at zero kinetic energy. For α from 0.1 to 0.116, the barrier is found to range from $0.15E_0$ to $0.09E_0$. Thus, the barrier is

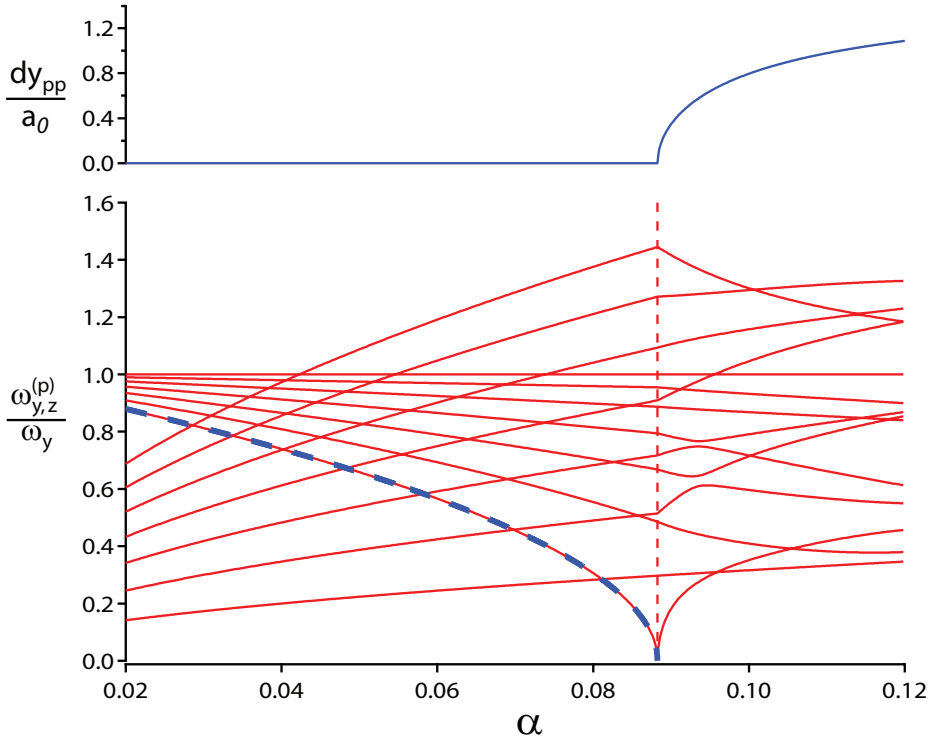

Figure 2.5: Numerical simulation of vibrational-mode frequencies for a seven-ion crystal near the onset of the zigzag transition. The upper panel shows the zigzag displacement as a function of α. The vertical dashed line separates the linear (left) and zigzag (right) regions. In the lower panel, solid (red) lines show the frequencies for different vibrational modes. The seven up-going curves are the axial modes; the down-going curves are the transverse modes. All frequencies are scaled to the transverse secular trap frequency ω_y. The blue dashed line shows the theoretical prediction of the transverse zigzag mode in the linear region (see text).

reduced (by about a factor two) as the zigzag transition is approached, but not dramatically in this model. One then expects the hopping rate to increase as the zigzag transition is approached, and one could perhaps estimate the rate according to an exponential thermal activation theory as was proposed in previous two-ion hopping experiments [21]. In our case, with many ions, it is not entirely clear if we can apply such a theory for a pair of ions undergoing a hopping event. For example, because of the strong, long range Coulomb coupling, it seems clear that all the ions need to be considered in a hopping event, but it is not clear if the net effect can be summed up in the size of an activation barrier for a given pair of ions. Furthermore, near the zigzag transition and at high kinetic energies, it seems that the dynamics at the centre of the crystal will be highly nonlinear and this may influence the hopping rate. Therefore, our approach will be to present the results for the hopping experiments first and then to consider molecular dynamics simulations to gain some understanding and, in the future, to guide us to some kind of analytical model.

2.3 Laser fluorescence and cooling

2.3.1 Review of basic theory

We conclude this chapter with a discussion of the effects of the 369.5-nm Doppler cooling laser, which allows us to control the kinetic energy of the ion-crystal and to image it through fluorescence. Recall that the ion crystals to be used for hopping studies are composed of $^{171}Yb^{+}$ ions with a single added $^{172}Yb^{+}$ impurity. The Doppler cooling laser is resonant with the $^{171}Yb^{+}$ ions, while the $^{172}Yb^{+}$ ion remains dark for distinguishability.

The energy levels of the $^{171}Yb^{+}$ ions relevant for laser cooling are shown in Fig. 2.6. The level structure and fluorescence behaviour is more complicated than for the $^{172}Yb^{+}$ isotope, which has no hyperfine structure; however, we have chosen to use the $^{171}Yb^{+}$ ions as the primary component of the ion crystals in our experiment since our group has recently made a careful study and calibration of the fluorescence response of $^{171}Yb^{+}$ for quantum computing applications [31].

It is the main $^{2}S_{1/2}(F=1) \rightarrow {}^{2}P_{1/2}(F=0)$ transition in $^{171}Yb^{+}$ at 369.5261 nm that is used for fluorescence imaging and Doppler-cooling. (The $^{2}S_{1/2} \rightarrow {}^{2}P_{1/2}$ transition for $^{172}Yb^{+}$ at 369.5244 nm is separated by 3.5 GHz due to the isotope shift.) A $^{171}Yb^{+}$

ion initially in $^2S_{1/2}(F=1)$ can absorb a photon from a 369.5-nm laser beam and go to the $^2P_{1/2}(F=0)$ state. From there, the ion has a very high probability to return to the $^2S_{1/2}$ ground state by spontaneous emission and, in doing so, must return to the $F=1$ hyperfine level by angular momentum selection rules. As long as a trapped ion is kept in this transition cycle, it will continuously scatter photons, and its fluorescence can be imaged by a camera. Also, each time the ion absorbs or emits a photon, its momentum is changed, which for appropriate laser parameters leads to Doppler-cooling. An ion in the cycle of the $^2S_{1/2}(F=1) \rightarrow {}^2P_{1/2}(F=0)$ transition is also continuously cooled.

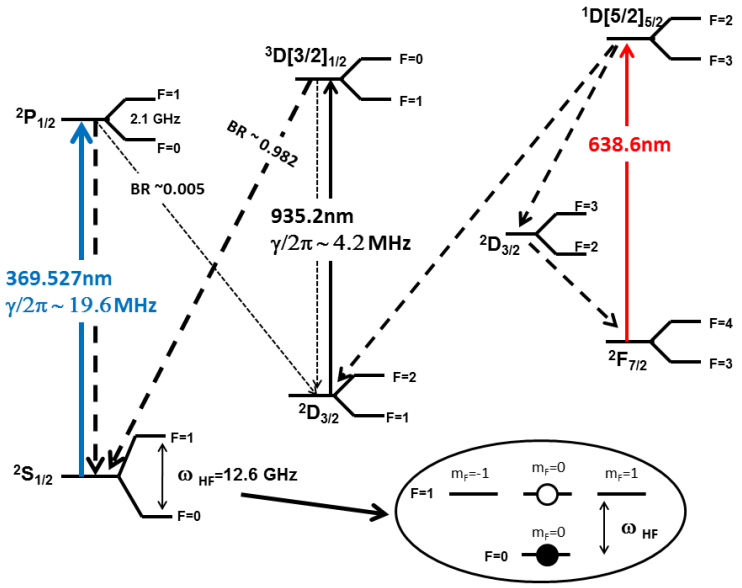

Figure 2.6: Energy levels of $^{171}\mathrm{Yb}^+$

The cooling and fluorescence transition is not perfectly closed but has several leaks, which, if not plugged, cause the ion fluorescence and cooling to cease. First, the cooling laser can off-resonantly excite the ion to the $^2P_{1/2}(F=1)$ state from which it can decay to the $^2S_{1/2}(F=0)$ state and out of the cooling transition. To repump the ion back into the cooling cycle, an additional laser frequency is needed on the $^2S_{1/2}(F=0) \rightarrow {}^2P_{1/2}(F=1)$ transition. As long as the repump laser intensity is high enough the leakage has a negligible effect on the fluorescence and Doppler-cooling rate. An additional leak out of the cooling cycle can occur via spontaneous decay from the $^2P_{1/2}$ excited state to the low-lying $^2D_{3/2}$

state (see Fig. 2.6) with a small branching ratio of 0.005. The natural decay rate of the $^2D_{3/2}$ state back to the ground state is far too slow to provide repumping. In order to return the ion to the main $S-P$ transition, repump laser frequencies with wavelength near 935.2 nm are required to clear out the hyperfine states of the $^2D_{3/2}$ state (see Fig. 2.6). Finally, a collision of an ion in one of the excited states with a background gas atom can also transfer the ion into the low-lying $^2F_{7/2}$ state, and thereby remove it from the fluorescence and cooling cycle [37, 38, 39]. A 638-nm laser is required to repump the ion back to $^2D_{3/2}$ state, from where it is further pumped back to the $S-P$ cycle.

With the 935-nm and 638-nm lasers continuously on during the experiment, we are able to keep the ion in the $^2S_{1/2}(F=1) \rightarrow {}^2P_{1/2}(F=0)$ cycle. However, the fluorescence of the $^{171}\mathrm{Yb}^+$ ion can still be suppressed due to the mechanism of coherent population trapping (CPT) [32]. In CPT, the ion is optically pumped into a coherent superposition of Zeeman levels in the ground-state that is decoupled from the laser field. For $^{171}\mathrm{Yb}^+$, the $^2D_{3/2} - {}^3D[3/2]_{1/2}$ repump transition is also susceptible to CPT.

Coherent population trapping can be counteracted by introducing a magnetic field of sufficient strength [32] or by modulation of the laser polarization [34]. The magnetic-field approach is adopted in our experiment due to its simplicity, and the field also serves to define a quantization axis. Previous experiments have been performed in our group to study the resonance fluorescence of a single trapped $^{171}\mathrm{Yb}^+$ ion [31] and to verify its predicted behaviour as a function of laser parameters and magnetic field [32], including the effect of the magnetic field at counteracting the coherent population trapping. Further details can be found in Refs. [32] and [31]. We simply quote here the result for the steady-state spontaneous scattering rate $\gamma_{sc} = \gamma \mathcal{P}_e$, which is determined by the natural linewidth, $\gamma = 2\pi \cdot 19.6$ MHz, of the $^2S_{1/2} \rightarrow {}^2P_{1/2}$ transition and the steady-state population $\mathcal{P}_e$ of the excited $^2P_{1/2}(F=0)$ state. With slight modification from Refs. [31] and [32], the expression for $\mathcal{P}_e$ as a function of magnetic field and as a function of laser power, detuning and polarization is as follows:

$$\mathcal{P}_e = \frac{3}{4}\frac{\cos^2\theta_{BE}\sin^2\theta_{BE}}{1+3\cos^2\theta_{BE}}\frac{\frac{\Omega^2}{3}}{\Delta^2+\left(\frac{\Gamma_{171}}{2}\right)^2} = F(\theta_{BE})\frac{\Omega^2}{\Delta^2+\left(\frac{\Gamma_{171}}{2}\right)^2}, \tag{2.13}$$

where the effective linewidth Γ_{171} is given by

$$\left(\frac{\Gamma_{171}}{2}\right)^2 = \left(\frac{\gamma}{2}\right)^2 + \frac{\Omega^2}{3}\cos^2\theta_{BE}\frac{1-3\cos^2\theta_{BE}}{1+3\cos^2\theta_{BE}} + \frac{\cos^2\theta_{BE}}{1+3\cos^2\theta_{BE}}\left(\frac{\Omega^4}{36\delta_B^2}+4\delta_B^2\right). \quad (2.14)$$

In the equations above, θ_{BE} denotes the angle between the magnetic field and the polarization direction of the 369.5-nm laser, and the definition of $F(\theta_{BE})$ is purely for notational simplicity in subsequent expressions. Further, $\delta_B = \mu_B B/\hbar$ is the frequency splitting between adjacent Zeeman sublevels of the $F = 1$ ground state under magnetic field B, and $\Delta = \omega - \omega_0$ gives the detuning of the laser from the resonance when $B = 0$. The laser Rabi frequency, Ω, is defined in terms of the laser intensity, I, and the saturation intensity, I_0, or equivalently the on-resonant saturation parameter, $s_0 = I/I_0$, as follows:

$$\Omega = \sqrt{\frac{s_0}{2}}\gamma, \qquad s_0 = \frac{I}{I_0}, \qquad I_0 = \frac{\pi hc}{3\lambda^3}\gamma, \quad (2.15)$$

where $\lambda = 369.5$ nm is the wavelength of the ${}^2S_{1/2} \rightarrow {}^2P_{1/2}$ transition.

The effective linewidth Γ_{171} includes polarization effects, and Zeeman and power broadening. At low laser powers, the linewidth is roughly constant and the excited-state population grows as $\mathcal{P}_e \sim \Omega^2$ while, at high powers, the effective linewidth broadens as Ω^2 due to coherent population trapping and the population drops off as $\mathcal{P}_e \sim 1/\Omega^2$.

At any fixed δ_B, the excited state's population has a maximum value when $\theta_{BE} \approx \theta_o \equiv \arccos\left(\frac{1}{\sqrt{3}}\right) = 54.7^\circ$. At this value, one finds that $F(\theta_{BE}) = 1/36$ and, on resonance, the excited population reduces to $\Omega^2/9\Gamma_{171}^2$. In our experiment, we use a 5.9-G magnetic field transverse to the laser wavevector, and the polarization direction of the laser is set to an angle $\theta_{BE} = 57.5^\circ$ with respect to the direction of the magnetic field to ensure near-optimal ion fluorescence. At this field and polarization angle, the fluorescence on resonance is expected to peak at $s_0 = 7.6$ with an excited-state fraction of 0.14 in steady state.

In the above discussion of resonant fluorescence, the ion has been assumed to be stationary. We now consider the mechanical effects on the ion due to an incident laser at 369.5 nm. During fluorescence, the momentum and energy of the ion are affected by the recoils acquired during absorption and emission of photons. Since the absorbed photons are from a certain direction – the laser wavevector $\vec{k}$ – and the spontaneous emission is symmetric, if not isotropic, in space, the ion will experience on average a force called the radiation pressure of $\vec{F} = \hbar\vec{k}\gamma_{sc}$, where $\gamma_{sc} = \gamma\mathcal{P}_e$ is the photon scattering rate as before. This average radiation pressure pushes the fluorescing ion downstream of the laser direction.

Besides the radiation pressure, photon-scattering also leads to cooling and heating effects, in particular Doppler cooling [40, 20]. First observed in the 1970s with trapped ions [41, 42], Doppler laser cooling is now widely used in atomic physics experiments as a main source of cooling or as a preliminary step before deeper cooling methods such as the Raman sideband technique [43]. In our experiment, Doppler cooling is used to control the "temperature" of the ions, which not surprisingly is an important parameter affecting the hopping behaviour within the ion crystal. The theory of Doppler cooling was developed in the 70's and 80's [41, 44, 45] and a review may be found in Refs. [40] and [20]. Following the semi-classical discussion in Ref. [45], we provide a summary below of the basic theory. It is noted here in advance that the results presented are the standard ones that are useful near the Doppler-cooling limit, while the hopping experiments are in a regime of high temperature well above the Doppler limit. Nevertheless, the derivation helps in understanding how Doppler-cooling of trapped ions works, and a discussion of the limitations to the theory is provided afterwards.

Consider the following scattering event in the laboratory frame, where an ion with mass M has its velocity changed from $\vec{v}$ to $\vec{v}\,'$ by first absorbing a photon with wave vector $\vec{k}$ and then emitting a second photon with wave vector $\vec{k}_s$. In the non-relativistic limit, conservation of momentum and energy leads to

$$\Delta v_i = v_i' - v_i = \frac{\hbar}{M}(k_i - k_{si}), \tag{2.16}$$

$$\Delta E_i = \frac{1}{2}M(v_i')^2 - \frac{1}{2}M(v_i)^2 = \frac{\hbar^2}{2M}(k_i - k_{si})^2 + \hbar(k_i - k_{si})v_i, \quad (i = x,y,z), \tag{2.17}$$

where the subscript i for the vectors denotes different components and ΔE_i is the kinetic energy of the motion in the i^{th} direction.

The equations above describe the motion of a free ion; however, they are also applicable to the case of a "weak" trap where the secular trap frequency ω_i is much smaller than the natural linewidth γ of the transition. For example, this applies to our experiment with trap frequencies $\omega_y/2\pi = 0.4$ MHz and $\omega_z/2\pi = 0.1$ MHz, and $\gamma/2\pi = 19.6$ MHz. In this case, the scattering process happens much faster than the secular motion and the ion can be viewed as a free particle during the scattering [44]. Javanainen and Stenholm describe a similar "heavy particle limit" for which the rate of change of the position and velocity of the oscillating ion are slow compared to the scattering process [46, 47]. Also, note here we

ignore micro-motion, which we assume is already properly minimized [20, 48]. In near-resonance scattering, which we consider here, the absorption frequency ω and emission frequency ω' both fall close to the resonance frequency ω_0, within a combined linewidth from Doppler and natural broadening. Since $v \ll c$ and $\gamma \ll \omega_0$, one has $\omega \approx \omega'$ and thus $k \approx k'$. Introducing unit vector $\hat{k} = \vec{k}/k$ and $\hat{k_s} = \vec{k_s}/k_s$, Eqn. (2.17) can be rewritten as

$$\Delta E_i = R(\hat{k_i}^2 - 2\hat{k_i}\hat{k}_{si} + \hat{k}_{si}^2) + \hbar(k_i - k_{si})v_i, \tag{2.18}$$

where $R = (\hbar k)^2/2M$ is the recoil kinetic energy due to an absorption or emission.

The probability per unit solid angle, $P_s(\hat{k_s})$, to emit a photon in the direction of $\hat{k_s}$ depends on the ΔM_F value of the transition. However, for spontaneous emission from ${}^2P_{1/2}(F=0)$ to ${}^2S_{1/2}(F=1)$, all of the polarization transitions, $\Delta M_F = 0, \pm 1$, are equally probable, which implies that $P_s(\hat{k_s}) = 1/4\pi$ for any $\hat{k_s}$. Averaging Eqn. (2.18) over all $\hat{k_s}$ gives the expectation for the energy change in one scattering event as follows:

$$\langle \Delta E_i \rangle_s = \int P_s(\hat{k_{si}}) \Delta E_i d\Omega = R(f_i + f_{si}) + \hbar k_i v_i \tag{2.19}$$

$$f_i = \hat{k_i}^2, \qquad f_{si} = \int P_s(\hat{k_s}) \hat{k_{si}}^2 d\Omega. \tag{2.20}$$

As $P_s(\hat{k}_{si}) = P_s(-\hat{k}_{si})$, we have dropped the linear terms in $\hat{k}_{si}$ from Eqn. (2.18). For our specific case of ${}^{171}\mathrm{Yb}^+$, the values of f_{si} are all $1/3$ while the values of f_i depend on the orientation of the laser wavevector with respect to the principal axes of the trap. Summed over all directions i, the expected total energy change in one scattering is

$$\langle \Delta E \rangle_s = 2R + \hbar\vec{k} \cdot \vec{v}. \tag{2.21}$$

The *rate* of energy change is given by the steady-state spontaneous scattering rate γ_{sc} multiplied by the energy change per scattering event. The scattering rate depends on the population of the $P_{1/2}$ excited state, which is given in Eqn. (2.13). Considering the ion motion, we should replace Δ in Eqn. (2.13) with $\Delta - \vec{k} \cdot \vec{v} - R/\hbar$ in the non-relativistic limit due to conservation of energy and momentum. The second term is the usual first order Doppler shift that accounts for the ion's velocity and the third term accounts for the recoil energy. Further averaging over the velocity probability distribution for the trapped ion, and with $F(\theta_{BE})$ as defined in Eqn. (2.13), one gets the following equation for the time rate of

change of the average kinetic energy of the ion:

$$\frac{dE_i}{dt} = \langle \gamma \mathcal{P}_e \langle \Delta E_i \rangle_s \rangle_v = \gamma \Omega^2 F(\theta_{BE}) \left\langle \frac{R(f_i + f_{si}) + \hbar k_i v_i}{(\Delta - \vec{k}\cdot\vec{v} - R/\hbar)^2 + (\frac{\Gamma_{171}}{2})^2} \right\rangle_v . \tag{2.22}$$

One can derive the steady-state Doppler temperature as a function of laser parameters by the reasoning below. When the ion is already substantially cooled, one can assume the root-mean-squared velocity to satisfy $k(v)_{rms} \ll \Gamma_{171}/2$ and $k(v)_{rms} \ll \omega_0 - \omega + R/\hbar \approx \omega_0 - \omega$. Thus,

$$\frac{dE_i}{dt} = \gamma_{sc0} \left\{ R(f_i + f_{si}) + \frac{2\Delta\hbar k^2 f_i \langle v_i^2 \rangle_v}{\Delta^2 + \left(\frac{\Gamma_{171}}{2}\right)^2} \right\}, \tag{2.23}$$

where

$$\gamma_{sc0} = \frac{\gamma \Omega^2 F(\theta_{BE})}{\Delta^2 + \left(\frac{\Gamma_{171}}{2}\right)^2} \tag{2.24}$$

is the scattering rate at zero velocity. In obtaining Eqn. (2.23), two more assumptions are made. First, the velocity distribution is unchanged with reflection of $\vec{v}$, which is reasonable in a harmonic trap. Second, $\langle v_i v_j \rangle_v = 0$ for $i \neq j$, which should be valid when the three secular frequencies are sufficiently different [46]. In the steady state ($dE_i/dt = 0$), we have

$$E_{Ki} = \frac{1}{2} M \langle v_i^2 \rangle_v = -\hbar \left(1 + \frac{f_{si}}{f_i}\right) \frac{\Delta^2 + \left(\frac{\Gamma_{171}}{2}\right)^2}{8\Delta}, \tag{2.25}$$

which is the result Eqn. (28) in Ref. [45]. Note that the solution is sensible only for $\Delta < 0$, that is, when the laser is red-detuned from resonance. Furthermore, we can see that if the laser wave-vector is perpendicular to the i^{th} principal axis of the trap ($f_i = 0$), the energy along that direction diverges ($E_{Ki} \to \infty$). In this case, no cooling is present in that direction to counterbalance the recoil heating from spontaneous emission. In order to have all three directions efficiently cooled, the laser's wave-vector should be set in such a direction that it has components along all the trap axes. In our experiment, the cooling laser's direction is chosen with this in mind (see below).

The steady-state kinetic energy depends on detuning Δ and the effective linewidth Γ_{171}, which is itself a function of power saturation parameter s_0, magnetic field B and polarization angle θ_{BE}. The achievable minimum is $(1 + f_{si}/f_i)\hbar\Gamma_{171}$ when we set $\Delta = -\frac{\Gamma_{171}}{2}$.

Further, in the case of isotropic scattering, we have $f_{si} = 1/3$ for $i = x, y, z$. The total energy is minimized if one sets $f_x = f_y = f_z = 1/3$. Equation (2.25) then gives $E_{Ki} = \Gamma_{171}/4$. At low power ($s_0 \ll 1$) and small magnetic field ($\delta_B \ll \gamma$), we have $\Gamma_{171} \to \gamma$. Thus, the steady-state kinetic energy along each direction reduces to $E_{Ki} = \hbar\gamma/4$ and the total energy is $E_i = \hbar\gamma/2$, which is often referred to as the Doppler-cooling-limit. In our experiment, the incident laser lies in the horizontal plane and makes an angle of 45° with the z axis so that $\vec{k} = k(\frac{1}{2}\hat{x} + \frac{1}{2}\hat{y} + \frac{1}{\sqrt{2}}\hat{z})$. Thus we have $f_x = f_y = 1/4$ and $f_z = 1/2$, leading to different kinetic energies along axial and transverse directions.

In Fig. 2.7, we plot the average energy, $\langle E_i \rangle = 2E_{Ki} = k_B T_i$, of a $^{171}Yb^+$ ion in the axial and transverse directions as a function of laser detuning and intensity, which we use as control parameters during the hopping experiment. The energy is scaled to $\hbar\omega_y$ and the laser intensity is expressed in terms of the on-resonant saturation parameter s_0, defined in Eqn. (2.15). Parameters are chosen to match typical experimental values used during hopping experiments. For reference, the fluorescence rate based on Eqn. (2.13) is also shown as a function of s_0. Where the power is sufficiently high that the fluorescence begins to fall due to CPT, the effective linewidth begins to broaden quickly and the average energy grows quickly. Also, it can be seen that the energy monotonically increases as the power is increased or as detuning approaches zero from below. Although the range of experimental parameters far exceeds the validity of the simple result of Eqn. (2.25) – see discussion below – we expect the general trends to hold.

2.3.2 Deviations from the basic theory

In the above discussion, we have presented the basics of Doppler-cooling theory; however, the mathematical form of the steady-state energy (Eqn. (2.25)) is not expected to be an accurate description for the ion crystals in our experiment. First, in deriving Eqn. (2.23), one assumes $k(v)_{rms} \ll \Gamma_{171}/2$ and $k(v)_{rms} \ll |\Delta|$. Although the first assumption is in fact not necessarily violated at the higher energies that we consider in the experiment, the second assumption is clearly problematic when one deliberately drives the ions hot at high power and close detuning ($\Delta \to 0$). In these circumstances, one presumably should resort to solving numerically for the steady-state distribution with, for example, the theory of Ref. [49].

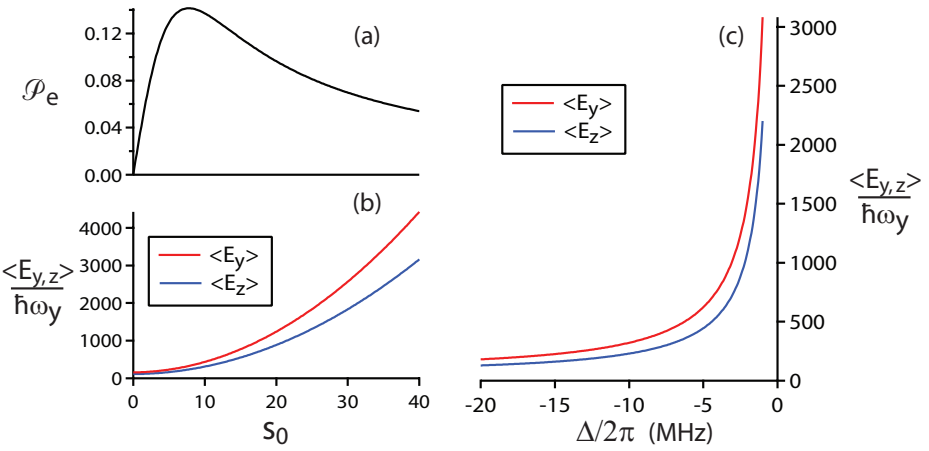

Figure 2.7: Average energy of a single trapped $^{171}Yb^{+}$ ion as a function of laser detuning and laser power. Left panels show the the effect of cooling laser power on (a) the excited state's population $\mathcal{P}_e$ and on (b) the average energy of the trapped ion in the axial (blue) and transverse (red) directions. For both (a) and (b), the laser detuning is fixed at $\Delta/2\pi = -1.2$ MHz. Right panel (c) shows the dependence of the average energy on detuning of the laser in the axial (blue) and transverse (red) directions, where laser power is fixed at $s_0 = 30$. For all plots, the magnetic field is 5.9 G; the polarization angle is $\theta_{BE} = 57.5^{\circ}$; and a typical transverse secular trap frequency of $\omega_y/2\pi = 430.0$ kHz is assumed.

Second, care should be taken in the assumption $\langle v_i v_j \rangle_v = 0$. Correlations in the velocity distribution are only negligible if the difference in the trap frequencies are sufficiently large compared to the recoil frequency $\omega_r/2\pi = 8.5$ kHz [46]. In the typical trap that we have used for data collection with $\{\omega_x, \omega_y, \omega_z\}/2\pi = \{447, 431, 114\}$ kHz, the two transverse frequencies are actually quite close, being separated by about twice the recoil frequency. The net effect is expected to be an increase in the average energy along the transverse directions and a change in the average-energy dependence on the laser detuning [46].

A further issue with the above Doppler theory is that it is derived for a single ion or a collection of non-interacting particles, while we are considering crystallized arrays of 6 or 7 ions with strong Coulomb interactions. In fact, it turns out that Doppler cooling of an ion crystal is more or less the same as for a single ion, at least near the Doppler limit [50]. In the small oscillation regime, the motion of the ions is described by their collective vibrational modes (Sec. 2.2), and Doppler cooling can then be viewed in terms of the cooling of the various independent modes. When the laser is at high power or is closely detuned, the energy of the ions will lead to large amplitudes for the collective modes. The resulting coupling between the modes, if nothing else, moves the situation away from the simple one considered in Ref. [50]. Another complication of laser cooling of an ion crystal is the need to account for differences between the ions. The most obvious example is a non-uniform illumination due to the laser beam profile across the ion crystal. The cooling process needs to account for the laser cooling effect of each ion as well as the energy transfer between them due to interactions. It would not be surprising in such a situation for there to exist a non-uniform temperature profile across the ion crystal. The complication of laser beam profile turned out to be one of the technical limitations to the interpretation of the experiment and is discussed in detail in the context of results in Chp. 4.

A more extreme example of an inhomogeneous cooling effect in our experiments is due to the isotopic impurity that we introduce to the crystals to observe hopping. With the Doppler laser beam tuned close to the resonance of the $^{171}Yb^+$ ions in the crystal, the $^{172}Yb^+$ impurity does not fluoresce due to the isotope shift. The lack of fluorescence is, of course, what allows us to distinguish the isotope, but, at the same time, this means that the impurity is not directly laser-cooled. Indirectly, however, the Coulomb interactions with the surrounding $^{171}Yb^+$ ions enables sympathetic cooling of the impurity [51, 52]. The sympathetic cooling rate almost certainly depends on the position of the dark impurity

within the crystal. There is also the possibility that the overall mechanical response of the crystal to the cooling laser may depend on the position of the non-fluorescing impurity, but one might expect the effect to be less important in larger crystals.

The ultimate goal of modeling the laser cooling for the hopping experiment is to associate a given hopping rate with an average energy of the ions. Given the various complications discussed above, it does not seem sensible to attempt an analytical model of the average energy. In the end, it seems better to use numerical simulations to compare to experiments, and we lay the ground work for that in Chp. 5. In closing, we note in advance that to obtain a qualitative idea of the average energy imparted to the ions, we have studied the energy of a single $^{171}Yb^{+}$ ion as a function of laser power and detuning. From the Gaussian profile of the ion's time-integrated position in the harmonic trap, we can estimate its average energy. To within the limits of the technique, we find that the average axial and transverse energies match remarkably well (within a factor of $2-4$) to the simple theory of Eqn. (2.25) and the transverse energy is found to be higher than the axial one.

2.4 Summary

We have presented an overview of the structure of ion crystals in a linear rf Paul trap and the basic dynamics of the crystals. In particular, we have focused on the crystal behaviour near the structural zigzag transition. We have argued that the structure and mechanical behaviour of the crystal is likely to lead to easier hopping at the centre of the crystal and that the trap anisotropy is expected to affect the hopping. We have also reviewed the simple theory of laser cooling and have shown that it is not trivial to model the average energy of the crystal for the laser parameters used during the hopping experiments. Notwithstanding all the complications mentioned, the basic trend of higher energy at higher laser power and closer detuning is expected. Observations in the experiment should, therefore, show that the hopping rate increases at higher laser power or/and closer detuning. In the experiment, our initial aim is to demonstrate that it is in fact possible to tune the energy and hopping rate in a controlled manner.

Chapter 3

Experiment Setup and Procedure

In this chapter, we look at the experimental setup used to study the hopping dynamics of a $^{172}Yb^{+}$ impurity in a crystal of trapped $^{171}Yb^{+}$ ions. We first describe the ion trap and how we calibrate its secular trap frequencies as a function of the end-cap voltages. We also make a comparison of the frequencies to the ion-trap theory introduced in Chp. 2. Following that is a discussion of the various lasers and their sidebands used in the experiment, with the main focus on the 369.5-nm cooling and detection laser since it is used to control the hopping rate. In Sec. 3.3, the imaging system that is used to monitor the dynamics of the crystal is summarized. Finally, the chapter concludes with a description of the basic experimental procedure used to obtain the results presented in Chp. 4.

3.1 Ion trap setup

As mentioned in the previous chapter, the millimeter-scale linear rf Paul trap used in the experiment is composed of four rods in a square configuration and two end-cap electrodes. A photograph of the trap installed inside the vacuum chamber is shown in Fig. 3.1(a) and a sketch with dimensions is shown in Fig. 3.1(b). The nearest distance from the ion to the rods is about 0.7 mm and the tip-to-tip spacing of the end-cap needles is 2.5 mm. A $\sim$ 30-MHz oscillation voltage is applied to a pair of opposing rods indicated in yellow in Fig. 3.1(b) and the other pair indicated in green in Fig. 3.1(b) is rf-grounded. The resulting pseudo-potential provides time-averaged confinement in the transverse direction (see Chp. 2). The end-caps are biased with a dc voltage in the range of 10-30 V to provide confinement in the

axial direction. Each rod or end-cap can be independently dc-biased, allowing the position of a linear ion crystal to be finely adjusted to place it along the minimum of the rf potential where the effect of micro-motion is minimized. Typical bias voltages are in the range of 0-200 mV.

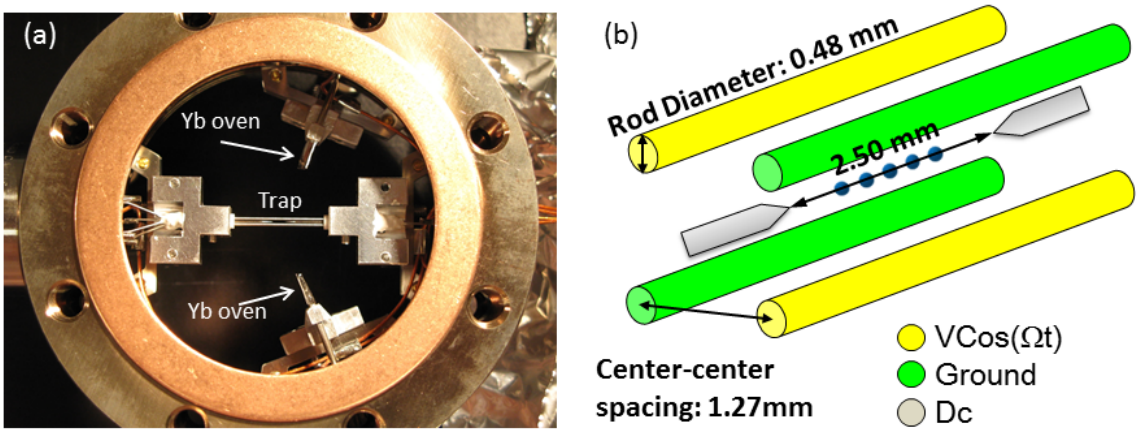

Figure 3.1: Setup of linear Paul trap. Part (a) is a top view of the trap along the imaging axis, showing the relative position of the trap and the Yb oven. Part (b) gives the dimensions of the linear rf Paul trap including four rods and two end-cap needles. The voltage on a pair of opposing rods (yellow) is oscillating at $\Omega/2\pi \sim$30 MHz.

The time-averaged confining potential is nominally harmonic, characterized by three secular trap frequencies. In our experiment, the end-cap voltages, rather than the rf voltage, are used to vary the trap asymmetry as part of the studies of hopping dynamics. The axial ion-spacing and the Coulomb interaction energy also vary at the same time, which introduces another variable to the dynamics; however, changing the dc voltage on the end-caps avoids rf-power dependent trap distortions due to thermalization effects of the trap electrodes. For each set of end-cap voltages used during the hopping experiment, we measure the secular trap frequencies by direct excitation in order to calibrate the trap asymmetry. In the calibration procedure, we first change the voltages on the end-caps while making sure the single trapped ion (or the centre of an ion crystal) remains located at the same axial position on the imaging camera. Voltages on the four rods are then fine tuned by a few mill-volts to minimize micro-motion along the direction of the cooling laser. An rf synthe-

sizer is ac-coupled to one of the end-caps or rods, depending on which trap frequency we wish to measure, and a manual or automatic scan of the synthesizer frequency is performed. When the output frequency is resonant with the secular trap frequency (or centre-of-mass frequency of the crystal) along the direction of interest, we observe a delocalized ion (or ion crystal) and the fluorescence level drops. We identify such a resonant frequency as the trap frequency in the corresponding direction.

Figure 3.2 shows the secular trap frequency data from several days of acquisition, measured by direct excitation. The values vary from $\{\omega_x, \omega_y, \omega_z\}/2\pi = \{447, 431, 114\}$ kHz to $\{433, 416, 197\}$ kHz over an end-cap U_0 range of 10–28 V and clearly show the basic features of axial tightening and transverse defocusing of the confinement with increasing end-cap voltage. From Sec. 2.1 in Chp. 2, we expect the secular frequency along the i^{th} direction to obey the following functional from:

$$\omega_i = \frac{1}{2}\Omega\sqrt{a_i + \frac{1}{2}q_i^2}, \tag{3.1}$$

where Ω is the rf trap frequency, q_i in Eqn. (2.4) characterizes the strength of the rf voltage V_0, and a_i as in Eqn. (2.3) is associated with the dc voltages applied to the rods and end-caps.

Since the rf voltage is kept constant during the experiments, we fit the secular frequencies in Fig. 3.2 to the following functions:

$$f_i = \sqrt{A_i U_0 + B_i}, \quad i = x, y, z. \tag{3.2}$$

Here $f_i = \omega_i/2\pi$ is the secular frequency in the i^{th} direction, $A_i U_0$ is proportional to a_i in Eqn. (2.3), while B_i is proportional to q_i^2 in Eqn. (2.4). The fitting procedure gives $\{-6.22(9)\times 10^2, -6.54(9)\times 10^2, 1.374(4)\times 10^3\}$ kHz^2/V for the A coefficients in the three directions, and the B coefficients are $\{2.049(2)\times 10^5, 1.914(2)\times 10^5, -3.7(5)\times 10^2\}$ kHz^2. Here we see that $\sum A_i \approx 0$, $A_x \approx A_y$, consistent with the expectation from Eqn. (2.3) for an ideal linear rf Paul trap. The theory for the ideal linear trap also predicts $q_x = -q_y$ and $q_z = 0$, matching, in part, the results from the fit where $B_x \approx B_y$ and $B_z \ll B_x$. We would normally expect the B_z value to be a small and positive value due to rf fringing fields "leaking" into the axial direction. The negative value of B_z is inconsistent with a simple physical model of the trap and may be due to the use of the average value of the end-cap voltages for the plot or another technical effect. If the value of B_z is fixed to zero, the fit

systematic is at most 1 kHz across the range ($\leq 1\%$ effect). The fit also shows that the symmetry between the x and y directions is broken, leading to weaker confinement in the y direction. This is partly due to the asymmetry in static potentials that dc-bias the rods, but the deviation from the square trap configuration is also an important factor to be considered.

For the purposes of the hopping experiments, we are only concerned with the axial frequency ω_z and the frequency ω_y for the weakest transverse direction. From these, we calculate the trap anisotropy, which is characterized by the parameter $\alpha = (\omega_z/\omega_y)^2$, as historically defined [13]. As already noted in Chp. 2, the anisotropy decreases with increasing α.

3.2 Laser setup

Figure 3.3 (reproduced from Chp. 2) shows the energy levels and laser transitions for the $^{171}Yb^+$ isotope, which forms the main component of the ion crystals used in our hopping studies. A brief summary is provided below to illustrate the setup and usage of the various lasers in our experiment including the 399-nm laser for photo-ionization loading of ions into the trap; the 369.5-nm $^{171}Yb^+$ "cooling and detection" laser that, in fact, serves multiple purposes of photo-ionization, cooling, optical pumping and detection; and the lasers at 935 nm and 638 nm for repumping. A frequency-doubled Ti:Sa laser is also used for facilitating the loading process, for identification of the $^{172}Yb^+$ isotopic impurity in ion crystals and, finally, for photo-dissociation to recover trapped Yb^+ ions which have formed molecules via background gas collisions. The main focus is on the $^{171}Yb^+$ cooling and detection laser for its crucial role in our experiment. Additional details on the setup can be found in a previous thesis [53] and in Ref. [31].

3.2.1 Photo-ionization laser

A 399-nm laser (see Fig. 3.4) is used for an efficient and isotopically selective ion-loading technique based on photo-ionization [54]. In the loading process, neutral Yb atoms are emitted from an oven and travel in a roughly collimated beam through the centre of the trap, where the 399-nm laser with a waist diameter of 60-100 μm is focused. The laser beam is arranged to propagate perpendicular to the atomic beam to limit effects of Doppler

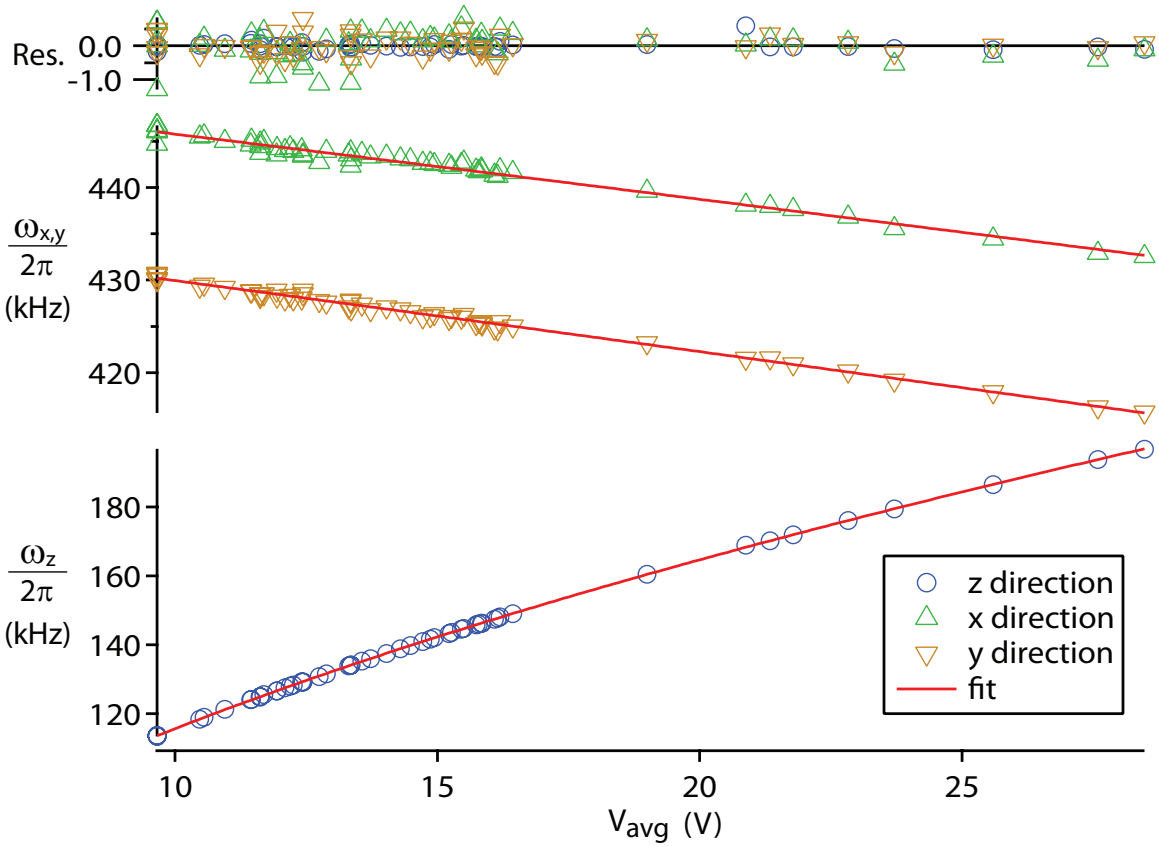

Figure 3.2: Calibration of secular trap frequencies. Measured secular frequencies in the three directions are plotted as a function of the average of the end-cap voltages. Solid curves are fits to the function in Eqn. (3.2). The coefficients A_i are $\{-6.22(9)\times10^2, -6.54(9)\times10^2, 1.374(4)\times10^3\}$ kHz^2/V while B_i are $\{2.049(2)\times10^5, 1.914(2)\times10^5, -3.7(5)\times10^2\}$ kHz^2.

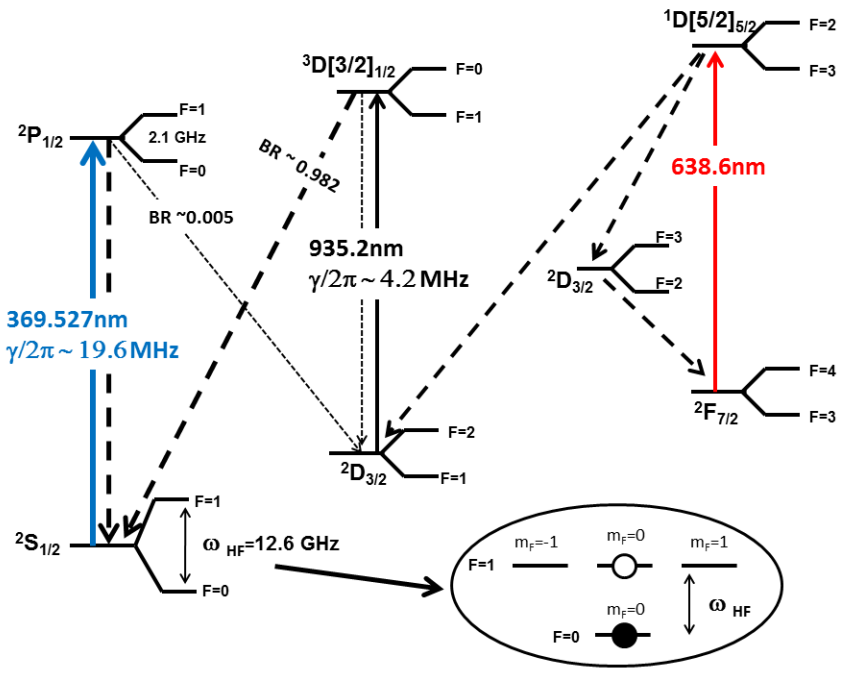

Figure 3.3: Energy levels of $^{171}Yb^+$ (reproduced from Chapter 2). The levels for $^{172}Yb^+$ are similar but without hyperfine structure.

broadening. The 399-nm laser from TOPTICA (model DL100), is a grating-stabilized external-cavity diode laser system and has a line-width of a few MHz. With its frequency properly tuned and its power set sufficiently low, the laser can excite one of the neutral Yb isotopes from the $^1S_0$ to $^1P_0$ state with reasonable selectivity. (The isotope shifts are around hundreds of MHz). Following the excitation, the atom can further absorb a second 399-nm photon and go to a high-lying Rydberg level, from which the atom can be ionized by the electric field of the trap. Alternatively, an outer electron in the atom in the $^1P_0$ state can be directly excited to the continuum by absorbing a 369.5-nm photon from the $^{171}Yb^+$ cooling and detection laser or from the frequency-doubled Ti:Sa laser, both of which are present during loading (see below). For the sake of isotopic selectivity, the power of the 399-nm laser is reduced to have about 100 μW in the trap to suppress saturation broadening on the $^1S_0 - ^1P_0$ transition. The higher 369.5-nm power of 2 mW from the cooling laser, and the $\sim$ 10 mW from the doubled Ti:Sa laser laser are assumed to contribute most in the second step of ionization [54].

3.2.2 Cooling and detection laser

After photo-ionization and capture into the trap, the ions may be still in a large orbit and need to be cooled down to the trap centre. For cooling, we use a 369.5-nm laser, red-detuned to the $^2S_{1/2} \rightarrow {}^2P_{1/2}$ transition of $^{171}Yb^+$.

This multi-purpose 369.5-nm laser, used in loading, cooling, optical pumping and detection, is generated by a commercial TA-SHG laser system from TOPTICA and consists of an amplified 739-nm diode laser feeding a frequency-doubling ring cavity in a bow-tie configuration. The 5-mW, 369.5-nm laser output from this system is transferred to the experiment through a single-mode, polarization-maintaining optical fiber with 40% coupling efficiency. The 2-mW beam from the fiber output is then split into two paths (see Fig. 3.4): The higher-power "loading" path is only used in the loading process, where it helps to photo-ionize Yb atoms and Doppler-cool the ions to the trap centre. This beam path is blocked when loading is finished. The lower power "cooling and detection" path is the primary one that provides Doppler-cooling and fluorescence imaging of the $^{171}Yb^+$ ions during hopping experiments. Most of the power is delivered to the loading path while about 10%, or 200 μW, is used for cooling and detection.

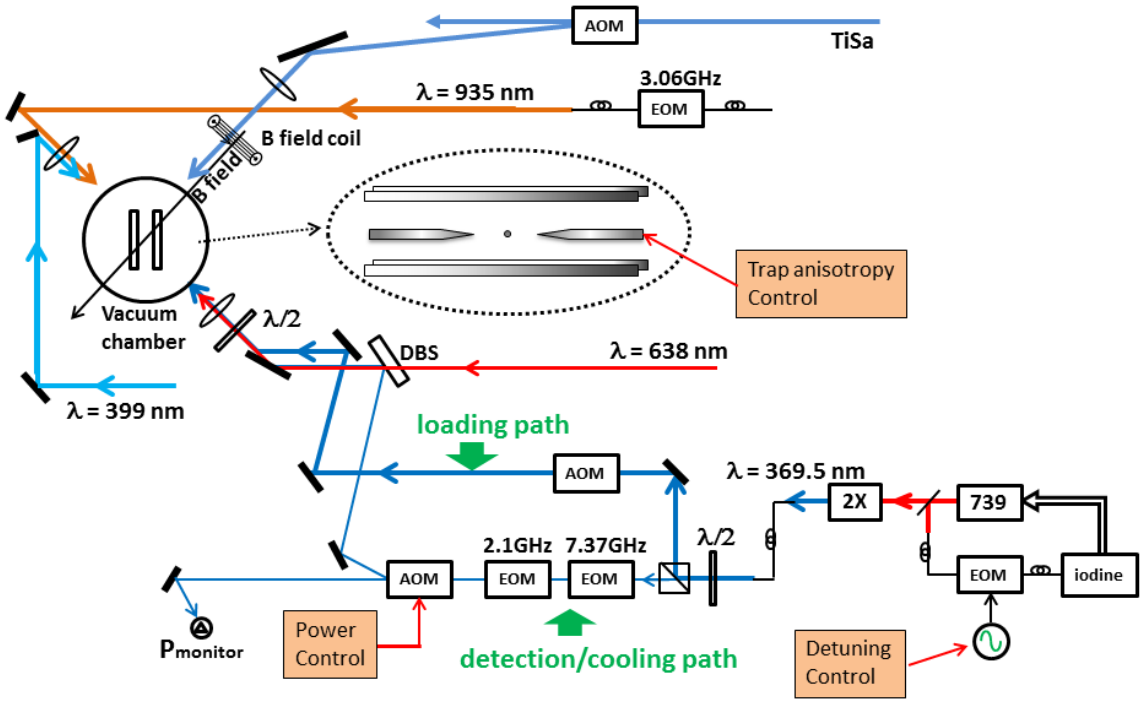

Figure 3.4: Sketch (top view) of the experimental setup, including the main laser-beam paths. In particular, the acoustic-optic modulator (AOM) used to control the power of the cooling laser is indicated, as is the offset frequency synthesizer for control of the detuning of the cooling laser. Inset is a magnified view of the trap electrodes (rotated by 90° relative to the actual setup). The voltages on the end-caps are used to control the trap anisotropy.

Before entering the trap, the loading laser-path goes through an 80-MHz acousto-optic modulator (AOM), which allows for power switching of the beam. The cooling and detection path first goes to an electro-optical modulator (EOM) that generates 7.37-GHz sidebands, the second of which couples the ${}^2S_{1/2}(F=0)$ and ${}^2P_{1/2}(F=1)$ states and enables the hyperfine repump. The beam then goes into a 2.1-GHz EOM, which can be used to drive the ${}^2S_{1/2}(F=1) \rightarrow {}^2P_{1/2}(F=1)$ optical pumping transition in order to initialize the ion into the ${}^2S_{1/2}(F=0, m_F=0)$ state. The optical pumping EOM is not used for the hopping experiments but is mentioned here for completeness since it is required to calibrate the magnetic field with microwave spectroscopy (see Ref. [31]). The beam out of the second EOM then goes through an 80-MHz AOM, which is used to control the Doppler-cooling power in the hopping experiments. The first diffracted order of the AOM is sent to the experiment while the zeroth order beam out of the AOM is directed to a power monitor to track for any drifts in the 369.5-nm power over the course of the experiment. Drift corrections are made in subsequent analysis where possible. The power of the cooling and detection beam can be varied over a range of typically 0-60 μW.

The beam passes through a half-wave plate, which allows the orientation of the linear polarization to be varied, and is then focused by a 100-mm or 150-mm lens into the trap through one of the eight viewports on the side of the vacuum chamber. The wavevector of the cooling and detection beam and the axial direction of the ion trap lie in a nominally horizontal plane and form an angle of $\sim 45^\circ$. The cross section of the laser-beam intensity along the axially aligned ion crystals has a full width at half maximum (FWHM) of about 50 μm, roughly equal to the end-to-end spacing of seven ions in a trap near the onset of the zigzag transition. A larger, more uniform beam in the axial direction would have been preferred, for example by using a cylindrical lens, but we have used what we had available.

To get a stable 369.5-nm laser for cooling and detection, the 739-nm laser in the TA-SHG system is stabilized before frequency doubling. While the doubling resonator cavity is locked to the 739-nm laser (the fundamental) to maintain the resonant enhancement of the doubling process, the 739-nm laser is also itself stabilized to the doubling cavity on a faster timescale to narrow its linewidth. To suppress long term drift in the frequency of the 739-nm laser, it is also locked to a hyperfine absorption line in molecular iodine using a saturation absorption technique [55, 53]. Since the particular iodine line that we have chosen to use is offset by about 10 GHz from that required for resonance with ${}^{171}\mathrm{Yb}^+$, a fiber

EOM driven by an HP8672 synthesizer at about 10 GHz is used to bridge the frequency gap. The first sideband of the EOM is used to lock to the reference absorption line; adjusting the synthesizer frequency while the laser lock is engaged allows the frequency of the 369.5-nm beam incident on the ions to be tuned. The synthesizer's frequency is adjustable with a resolution of 3 kHz and can be controlled manually, or remotely via GPIB.

As mentioned in Sec. 2.3, the primary 369.5-nm $^2S_{1/2}(F=1) \rightarrow {}^2P_{1/2}(F=0)$ cooling and fluorescence transition of $^{171}\mathrm{Yb}^+$ is susceptible to coherent population trapping. To suppress this effect, a magnetic-field coil of 100 turns next to the vacuum chamber provides a 5.9-G magnetic field transverse to the 369.5-nm laser wavevector (see Fig. 3.4). The magnetic field has been calibrated using microwave spectroscopy in previous experiments [31]. The polarization direction of the linearly polarized cooling and detection beam is also set to an angle $\theta_{BE} = 57.5^\circ$ with respect to the direction of the magnetic field to ensure near-optimal ion fluorescence [31].

3.2.3 Repump lasers

During the fluorescence and cooling process, an Yb^+ ion excited to the $^2P_{1/2}$ state has a branching ratio of 0.005 to decay to the low-lying, metastable $^2D_{3/2}$ state, as shown in Fig. 3.3. The ion can also end up in the low-lying $^2F_{7/2}$ state via a collision with a background gas atom [37, 38, 39]. To depopulate these states and return the ion back to the main cycle of $^2S_{1/2} \rightarrow {}^2P_{1/2}$ at 369.5-nm, we use both 935-nm and 638-nm repumping lasers.

The 935-nm laser (Fig. 3.4), also from TOPTICA (model DL100), acts on the $^2D_{3/2} \rightarrow {}^3D[3/2]_{1/2}$ transition. For $^{171}\mathrm{Yb}^+$, the laser is tuned to 935.1878 nm, as measured with a wavemeter, to provide the repump from $^2D_{3/2}(F=1)$ back to $^2S_{1/2}$ via the $^3D[3/2]_{1/2}$ state. A 3.07-GHz sideband generated by a fiber EOM is used to depopulate the $^2D_{3/2}(F=2)$ hyperfine state. Long-term drift of the 935-nm laser is prevented by locking to the stabilized 739-nm cooling and detection laser via a Fabry-Perot transfer cavity. The short term stability of the transfer cavity is also used to narrow the linewidth of the 935-nm laser. The 935-nm laser has a power of 2-3 mW and a waist diameter of 200 μm at the trap and is continuously on during all stages of the experiment. The frequency of the 935-nm laser, when set for $^{171}\mathrm{Yb}^+$, is only 140 MHz detuned from the repump transition for $^{172}\mathrm{Yb}^+$ and

no extra effort is required to obtain fluorescence of the $^{172}Yb^{+}$ isotope.

The 638-nm laser (Fig. 3.4) that serves for F-state repumping is also a DL100 model from TOPTICA. It has a power of 2 mW into the trap and a relatively large focused waist. The wavelength of the laser is ramped from 638.6105 to 638.6185 nm with a cycle time of 1 s to cover the hyperfine levels of the $^2F_{7/2} \rightarrow {}^1D_{2/5}$ transition for $^{171}Yb^{+}$ as well as the transition for the $^{172}Yb^{+}$ isotope. The 638-nm laser is continuously on during all stages of the experiment.

3.2.4 Titanium:Sapphire laser system

The last laser involved in the experiment is a frequency-doubled, stabilized Ti:Sa laser system (Fig. 3.4). The fundamental wave at $\sim$ 739 nm is produced by a Spectra-Physics/Sirah Matisse TX Lite, and is frequency-doubled to 369.5 nm in a Tehknoscan resonant doubler unit. The first role of this laser system is enhancing the loading efficiency. We tune the fundamental to a wavelength of 739.0530 nm (369.5265-nm doubled) and focus 12 mW of the UV doubled light into the trap, primarily to enhance the velocity capture of hot ions. The 369.5-nm photons can also assist in the second step of photo-ionization as noted above. After loading, the Ti:Sa laser is blocked during data-taking. Still, it is used occasionally in the experiment. Once in a while, the $^{171}Yb^{+}$ forms a molecule via a background gas collision, and we turn on the Ti:Sa system with full power to dissociate the molecule. We usually tune the fundamental wave to 738.964 nm (369.482 nm doubled) to take advantage of a published photodissociation resonance [56]; however, we have not verified if such a resonant behaviour exists. Typically, it takes less than 10 min to bring back the $^{171}Yb^{+}$. During the hopping experiment, we also occasionally reduce the power of the Ti:Sa system and tune its frequency to verify the identity of the $^{172}Yb^{+}$ impurity in the ion crystals.

3.3 Detection setup

A custom UV microscope with a vertical imaging axis is used to monitor the ion crystals in the trap (Fig. 3.5). Scattered 369.5-nm photons from the ions are collected by an anti-reflection-coated UV objective lens with a 20-mm focal length and a numerical aperture of 0.23. An intermediate image of the ions is formed 20-30 cm behind the objective, and re-

imaged by a pair of 75-mm lenses onto a Hamamatsu photo-multiplier-tube (PMT), or onto an intensified charge-coupled device (ICCD) camera (Princeton Instruments PI-MAX2). The PMT is used for fluorescence counting during experiment calibration steps and for micromotion nulling using the correlated photon technique [57]; the ICCD camera is used to monitor the hopping dynamics of the ion crystals. A 600-μm pinhole in the intermediate image plane (Fig. 3.5) suppresses laser scatter from the trap electrodes, while a dichroic mirror is used to filter out 638-nm and 935-nm photons from the imaging path.

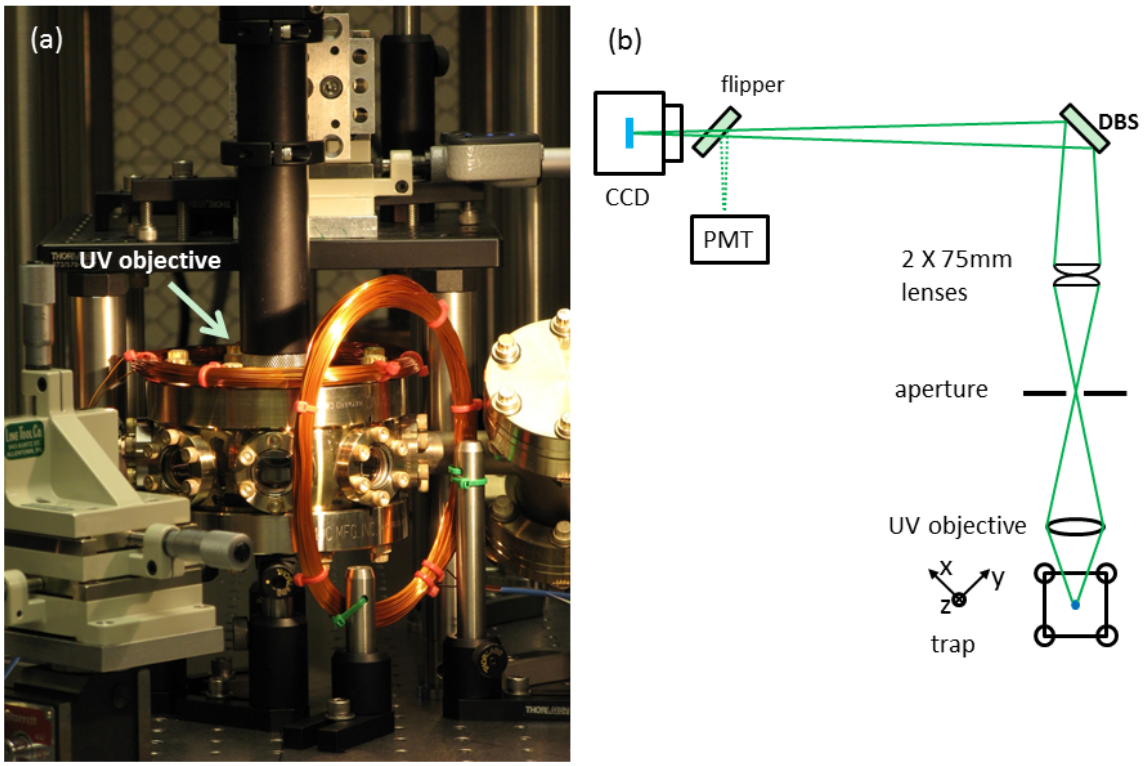

Figure 3.5: Imaging setup which views the ions from above the trap. (a) Photo of the vacuum chamber and location of the UV objective lense. (b) Sketch of the optical path of the imaging system.

Total magnification of the imaging system is about 150. Calibration of the length scale of the CCD images is made by comparing the axial spacing of trapped ions in the CCD image to that calculated from the measured secular trap frequencies. Due to the broken

symmetry in the shape of the transverse confining potential, the 2-D zigzag pattern in ion crystals at high α lies in a plane determined by the axial direction and the weaker transverse direction (see Fig. 3.6). This plane does not lie transverse to the vertical imaging axis of the camera and its orientation is not accurately known *a priori*. The oblique viewing angle is determined by comparison between the observed zigzag displacement to that predicted by theory. As will be shown in Chp. 4, this angle is found to be close to 45°, meaning that the principal axes of the transverse pseudo-potential match closely to x and y axes as defined in Fig. 2.1.

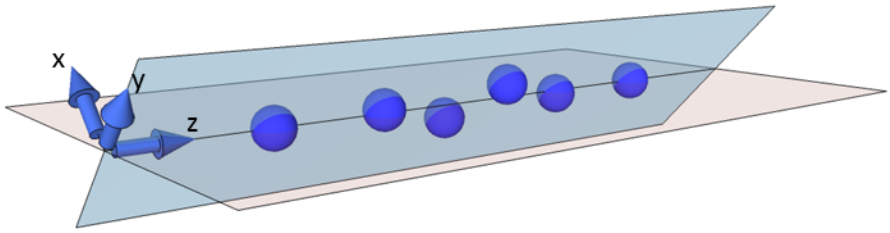

Figure 3.6: Sketch of a six-ion crystal in the zigzag phase. The 2-D zigzag pattern lies on the blue plane, which overlaps with the y-z plane as defined in Fig. 2.1, and makes an angle of 45° with the horizontal plane (red).

The bin size of the CCD images is set to 8×8 pixels to increase the rate of frame readout while still maintaining good spatial resolution. To further speed up the rate, the readout of the CCD images is also limited to a region of interest around the ion crystal of typically 100×50 binned pixels. A 40-ms exposure time followed by 28.3-ms readout gives a net frame period of 68.3 ms. Movies containing 3000 to 20000 images, lasting 3 to 23 min, are acquired to measure the hopping dynamics in an ion crystal, and repeated as necessary for additional statistics.

3.4 Basic experimental procedure

A basic daily procedure is outlined in this section to illustrate how a typical experiment to study hopping dynamics is done.

At the start of each day before loading ions, all lasers are turned on and optimized. Then a single $^{171}Yb^{+}$ ion is loaded into a trap with the two end-cap voltages set to 9.193 V and 10.120 V, and several alignment steps and daily calibrations are performed. The single ion is used to align the 369.5-nm cooling beam and 935-nm repump beam onto the centre of the trap and to verify proper operation of the lasers and system according to, for example, typical peak fluorescence counts. Micromotion is monitored regularly using the photon correlation technique during calibration experiments, and the dc-bias voltage on one of the trap rods is adjusted as needed to suppress the effect of micromotion on the ion fluorescence. As mentioned earlier, typical bias voltages are 0-200 mV and daily changes over the course of data taking were typically 20 mV or less. Infrequently, we have also done a full micromotion nulling with a combination of techniques [57] to place the centre of the trap close to the rf minimum in all dimensions. We avoid doing this regularly because it requires varying the rf power to the trap. In a separate test, we have found that a transverse voltage bias of up to ~ 20 mV that introduces micromotion in the direction that has no effect on the fluorescence does not show an observable effect on the hopping.

A calibration experiment with a single trapped $^{171}Yb^{+}$ ion is done to identify the offset frequency associated with the resonance of the 369.5-nm $^{2}S_{1/2}(F=1) \rightarrow ^{2}P_{1/2}(F=0)$ transition. The ion exhibits a characteristic half-lineshape shown in Fig. 3.7 due to Doppler-cooling and -heating effects [58], and we identify the drop-out in fluorescence as resonance. We do not scan the whole resonance lineshape each day but simply manually tune the synthesizer over the $^{171}Yb^{+}$ resonance to locate the drop-out point. The location of the drop-out exhibits a repeatability of better than 100 kHz in the UV over the course of at least a day. The resonance location is used to infer detuning of the cooling and detection laser for the remainder of the day's data.

Once the resonance location for $^{171}Yb^{+}$ is determined, fluorescence measurements of a single trapped $^{171}Yb^{+}$ ion are performed as a function of the power of the 369.5-nm cooling and detection laser. The laser detuning is typically fixed at -8 MHz for these measurements. The power scan is an automated procedure that steps the rf power to the AOM used for controlling the power of the cooling and detection laser. The fluorescence-verse-power scans are fit to the theory in Eqn. (2.13) in order to calibrate the central intensity of the laser at the trap in terms of an equivalent saturation power p_0 [31]. That is, for a given laser power, the ratio p/p_0 gives the on-resonant saturation parameter s_0 (Sec. 2.3)

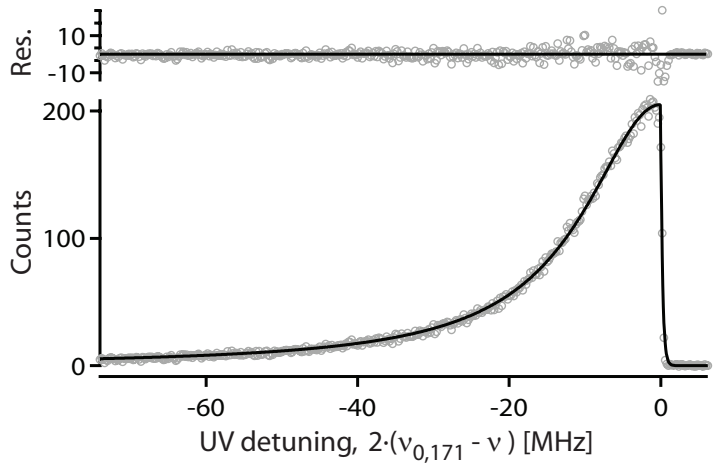

Figure 3.7: Typical half-lineshape for the 369.5 nm $^2S_{1/2} - {}^2P_{1/2}$ transition of a single trapped $^{171}Yb^+$ ion in our experiment, reproduced from [31].

at the centre of the laser profile. Figure 3.8 shows an example of a power scan and fit. The fit to theory also relies on a prior calibration of the magnetic field at the ion as well as a daily calibration of the AOM response using a photodiode power meter from Ophir. The power monitor for the cooling and detection beam, already mentioned above, continues throughout the day to monitor power drifts relative to the calibration point.

With the initial calibrations complete, an isotopically selective photo-ionization technique [54] is then used to load a given number of $^{171}Yb^+$ ions and to add a single $^{172}Yb^+$ impurity. During the loading process, the 399-nm beam, the 369.5-nm cooling and detection beam, the 369.5-nm loading beams, the 10 mW 369.5-nm doubled Ti:Sa beam and the 638-nm and 935-nm repump beams are all introduced into the trap. The 399-nm laser is first tuned close to the resonance of $^1S_0 - {}^1P_0$ transition of the neutral ^{171}Yb atom (near 398.9111 nm) to provide the first step of photo-ionization. As mentioned above, the 369.5-nm photons from the high-power loading beam and from the doubled Ti:Sa beam are presumed to dominate the second step of photo-ionization and ^{171}Yb atoms are ionized and trapped. The cooling and detection laser is locked ~ 8 MHz below resonance during the loading procedure. With the help of the doubled Ti:Sa, which is tuned 1.0 GHz below resonance to provide a large velocity capture range, the trapped ions are Doppler-cooled

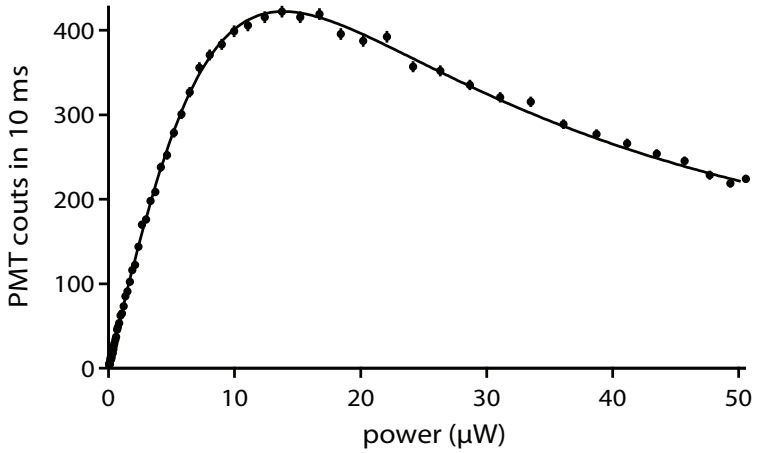

Figure 3.8: Power scan for calibration of the laser intensity. The laser detuning is fixed at -8.12 MHz, and magnetic field is fixed at 5.9 G. The fluorescence is predicted to peak at $p/p_0 = 9.3$ by the theory. Solid curve is the fit to the theory, giving $p_0 = 1.51$ μW. An overall amplitude parameter is included in the fit to account for the photon-collection efficiency.

to the centre of trap. Optimizing the various laser parameters, ions will, for the most part, load and crystallize automatically, allowing us to cut off the loading at a given number of ions. After loading the requisite number of $^{171}Yb^+$ ions, the 399-nm laser is then tuned to the resonance of ^{172}Yb to add a single $^{172}Yb^+$ impurity isotope to the crystal. This isotope is sympathetically cooled by the $^{171}Yb^+$ ions in the trap and becomes integrated into the crystal array. We verify the $^{172}Yb^+$ identity of the impurity by tuning the doubled Ti:Sa laser at low power to the $^{172}Yb^+$ resonance, where the impurity ion fluoresces. At this point, the 369.5-nm loading beam and the doubled Ti:Sa beam are turned off and the paths are physically blocked so that leakage light does not affect the hopping measurements. It takes typically a total time of 1-2 hours to load the desired crystal and impurity defect, but they last for the 10-15 hours required for data-taking.

During the hopping experiments, the 369.5-nm detection and cooling beam, as well as the 935-nm and 638-nm repumping lasers are always active. The cooling and detection laser remains locked near to the $S-P$ transition of the $^{171}Yb^+$ ions. The $^{172}Yb^+$ impurity in a crystal of $^{171}Yb^+$ ions does not interact strongly with the cooling and detection laser

and remains dark, since the laser and its 7.37-GHz modulation sidebands used for hyperfine repumping are at least 3.5 GHz detuned from the $^{172}Yb^{+}$ resonance. The $^{172}Yb^{+}$ ion is, however, sympathetically cooled through its Coulomb interaction with the $^{171}Yb^{+}$ ions [51, 52].

Figure 3.4 summarizes the main parameters that we adjust during the experiments to control and assess hopping. To reiterate, a synthesizer driving the AOM in the cooling and detection path controls the optical power for Doppler cooling of the $^{171}Yb^{+}$ ions in the crystal. A synthesizer in the lock setup of the cooling and detection laser provides the ability to adjust the detuning for the Doppler cooling. By controlling the power and detuning of the Doppler-cooling, one can affect the kinetic energy of the ion crystal. The end-cap voltages of the trap are used to adjust the axial secular trap frequency, thus changing the asymmetry parameter of the trap potential and the Coulomb interactions between the ions. These control parameters set the "environment" for the ions, and the resulting hopping behaviour is recorded in a sequence of images taken with an ICCD camera. As part of the data collection, the effect of micro-motion on the fluorescence is suppressed by fine tuning of the dc-bias voltages on the rods of the trap. The doubled Ti:Sa laser is used occasionally to confirm the isotopic identity of the impurity ion. Finally, once to a few times per hour, a background-gas collision forms a molecular ion with one of the $^{171}Yb^{+}$ ions. The molecular ion is localized in the ion crystal and does not fluoresce, but, through its larger mass, can reveal itself by inducing a structural zigzag deformation in a linear crystal. The doubled Ti:Sa laser system is then used to photo-dissociate the molecules [56] and recover the Ytterbium ions. This allows the same ion crystal to be used for multiple hours. The hopping behaviour as a function of the control parameters is presented in the following chapter.

Chapter 4

Hopping Behaviour

In this chapter we discuss in detail the hopping behaviour of a single $^{172}Yb^{+}$ impurity ion within a crystal of $^{171}Yb^{+}$ ions and, in particular, how the hopping responds to several aspects of the experimental environment of the ion crystal. As noted in the introduction, these studies are built on earlier hopping experiments with two ions in Ref. [21] and fit into a range of previous experiments studying crystallization and melting dynamics in ion traps. At the end of the previous chapter, we have detailed our basic experimental procedure required to study hopping. This chapter begins with a description of how the site-to-site hopping is observed using camera images of the ion crystal. The next two sections concentrate on developing an automatic way to extract the hopping trajectory of the impurity ion from those images. Following is a discussion on various descriptive statistics that are derived directly from the trajectory of the impurity, including the distribution of dwell times at a given site, the hopping destination and the spatial dependence of on-site probability and hopping rate. Finally, we demonstrate how the hopping rate of the impurity depends on the power and detuning of the Doppler-cooling laser applied to the crystal and how the hopping rate depends on the anisotropy of the trap confining the ion crystal. Although there are some technical complications to this first edition of these kinds of experiments, we conclude by discussing how several features of the observed hopping dynamics are likely to be intrinsic to the structure of the ion crystal.

4.1 Acquiring hopping data

As has been discussed in Sec. 3.4 of the previous chapter, calibrations of the detuning Δ of the Doppler-cooling laser and of its power p in terms of saturation power p_0 are performed with a single trapped $^{171}Yb^+$ ion at the start of each day. (For convenience, "Doppler-cooling laser" or "369.5-nm laser" will be used to refer to the "cooling and detection laser" of Chp. 3.) A crystal of $^{171}Yb^+$ ions is then loaded into the trap. Because of the indistinguishability of the same ion species, many behaviours of the ion crystal such as site-to-site hopping are actually unobservable. In order to see these behaviours, we introduce a single, non-fluorescing "tag" ion into the crystal of fluorescing $^{171}Yb^+$ ions [2]. In our case, a single $^{172}Yb^+$ impurity is chosen as the tag ion to have nearly identical mass [59]. We can relatively easily add such an isotopic impurity to the ion crystal and verify its identity with the methods described in the previous chapter.

The ion crystal in the trap displays various dynamical behaviours, among which site-to-site hopping is our primary interest here. By hopping, we specifically point to the event where the impurity ion swaps positions with another ion in the crystal in a short amount of time, without the observable loss of the localization of the ion crystal. The one caveat to this statement is the hopping process occurs much faster than the 68-ms time between camera frames in our setup (Sec. 3.3), and so we do not have access to the full trajectory of the ions during the hopping event.

Under good cooling conditions where the power of the Doppler-cooling laser is sufficiently low and the detuning is near half of a linewidth below resonance, the ion crystal is quite stable against hopping. To induce hopping, we first adjust the end-cap voltages to obtain a trap with anisotropy parameter α near but below the onset of the zigzag transition. The 369.5-nm laser is tuned close to the $^{171}Yb^+$ resonance, and the laser power is raised to a large saturation value, both of which compromise the Doppler cooling in a controlled fashion and elevate the kinetic energy of the ions [20]. Under these conditions of a "warm" ion crystal, hopping dynamics are initiated. Using an intensified CCD camera, we record image sequences of the ion crystal at different experimental parameters and investigate how the hopping dynamics are influenced by the laser- and trap-induced "environment". Image sequences of between 3,000 and 20,000 images, lasting between 3 and 23 minutes respectively, are acquired in a continuous data set and are repeated as necessary for additional

statistics.

Figure 4.1(a) shows a sequence of images for a six-ion crystal in a trap with frequencies {442.8, 426.4, 141.2} kHz, and at a laser detuning of $\Delta/2\pi = -1.2$ MHz and a scaled laser power of $p/p_0 = 28$. The crystal is generally stable and the ions' positions well defined (Fig. 4.1(b)), although the ions are clearly more delocalized than in a reasonably well-cooled state (Fig. 4.1(c)). The impurity ion, which is identified by a lack of fluorescence at a given site, is observed to hop within the crystal from image to image, for example Fig. 4.1(a) frames 7-8, and during the exposure of a single image such as frame 4. The majority of events involve a relocation of the impurity without observable loss of crystal localization. Intermittently, the crystal delocalizes partially and loses contrast or, in more extreme cases, makes a transition to a disordered cloud state followed by re-ordering (Fig. 4.1(a) frames 17-20). For the parameters of Fig. 4.1(a), these events typically occur about every 20 s and form the bulk of the non-hopping events. Other low-level background events include a $^{171}Yb^{+}$ ion going dark through collisional population of the $^2F_{7/2}$ state [39], cleared out by the 638.6-nm laser, and the rarer molecule-forming collisions already mentioned in Sec. 3.2 in Chp. 3.

4.2 Image analysis

To identify the state of the crystal including the location of the dark impurity, we first analyze the images by integrating the fluorescence in a rectangular region around each crystal site. Figure 4.2(a) shows the integrated fluorescence for different sites in a six-ion crystal with integration regions as indicated in Fig. 4.2(b). At time t_1=135.0 s, only site 2 has low fluorescence counts. Since the impurity is dark, it can be expected that at this moment the impurity is located at site 2, which is justified by looking at the corresponding image of the crystal in Fig. 4.2(b). However, some added effort is required to ensure that situations where the ion crystal is non-ideal or absent are not misinterpreted. For example near time t_2=85.5 s, all the sites have low fluorescence counts. In this case, there has been a loss of crystallization and the ions are in a disordered cloud state (Fig. 4.2(c) and (d)). In general, images with more than one dark site correspond to situations where there has been a loss of crystallization, one of the $^{171}Yb^{+}$ ions has been pumped into the metastable F-state, or one of the $^{171}Yb^{+}$ ions has formed a molecule with a background-gas atom.

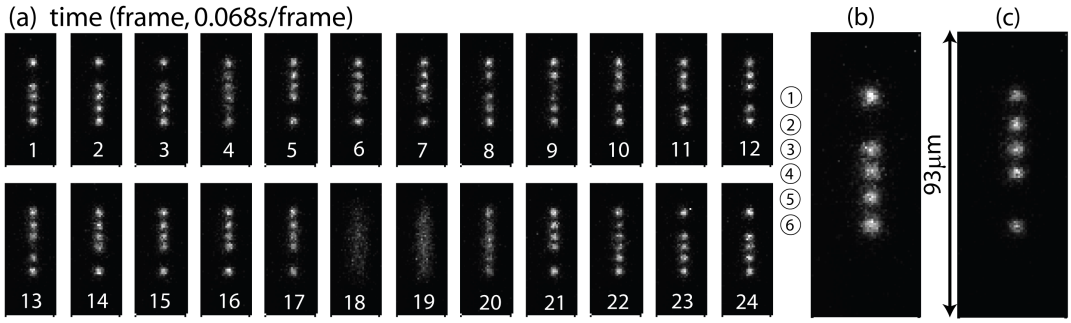

Figure 4.1: Activated hopping in a six-ion crystal of five $^{171}Yb^{+}$ ions and a single $^{172}Yb^{+}$ impurity defect. (a) Example sequence of CCD image frames (40 ms exposure, 28.3 ms readout, pixels hardware-binned 8×8) showing typical behaviour. Trap frequencies are $\{442.8, 426.4, 141.2\}$ kHz, and laser parameters are detuning $\Delta/2\pi = -1.2$ MHz and power $p/p_0 = 28$ where $p_0 \approx 1.6\,\mu$W. (b) Enlarged version of frame 1 from part (a). Crystal sites are labeled as indicated. (c) The same crystal as in (a) and (b) but within an expected factor of 2 of the Doppler-cooling limit ($\Delta/2\pi = -8.2$ MHz, $p/p_0 = 9.0$). Gray scales for (b) and (c) approximately span the dynamic range of their respective images. Fits to ion images in the centre of the crystal give a transverse FWHM of 5.0 μm in (b) and 4.2 μm in (c); the latter is close to the minimum observable.

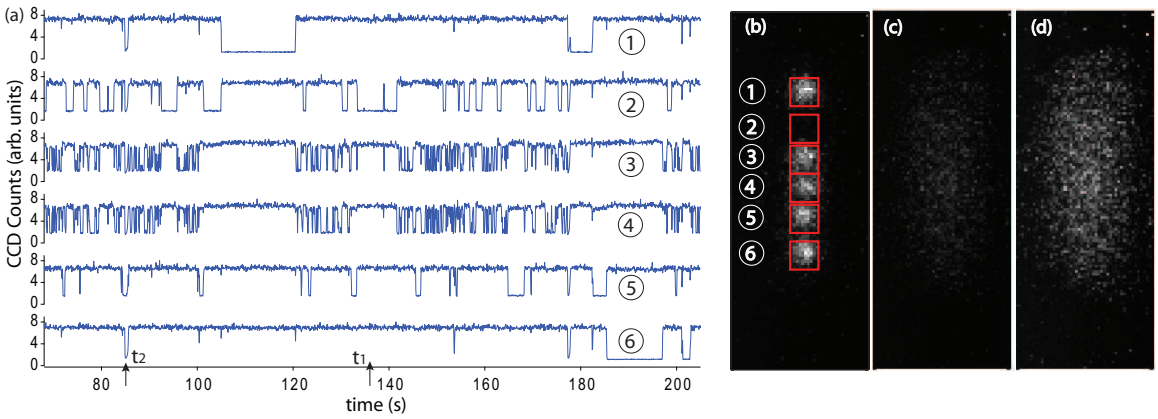

Figure 4.2: (a) Integrated fluorescence as a function of time at each crystal site in a six-ion crystal with one defect. Experimental parameters are the same as in Fig. 4.1(a). (b) Image of the crystal at time $t_1 = 135.0$ s. The six rectangular outlines show integration regions used to calculate integrated fluorescence for different sites in (a). The gray scale approximately spans the dynamic range of the image. (c) Image of delocalized ion cloud near time $t_2 = 85.5$ s, with gray scale same as (b). (d) The same image as (c) but shown with an enhanced gray scale in order to see the ion cloud.

A proper design of the analysis should be able to exclude images corresponding to these situations where the crystal is absent or not ideal.

To help with filtering out these cases, we also consider the contrast in fluorescence between the centre and corners of the rectangular region defining each crystal site. A higher contrast implies a more localized ion at the site. Rather than assessing each site individually, it is sufficient to consider the total fluorescence and total contrast summed over all sites. These two values, in fact, provide an efficient two-dimensional discriminator for good crystals. Figure 4.3 illustrates how to make use of this 2-D discriminator to filter out images with a non-ideal crystal. For each frame in a given image sequence, the total fluorescence and total contrast are calculated, and this pair of values corresponds to a single point in the fluorescence-contrast plane. The distribution of the points typically forms a pattern with a high density of points on the upper right of the plot with high fluorescence and good contrast, and with a "tail" extending to the lower left corner. Similar patterns are consistently observed for all data sets.

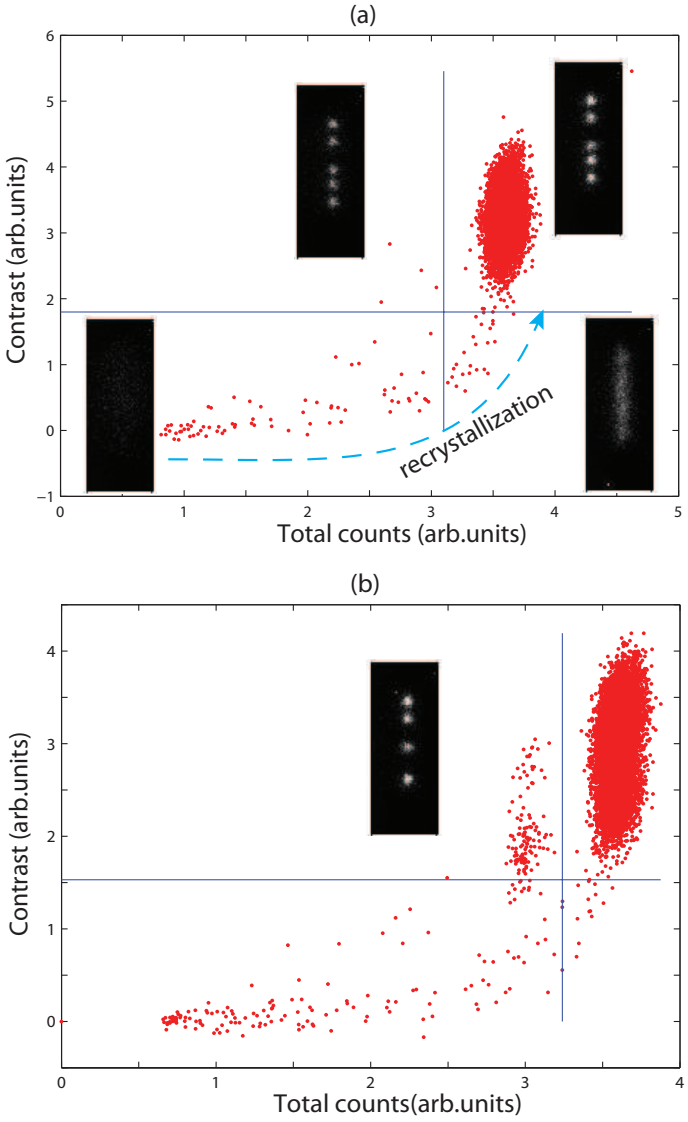

Figure 4.3: Illustration of the two-dimensional fluorescence-contrast discriminator. (a) Typical distribution of fluorescence counts and contrast in a sequence of 10,000 images of a six-ion crystal with one impurity defect. Experimental parameters are the same as in Fig. 4.1(a). Example images are included to show the typical behaviours for different regions in the count-contrast plane. An arrow shows the path of re-crystallization. (b) Example of a distribution of images that includes a cluster of images lying in the upper left-hand corner of the count-contrast plane. The distribution consists of a sequence of 10,000 images. Experimental parameters are the same as in (a).

From experience, we find that a choice of fluorescence-count and contrast values just to the inside edge of the high density region can serve as a very good discriminator of a well-localized crystal with all $^{171}Yb^{+}$ ions bright (see Fig. 4.3). The two values divide the counts-contrast plane into four regions and example images are provided in Fig. 4.3 to show the typical state of the crystal associated with each region. The upper right region, where the total counts and contrast are both high, corresponds to the case of "good" crystals where the ions are reasonably localized and the $^{171}Yb^{+}$ ions are bright. The lower right region with high total counts but low contrast is typically associated with partially localized yet disordered clouds. The points with low fluorescence and low contrast in the lower left region correspond to a fully delocalized cloud-state with the ions in relatively large orbits. One of the interesting side notes to plots such as Fig. 4.3 is that they provide a nice illustration of the melting and crystallization behaviour of ion crystals [18]. Typically, during loss of crystallization, a point on the count-contrast plane representing the state of the crystal moves suddenly from the upper right region to the lower left region. The re-crystallization, however, is a relatively slow process that follows the path in the fluorescence-contrast plane indicated in Fig. 4.3(a). Along the path, the disordered ion-cloud is first re-cooled and contracts in size, bringing up the level of fluorescence within the integration region. Finally, the ion cloud makes a transition to an ordered crystal with high contrast to complete the recovery process. Usually in the upper left region there are only a few scattered points, often associated with a transition within one frame from a good crystal to a disordered cloud. In this case, the fluorescence level is low for part of the exposure time, leading to a dimmer image of the crystal as in Fig. 4.3(a). However, if one sees a significant number of points in this region, as in Fig. 4.3(b), it often implies that there is a sub-sequence of images in which one of the $^{171}Yb^{+}$ ions has gone dark, either by going to the metastable F-state or by molecule formation.

In summary, total fluorescence counts and contrast provide a very useful two-dimensional discriminator of a well-localized crystal with all $^{171}Yb^{+}$ ions being bright. Typically, we can acquire 10,000 images, covering 11 min, in which more than 95% of the frames show an acceptable crystal. For images where there is a well-defined crystal, the location of the impurity ion is identified by the darkest location. An additional layer of analysis is performed to extract a small number of missed events occurring during exposure times. The number of these events is low as long as the hopping rate is not too fast compared to the

camera frame-rate. In practice, we include in our results data sets with hopping rates up to about 10 Hz. As the hopping rate approaches a significant fraction of the camera frame rate ($\sim$ 15 Hz), the effect of the finite camera exposure and readout times becomes significant and, as will be discussed in the next section, leads to a downward bias in the measured hopping rates among other effects. In any case, the end result of the image analysis, shown in Figure 4.4, is a hopping trajectory for the impurity in the crystal as a function of time with occasional gaps due to loss of crystallization or otherwise.

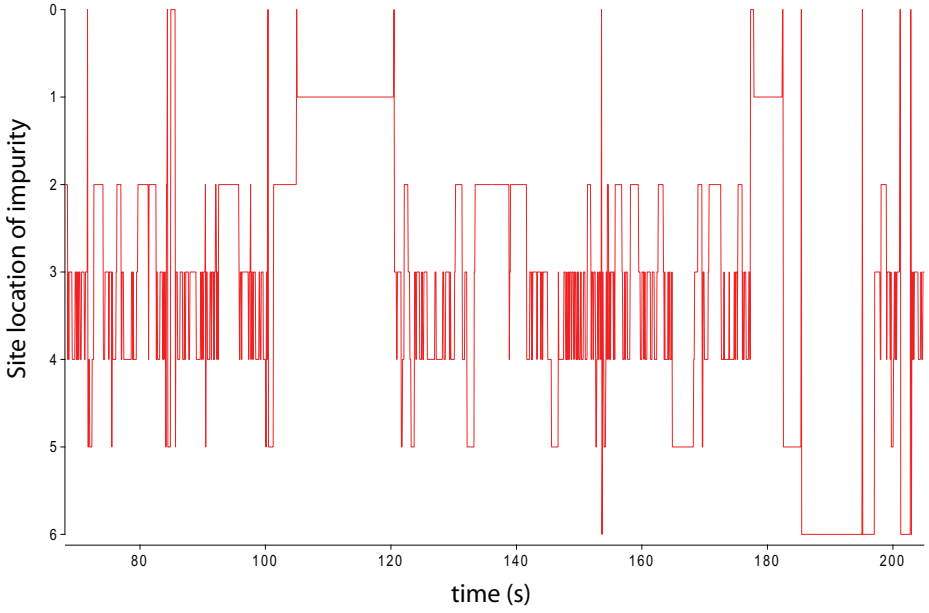

Figure 4.4: Trajectory of the impurity in a six-ion crystal extracted from image analysis. Note that we use "site 0" to indicate situations in which the crystal is ill-defined. Experimental parameters are the same as in Fig. 4.1(a).

4.3 Hopping characteristics

4.3.1 Distribution of impurity dwell-times at a site

From the trajectory of the impurity ion, the distribution of time intervals for which it dwells at a given crystal site can be extracted. Figure 4.5 shows an example of the typical dwell-

time distributions for different sites in a six-ion crystal. The termination of the dwell interval has not been filtered in favour of hopping events since they already dominate the statistics. One can see that the dwell-time distribution is broader as one moves from the centre to the outer regions of the crystal and these behaviours are roughly symmetric about the centre. This indicates a longer average dwell time for the outer sites. Although the outer sites have low statistics, a decaying distribution is still roughly observable for all sites. An exponential distribution would be expected in the case of a time-independent hopping rate away from a site, as might occur for a thermally activated process, and exponential behaviour has been observed previously for hopping in two-ion crystals [21]. In Fig. 4.6, we show fits to an exponential for the dwell-time distributions at site 4 and site 5 from Fig. 4.5. The fits match the data qualitatively well but typically show an excess tail of dwell-time events at longer times. As a result, the decay time constants obtained from the fits are 1.2–2 times lower than the average dwell times, as calculated directly from the distributions. For example, for the distributions at sites 4 and 5 in Fig. 4.6, we obtain fit time constants of 0.151(2) s and 0.53(3) s but average dwell times of 0.23 s and 1.07 s respectively. Therefore, to avoid systematic errors associated with fitting, we simply calculate the average dwell time $\langle \tau_i \rangle$ from the distribution of dwell times for the i^{th} site and use its inverse, $\langle \tau_i \rangle^{-1}$, to characterize the hopping rate [60].

4.3.2 Effect of the finite camera frame rate

One might imagine that the finite frame rate of the CCD camera could be responsible for the systematic deviations of the dwell-time distributions from exponential behaviour. We divert here from the main discussion to assess how the finite camera rate affects the hopping statistics acquired. To do so, we simulate the simplest case of hopping, namely in a two-ion crystal, with Monte-Carlo method, where at each simulation step (corresponding to 1 ms in real time) the ions can swap positions with a small, fixed input probability proportional to the hopping rate. The repetitive imaging sequence of the camera is included in the model with an exposure time of 40 ms, followed by a readout time of 28 ms, matching what we use in the experiment. Of the two ions in the simulation, one is assumed to be "dark". It is deemed to be in a certain site in a camera frame if it shows up in that site for more than half of the exposure time, in close analogy with the analysis procedure used in

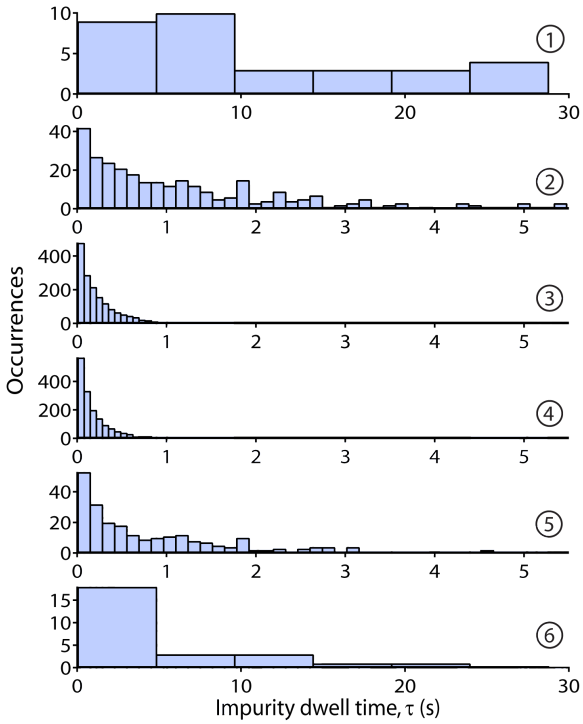

Figure 4.5: Distribution of dwell-times at different sites in a six-ion crystal. The central four sites share the same time scale so the distributions for these sites can be directly compared with each other. The two outer sites of the crystal use a larger time scale to match the dwell-time behaviours there. Bin sizes are adjusted according to the available statistics at each site. Experimental parameters are the same as in Fig. 4.1(a).

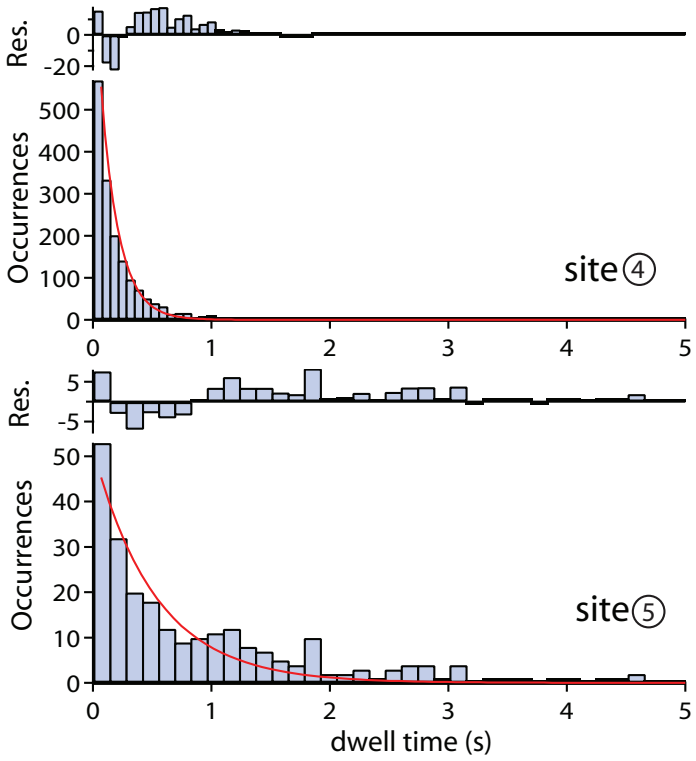

Figure 4.6: Dwell-time distributions for the two central sites (site 4 and 5) in a six-ion crystal. Histograms are obtained from 20,000 images. Experimental parameters are the same as in Fig. 4.1(a). The plot for site 4 contains 1,235 instances, including 17 transitions to a decrystallized state; for site 5, the plot contains 176 instances, including 9 transitions to a decrystallized state. Solid lines are exponential fits with time constants of 0.151(2) s and 0.53(3) s for site 4 and site 5 respectively. Fit residuals are included above each plot.

the actual experiment. The simulation automatically includes the dead-time effect of the camera since, during the readout time, the ions' hopping is ignored by the camera.

We vary the input hopping rate in the simulation and investigate the reliability of the camera in reproducing the expected behaviour. In Fig. 4.7, we compare the distribution of actual hopping events generated by the simulation to that obtained after applying the camera "filter". For Figs. 4.7(a)–(c), the input hopping rate in the simulation is set to 0.83 Hz, 1.7 Hz and 8.3 Hz, corresponding to a typical range in the experiment. As would be expected, exponential fits to the actual distributions work well and correctly reproduce the input hopping rates. Compared to the actual distributions, the camera-derived distributions consistently show fewer counts at shorter dwell times while extra (false) counts are registered at longer dwell times. However, since these extra counts only correspond to about 5% of the number missing at shorter dwell times, the dominant effect is missing counts at short dwell times. (Note that the effect of false counts will be addressed later). In Fig. 4.7(a)–(c), the missing counts correspond to {7, 12, 46}% of the total number of actual events at shorter dwell times and {7, 11, 43}% of the total number of actual events generated in the simulation. The discrepancy between the actual hopping behaviour and the camera-derived behaviour gets larger at higher hopping rates, as expected; however, in this Monte-Carlo simulation, we find that the dwell-time distributions acquired with the camera follow an exponential distribution very well even for the highest hopping rate shown in Fig. 4.7(c). This is in contrast to the case in the experiment, where there is usually an excess tail of dwell-time events at longer dwell times. The inclusion of the camera mechanism thus does not seem to explain the typical deviations apparent in the residuals in the experimental data (see Fig. 4.6).

Moreover, in the experiment, the average dwell time is typically $\sim$2 times larger than the fit constants in the 1-to-2 Hz range of hopping rates. To see if this is also true in the simulation, we compare in Fig. 4.8 the camera-derived hopping rate calculated directly from the inverse of the average dwell time and that obtained from the inverse of the fit dwell time. Both the hopping rates calculated from these two methods match the actual rate very well for low hopping rates (see Fig. 4.8), and the discrepancy grows at higher hopping rates, consistent with the discussion above. Figure 4.8 also shows that the hopping rate obtained from the fits to the camera-derived distributions is generally higher than the inverse of the average dwell time, which is the same trend observed in the experimental

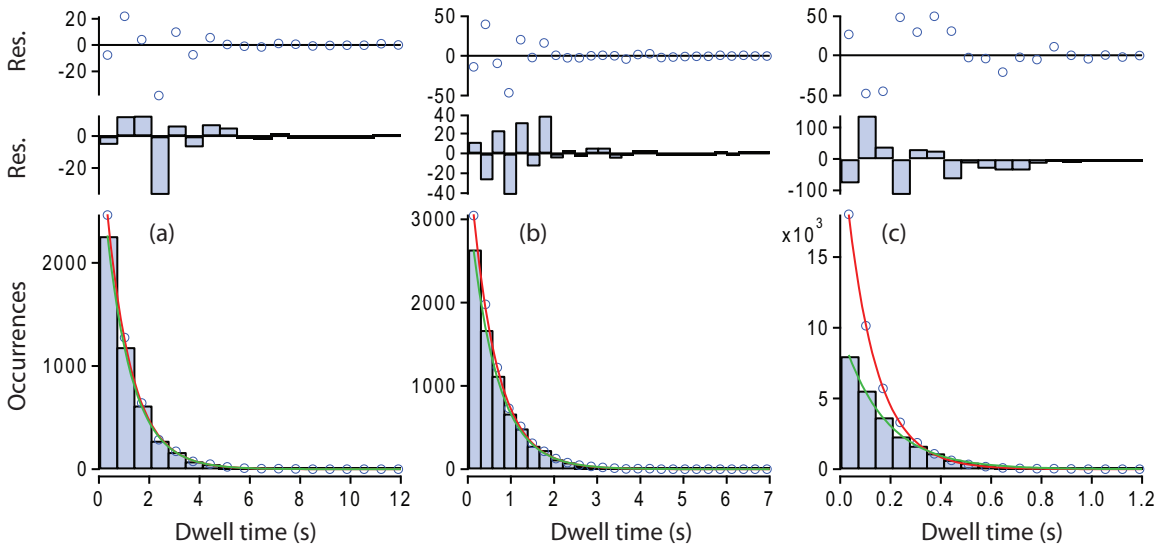

Figure 4.7: Simulation of the camera's effect on dwell-time distributions for two-site hopping. From (a) to (c), the input hopping rate for the simulation is set to 0.833 Hz, 1.667 Hz and 8.33 Hz. Open circles show the statistics of the actual events generated by the simulation. Bars are the statistics derived from simulated camera frames (exposure time 40 ms, readout time 28 ms). Fits to the exponential function for the statistics from actual events and camera-observed events are shown in red lines and green lines respectively. Also included are the residuals from the fits. Hopping rate for (a)–(c) obtained from fit time constants are {0.822, 1.678, 8.375} Hz and {0.806, 1.603, 5.848} Hz for actual events and camera-observed events, respectively.

results. However, for hopping rates of 1–2 Hz in the simulation, the calculated rates from the two methods differ by less than 2%, which is much less than what is observed in the experiment. Considering this difference between the simple Monte-Carlo simulation and the experimental results, there are likely some other factors in the experiment that result in the deviation from a simple exponential model.

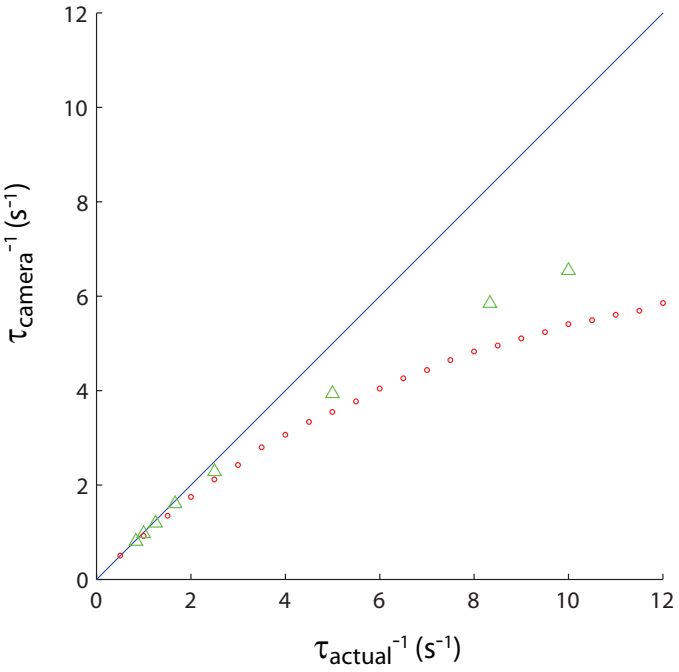

Figure 4.8: Simulation of camera response at different hopping rates. Red open circles are the inverse of the average dwell time obtained from the simulation including the "filter" effect due to the finite frame rate of the camera. Green triangles are obtained from the fit of the camera-obtained dwell-time statistics. Blue line shows the expected response of an ideal camera (infinite camera rate).

Eventhough the simulation does not explain the shape of the dwell-time distributions in the experimental data, it is still worthwhile to point out the other effects to be expected due to the finite camera frame rate. The general trend in Fig. 4.8 shows that the camera frame rate is expected to suppress the observed hopping rate from the actual value by a factor of 1.25 up to 4-Hz hopping rate and by a factor of ~ 2 at an 8-Hz hopping rate.

Therefore, we expect the effect of the camera "filter" is to smooth out the dependence of the hopping rate on experimental parameters. Finally, we have extended the two-ion Monte-Carlo simulation to the case with 3 ions with nearest-neighbour hopping and see that, in addition to the suppression in observed event count, the camera also produces events that are mislabeled. For example, non-nearest-neighbour hopping events are "observed" by the camera even though they are absent in the unfiltered data. The effect does not seem very strong for our experiment parameters (see below).

4.3.3 Spatial dependence of the hopping behaviour

We now return to a discussion of the experimental results. From the trajectory of the impurity defect, the hopping outcome as a function of initial position can also be obtained and is shown for seven and six ions in Fig. 4.9. Only those events corresponding to well-defined initial and final crystals are included, which comprise the large majority of events. The interior crystal sites are clearly seen to be the most active and dominate the behaviour. For the case of seven ions where the interior three sites exhibit most of the hopping, an impurity on either side of the central site tends to hop towards it. An impurity in the centre, which can hop readily to two nearby sites, is found qualitatively to have a shorter average dwell time (0.45 s in the centre compared to 0.70 s and 0.62 s on either side).

Non-nearest-neighbour hopping events are observed in the hopping outcome. For example, in Fig. 4.9(a), there are 140 instances where the impurity is deemed to hop from site 3 to site 5; this corresponds to about 20 % of the total number of hopping events from site 3. For comparison, we have studied a Monte-Carlo simulation with 3 ions, where only nearest-neighbour hopping is allowed. We set the hopping probability in the simulation so that the camera-derived central hopping rate matches the central rate in a seven-ion crystal in the experiment. The main effect of the camera in the simulation is to smooth out the distribution of hopping outcome. However, as long as the hopping rate is not very high, the camera-derived hopping outcome is close in shape to the unfiltered one. (This is the reason why we only use a moderate hopping rate in the experiment for these plots). The camera mechanism produces non-nearest-neighbour hopping events at a site (for example, site 1), which corresponds to only 5 % of the total events at that site, substantially less than in the experiment. This suggests that either non-nearest-neighbour hopping exists in the

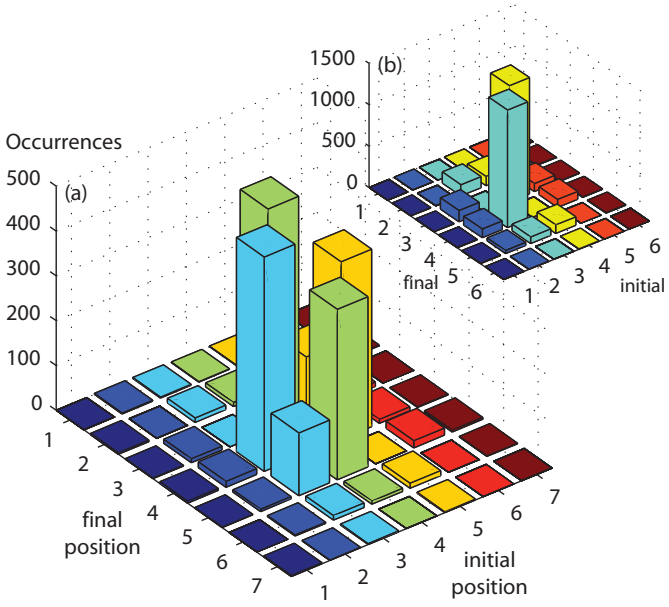

Figure 4.9: Distribution of hopping outcome as function of initial impurity position in a crystal of (a) seven ions and (b) six ions. Diagonal values are unobservable and set to zero. Trap frequencies for (a) are {443.5, 428.9, 126.6} kHz and laser parameters are a detuning of $\Delta/2\pi = -1.2$ MHz and scaled power of $p/p_0 = 27$. Figure (a) is based on a total of 40,000 images (4% indeterminate) and includes 2,166 relocation events. Omitted are 184 non-hopping events. Parameters for (b) are the same as those in Figs. 4.1(a). Figure (b) is based on a total of 30,000 images (2% indeterminate) and includes 3,797 relocation events. Omitted are 107 non-hopping events.

experiment, or a more sophisticated model of the camera's effect should be considered.

Focusing again on the experimental results, there is also a slight asymmetry for the case of seven ions in Fig. 4.9(a), indicating an increased tendency for the impurity to hop in the direction of site 1. In particular, there are 30% more hopping events from the central site 4 to site 3 than to site 5. Some care, however, is required in interpreting the raw event counts in Fig. 4.9. In general, they do not directly reflect the site-to-site hopping rates since the distribution is weighted by the probability for the impurity to be found at each site. For example, this can play a role in the asymmetry in Fig. 4.9(a) between events $3 \rightarrow 4$ and $5 \rightarrow 4$, where the initial position is different. A simple argument, as follows, relates the number of events to the hopping rate. The number of hopping events N_i from the i^{th} site – only the net rate summed over all outcomes is considered here for simplicity – is related to the average dwell time through the expression, $\langle \tau_i \rangle = \frac{1}{N_i} \sum_{j=1}^{N_i} \tau_{ij}$, where $\{\tau_{ij}\}$ is the sequence of dwell times at the i^{th} site acquired over the duration of a data set. From a purely experimental perspective, the expression can be rearranged to the form, $\langle \tau_i \rangle^{-1} = N_i / T_i$; that is, the hopping rate, characterized by the inverse average dwell time, is given by the measured number of hopping events divided by the measured total time, $T_i = \sum_{j=1}^{N_i} \tau_{ij}$, that the impurity dwells at the i^{th} site. The total dwell time, when appropriately normalized, gives the on-site probability, the probability for the impurity to be found at a given site.

From an interpretative perspective, it is more convenient to consider the expression $N_i = \langle \tau_i \rangle^{-1} \cdot T_i$; that is, the number of hopping events is the product of the hopping rate and, within a scale factor, the on-site probability. As will be shown, the strongest factor in determining the shape of the distributions of events in Fig. 4.9 turns out to be the spatial dependence of the hopping rate, rather than that of the on-site probability. Nevertheless, the on-site probability is discussed here in detail since it provides insight into the physical processes associated with the hopping dynamics. The data sets associated with Fig. 4.9 have been used to calculate the on-site probability, which is shown in Figs. 4.10(a) and (c). The on-site probability of the impurity ion is determined from the total time it resides at a site, normalized to the total time that a well-defined crystal is present during a data set. The plots in Fig. 4.10 are based on three or more successive data sets of either 11.4 or 22.8 min duration. Calculations based on the independent data sets are also included to show temporal fluctuations, which are most apparent at the edges of the crystal where the

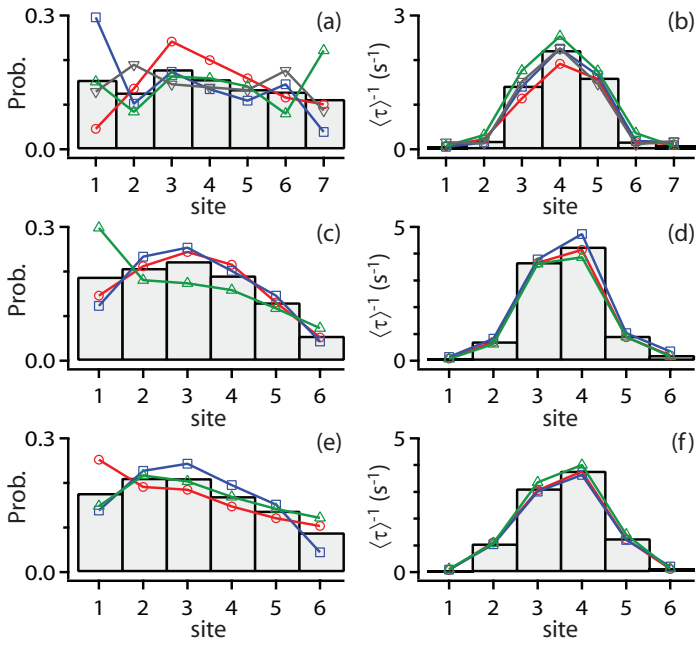

Figure 4.10: Left panels show the on-site probability for a $^{172}Yb^{+}$ impurity in a crystal of $^{171}Yb^{+}$ ions. Right panels show the inverse average dwell time of the impurity at each site. The on-site probability is the total time spent at a site, normalized to the total time that a well-defined crystal is present during a data set. The inverse average dwell time characterizes the hopping rate. Different open symbols represent successive data sets to show temporal variations. Solid bars are obtained from the combined data sets shown. Experimental parameters for the various panels are as follows. Figs. (a) and (b): The same data and parameters for a seven-ion crystal as in Fig. 4.9(a). Individual data sets shown are obtained from four consecutive sets of 10,000 images, covering 11.4 min each. Figs. (c) and (d): The same data and parameters for a six-ion crystal as in Fig. 4.9(b). Individual data sets shown are obtained from three consecutive sets of 10,000 images, covering 11.4 min each. Figs. (e) and (f): A six-ion crystal with a Doppler cooling beam 1.5(2) times larger in the axial direction than for (c) and (d), but with trap frequencies and central hopping rate closely matched. Trap frequencies are $\{442.0, 425.6, 141.1\}$ kHz, and laser parameters are $\Delta/2\pi = -0.9$ MHz and $p/p_0 = 18$. Individual data sets shown are obtained from three consecutive sets of 20,000 images, covering 22.8 min each. The combined data set of 60,000 images (4% indeterminate) includes 6,590 relocation events. Omitted from (f) are 222 non-hopping events.

hopping rate is low.

A trend of increased probability for the impurity ion to reside towards site 1 is clear for both seven and six ions (Figs. 4.10(a) and (c), respectively). This behaviour is consistent with the direction of the radiation-pressure force due to the Doppler-cooling laser (see Sec. 2.3 in Chp. 2). Since the laser beam is incident at 45° to the axial trap direction, there is a component of the force acting on the $^{171}Yb^{+}$ ions in the axial direction and pushing them in the direction of site 6. In turn, this will tend to cause the non-fluorescing $^{172}Yb^{+}$ impurity to diffuse via hopping in the upstream direction of the laser beam [61].

In Fig. 4.10, the on-site probability also appears to have a slight maximum, preferentially locating the impurity ion towards the centre of the crystal. Dipole forces are expected to be negligible and other spontaneous-scattering effects due to divergence of the cooling beam are unlikely to have a strong effect. One possible cause may be a differential cooling effect associated with the location of the non-fluorescing impurity and the non-negligible intensity profile of the cooling laser across the crystal. Specifically, an impurity defect near the centre of the crystal would reduce the average laser intensity impinging on the $^{171}Yb^{+}$ ions, and thereby reduce the average energy of the crystal and impurity. This lower average energy would, in turn, tend to reduce the hopping of the impurity away from the centre, and thus enhance the on-site probability there.

Even in the absence of an inhomogeneous intensity profile, the location of the non-fluorescing impurity may influence the mechanical response of the ion crystal to the cooling laser through the structure of the collective vibrational modes of the crystal [22, 62]. In addition, since the impurity ion relies on sympathetic cooling by the surrounding laser-cooled $^{171}Yb^{+}$ ions, the structure of the collective modes may also lead to a position dependence for the sympathetic cooling efficiency and average energy of the impurity. Overall, it is not immediately clear what the net trend on the on-site probability (and hopping rate) would be. Further possible effects on the average energy of the impurity ion will be discussed below.

Although the radiation pressure from the Doppler-cooling laser does appear to create an observable bias in the on-site probability of the impurity, the effect is perhaps not as strong as might be expected, for several reasons. First, due to coherent population trapping, the fluorescence scattering of the $^{171}Yb^{+}$ ions for the laser parameters of Figs. 4.9 and 4.10 is already substantially lower than for a saturated two-level atom. According

to Eqn. (2.13) in Chp. 2, the theoretical excited-state population for the central laser intensity in Figs. 4.10(a)–(d) is ~ 0.074 versus a value of 0.5 for a two-level atom in the high-saturation limit. Furthermore, the relatively high average energy of the crystal as a result of the compromised Doppler cooling will tend to soften the asymmetry in the on-site probability. Finally, the occasional loss of crystallization and re-crystallization can have an impact on the distribution of the impurity by "resetting" its position in the crystal. We find, albeit from low statistics, that the probability for loss of crystallization follows the on-site probability fairly well, which implies that the rate for the process is uncorrelated with the position of the impurity. Furthermore, the re-crystallization is not necessarily a fully randomizing process for the position of the impurity but at least does not appear to introduce a stronger bias in the position of the impurity than was already present before the loss of crystallization.

To assess further how the non-hopping events affect the on-site probability, we have considered a rate model including only the hopping processes. The matrix of rate coefficients, including inter-site asymmetries, is determined empirically from the distributions as in Fig. 4.9, corrected for the on-site probability. The solutions reproduce an asymmetric maximum in the on-site probability that roughly matches the data of Fig. 4.10. However, they consistently underestimate the probability at the edges of the crystal, with site 1 showing the largest discrepancies (by a factor of 1.6 and 2.7 for Figs. 4.10(a) and (c) respectively). Therefore, the non-hopping events do appear to flatten out the on-site probability distribution of the impurity ion to some extent.

Notwithstanding the spatial non-uniformity of the on-site probability, there is still a substantial probability for the impurity to be found at all sites within the crystal. Therefore, the narrow spatial distributions of hopping events shown in Fig. 4.9, are not dominated by the processes leading to the on-site probability of the impurity. In fact, correcting the plots in Fig. 4.9 for the on-site probability leads to distinct, but not drastic, changes in the distributions.

In Figs. 4.10(b) and (d), we also show the inverse average dwell time of the impurity ion as a function of crystal site, again calculated for the same data sets from Fig. 4.9. In general, the hopping rate decreases further away from the crystal centre – see also Fig. 4.5 – and has a relatively narrow maximum compared to that of the on-site probability. The hopping rate is nearly symmetric about the centre of the crystal except for a consistently

higher hopping rate on the right side (higher site number) in the plots. Although the effect is comparable to the overall fluctuations between successive data sets shown, each data set for six ions consistently shows the same bias (Fig. 4.10(d)). This is not the case for seven ions; however, the combined data still shows the same effect (Fig. 4.10(b)). The asymmetry in the hopping rate (for example, site 4 vs. site 3 in Fig. 4.10(d)), together with the general tendency for hopping towards the centre of the crystal as observed in Fig. 4.9, is qualitatively consistent with the spontaneous-scattering force driving the impurity defect during hopping towards site 1 (plot's left). In any case, the asymmetry is not a strong effect. The primary feature of the site-dependent hopping rate is the sharp peak at the centre of the crystal, which, along with its physical origin, is the most significant factor in determining the distribution of hopping events in Fig. 4.9. It is worth noting that a peak in the hopping rate at the centre of the crystal is not inconsistent with a preference for the impurity ion to be located there since the maximum in the on-site probability is determined by an asymmetry, or irreversibility, in the hopping rate of the impurity towards and away from the centre of the crystal.

As noted in Sec. 3.2 in Chp. 3, the size of the Doppler cooling beam is comparable to the axial extent of a six- or seven-ion crystal (for technical reasons). We have already noted a possible effect of the intensity profile on the on-site probability, and this raises the question of an effect on the spatial profile of the hopping rate. For example, it is conceivable that the higher laser intensity at the centre of the crystal could result in a higher average energy for the central sites. This would enhance the hopping rate compared to the edges of the crystal. As a follow-up experiment, we have tested the effect of the beam size by increasing it by a factor of 1.5(2) to an intensity FWHM of $\sim$70 μm along the axial extent of the crystal. The laser power was increased within technical limits to reach an intensity at the centre of the beam of $I/I_0 = 18$, or equivalently a power of $p/p_0 = 18$, which is somewhat lower than the value of 28 used for the data with the smaller beam in Figs. 4.9 and 4.10. To compensate for this difference, we tuned the laser closer to resonance ($\Delta/2\pi = -0.9$ MHz) in order to obtain approximately the same hopping rate at the centre of a six-ion crystal as in Fig. 4.10(d). The on-site probability for the larger beam size, shown in Fig. 4.10(e), is slightly more uniform than the distribution for the smaller beam size in Fig. 4.10(c). There is more of a difference between the two cases if the rate model for only hopping processes is considered to eliminate the effect of the non-hopping events. For the larger beam, the

on-site probability from the steady-state solution has a more obviously flatter distribution; however, this is primarily due to a difference in behaviour at a single location, site 1.

More importantly, a comparison of Fig. 4.10(f) to Fig. 4.10(d) shows that the spatial profile of the hopping rate is only slightly broader for the case of the larger beam size. The hopping rates for sites 2 and 5, after normalization to the value in the centre of the crystal, show a factor of 1.5–2 increase; however, this represents only a $\sim$12% increase compared to the peak value of the hopping rate at the centre of the crystal. Although not shown here, the spatial distribution of hopping outcome for the larger beam is qualitatively the same as already shown in Fig. 4.9(b), with a small enhancement in the low lying counts surrounding the dominant central two sites. Therefore, within the limitations of our test, the spatial dependence of the hopping behaviour does not appear to be a strong function of the profile of the laser beam for the size used here. The remainder of the data shown in the following sections continues to use the original beam size with a 50-μm FWHM.

4.4 Hopping rate as a function of laser parameters

We now study the onset of hopping with laser and trapping parameters and demonstrate that it can be controlled. The onset is first studied as a function of laser detuning and power for six ions in a trap with frequencies {443.1, 426.9, 138.8} kHz, corresponding to an α parameter just below the onset of the zigzag transition. The inverse average dwell time, obtained from 3,000 images, is plotted as a function of laser detuning and power in Fig. 4.11(a) and (b) respectively. Only half the crystal sites are shown since the behaviour is approximately symmetric. The laser power values plotted in Fig. 4.11(b) have been corrected for drifts occurring during the data collection.

As before, the hopping rate decreases away from the centre of the crystal. The onset of hopping requires high laser power and a detuning close to resonance. For the case of the power dependence, the onset of hopping occurs at $p/p_0 \sim 25$. This is well into the regime of coherent population trapping for $^{171}Yb^{+}$ and corresponds to a central intensity of the cooling laser a factor of $\sim$3 above the value required for maximum fluorescence. At this intensity, the effective linewidth is strongly broadened by a theoretically expected factor $\gtrsim 3.5$ from its low intensity value. Due to the broad linewidth and close detuning, this is a regime of laser cooling with energies well above the optimal Doppler limit and, as such,

is indicative of the height of the transverse Coulomb barrier that inhibits the swapping of ions during a hopping event. Modeling the laser cooling for this range of laser parameters requires care [20, 63] and should also include the effect of the laser beam profile across the ion crystal [64] and modifications to the collective behaviour of the ion crystal near the zigzag transition [15]. In addition, the average energy of the non-fluorescing impurity requires a consideration of the sympathetic cooling process, which may result in a different (and location-dependent) average energy for the $^{172}Yb^{+}$ impurity than for the laser-cooled $^{171}Yb^{+}$ ions.

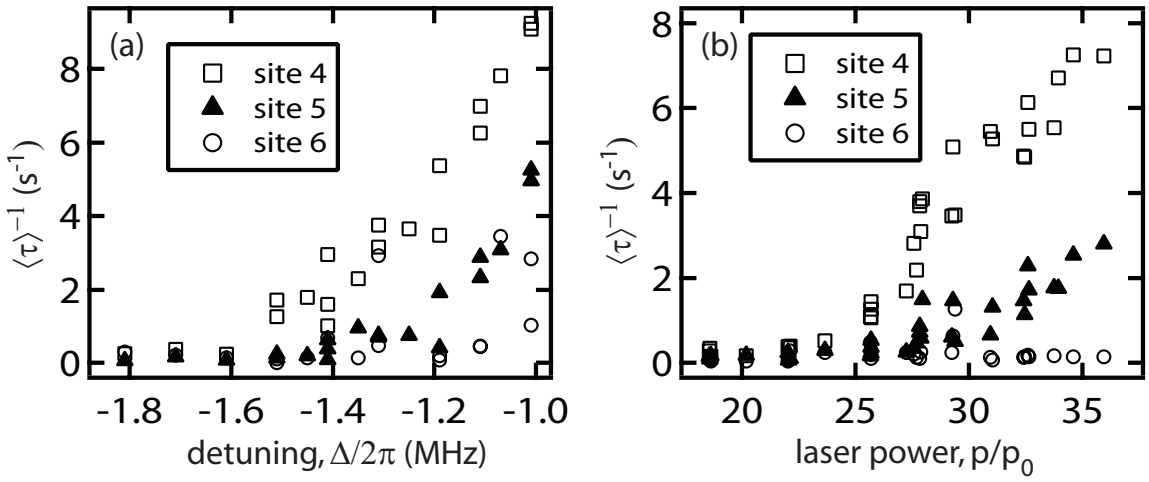

Figure 4.11: Impurity hopping rate in a six-ion crystal as a function of (a) laser detuning and (b) laser power. The rate, characterized by the inverse average dwell time, is obtained from 3000 images and plotted for sites 4, 5 and 6 (see legend); behaviour at other sites is nearly symmetric about the centre of the crystal. Statistics are marginal for the low hopping rates. Trap frequencies for both (a) and (b) are {443.1, 426.9, 138.8} kHz. For (a), the laser power is fixed at $p/p_0 = 30$ in terms of saturation value p_0 (see text). For (b), the laser detuning is fixed at $\Delta/2\pi = -1.2$ MHz.

To obtain a qualitative idea of the average energy imparted to the ions, we have studied a single $^{171}Yb^{+}$ ion for the same laser parameters. From the gaussian profile of the ion's time-integrated position in the harmonic trap, we can estimate its average energy. To within the limits of the technique, we find that the average scaled axial energy is $\langle E_z\rangle/\hbar\omega_z \gtrsim 10^4$,

well above the Doppler cooling limit of $\gamma/2\omega_z \sim 10^2$. Furthermore, the transverse energy $\langle E_r \rangle$ is a factor of $\sim$4 larger than the axial energy, which can be expected qualitatively from the details of the laser cooling [45, 20, 46]. For comparison, an upper limit on the transverse energy barrier to hopping at the centre of the ion crystal, assuming $\omega_{x,y}$ is somewhat larger than ω_z, is provided by the Coulomb interaction energy $E_c \approx q^2/4\pi\varepsilon_0 a_0$. Here, a_0 sets the scale for ion-ion separation in the transverse $y-$direction according to $a_0^3 = q^2/(4\pi\varepsilon_0 m\omega_y^2)$ [13]. For $\omega_y/2\pi \sim 430$ kHz, one obtains $a_0 \sim 5$ μm and $E_c/\hbar\omega_y \sim 10^5$ yielding $E_c/\langle E_r \rangle \sim 10$. This model of the energy barrier for hopping can be further improved, for example through the inclusion of the initial axial ion spacing, which is smallest at the centre of the crystal and therefore is expected to give the lowest barrier there. As a final note, assuming that the measurements of average energies for single ions can be taken to apply to multi-ion crystals, the associated large amplitudes of motion of the ion crystal imply that the system will be outside the linear regime of small collective oscillations, and nonlinear behaviour such as coupling between collective modes can be expected.

4.5 Hopping rate as a function of trap anisotropy

In our final experiment, the effect of the confining potential on hopping behaviour is considered. In particular, an enhancement of the hopping is observed to occur near the onset of the structural phase transition to the zigzag configuration. Therefore, we have first characterized the onset of the zigzag transition for pure $^{171}Yb^+$ crystals as a function of the end-cap voltage, which affects the anisotropy of the confining potential.

To characterize the zigzag transition, we set the laser parameters to achieve good Doppler cooling. For each value of the end-cap voltages, a short sequence of images is taken and the peak-to-peak transverse displacement of the zigzag configuration is obtained by averaging fits of 30-100 images. The largest amplitude displacement is found to occur at the centre of the crystal as expected. In Fig. 4.12(a), the transition behaviour for crystals of six and seven ions is plotted with respect to the α parameter, the values of which are calculated from measurements of the secular trap frequencies. The spatial scale of the images used to infer the zigzag displacements is calibrated by making a comparison of the axial ion spacing to numerical theory across a range of end-cap voltages.

For the measurements of the zigzag transition, the laser cooling needs to be optimized

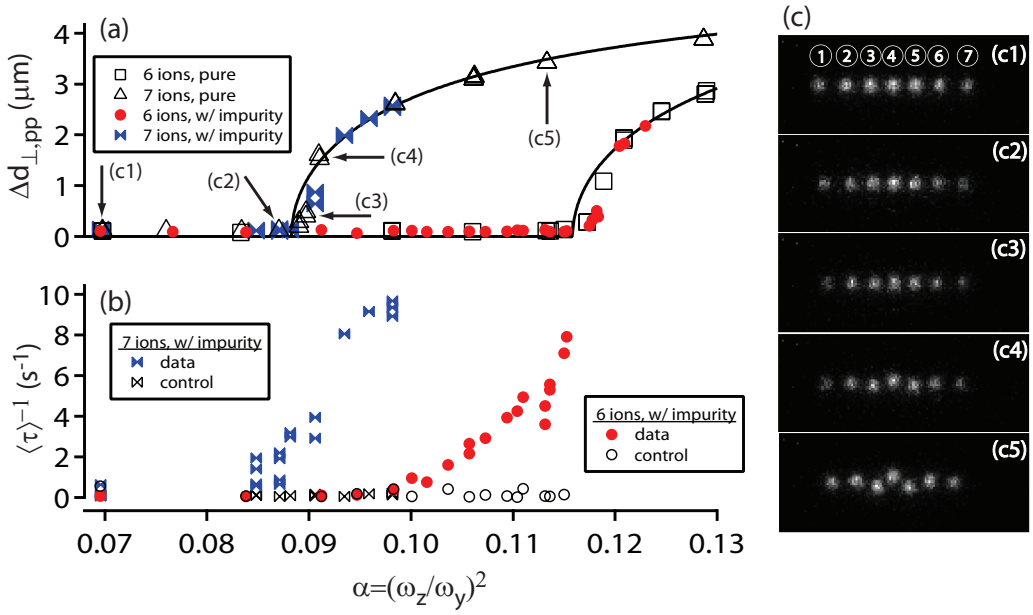

Figure 4.12: Laser-induced impurity hopping rate as a function of trap anisotropy near the structural zigzag transition. (a) Location of the zigzag transition for six- and seven-ion crystals. Open symbols show the peak-to-peak displacement of the zigzag configuration, transverse to the imaging axis, in a pure $^{171}Yb^{+}$ crystal as a function of anisotropy-related parameter $\alpha = (\omega_z/\omega_y)^2$. The anisotropy, which decreases from left to right, is modified using the trap end-cap voltages. Solid symbols show similar for an ion crystal with a single impurity ion, offset from the centre of the crystal by 1.5 sites for 6 ions and 1 site for 7 ions. Lines are obtained from numerical minimization of energy for a pure crystal and include a scale factor to account for an oblique viewing axis. The binned pixel size in images corresponds to 0.69 μm. Laser parameters for the data sets are as follows. Open squares and open triangles: $\Delta/2\pi = -8.1$ MHz, $p/p_0 = 3.5$ near zigzag transition, $p/p_0 = 8.2$ otherwise; solid circles: $\Delta/2\pi = -8.2$ MHz, $p/p_0 = 3.8$ near zigzag transition, $p/p_0 = 9.0$ otherwise; solid bow-ties: $\Delta/2\pi = -8.2$ MHz, $p/p_0 = 3.2$. (b) Inverse average dwell time versus α for an impurity at central site 4 in a six-ion crystal and at middle site 4 in a seven-ion crystal. Data (solid) and control (open) points correspond to laser parameters leading to high and low kinetic energies respectively. Laser parameters are as follows. Solid circles: $\Delta/2\pi = -1.2$ MHz, $p/p_0 = 27$; open circles: $\Delta/2\pi = -8.2$ MHz, $p/p_0 = 9.0$; solid bow-ties: $\Delta/2\pi = -1.2$ MHz, $p/p_0 = 27$; open bow-ties: $\Delta/2\pi = -8.2$ MHz, $p/p_0 = 3.2$. (c1)–(c5) Examples of crystal structure at different α as indicated in (a).

to limit thermally induced switching between opposing zigzag configurations, particularly near the critical anisotropy. Near this anisotropy where the frequency of the lowest transverse collective mode goes to zero [15], the local transverse potential at the centre of the crystal is very soft and the barrier to zigzag switching is low. Notwithstanding reasonably optimized Doppler cooling, significant switching is still observed in image sequences close to the onset of the transition, as evidenced by excess image-to-image fluctuations in the transverse zigzag displacement. Although this affects the calculation of the average displacement, we ignore the effect since the location of the transition's onset is already sufficiently well defined for our hopping studies.

The theoretical prediction for the transverse zigzag displacement, obtained from numerical energy minimization described in Sec. 2.2, matches the data well (Fig. 4.12(a)) except for a consistent discrepancy near the onset of the transition. This bias may be due to the effect of thermal switching on the measurement, as mentioned above. An overall scale factor is included in the theory to account for an oblique viewing angle, and corresponds to a 45° tilt of the trap's weaker transverse axis (y-axis) with respect to the horizontal plane. Good agreement between theory and experiment for six and seven ions continues over a larger range of α than shown in Fig. 4.12(a). We have also verified the behaviour of the zigzag transition against theory for crystals with five ions with similar success.

Following the calibration of the zigzag transition in pure crystals, a study of hopping as a function of trap anisotropy has been performed on six- and seven-ion crystals containing a single impurity defect. Suitable values of the laser power ($p/p_0 = 27$) and detuning ($\Delta/2\pi = -1.2$ MHz) are chosen to activate the hopping, according to studies as in Fig. 4.11. The primary aim is to ensure that the hopping rate near the zigzag transition is rapid but does not overwhelm the CCD frame rate. The hopping is then measured over a range of end-cap voltages. For each end-cap value, small adjustments are first made to the dc voltages applied to the trap rods to minimize the effect of micro-motion on the laser cooling [65]. In Fig. 4.12(b), the inverse average dwell time for a single site (site 4) in the centre of the crystal is plotted with respect to the trap α parameter. Control data taken at a detuning of $\Delta/2\pi = -8.2$ MHz and a moderate laser power of $p/p_0 = 9.0$ for six ions or $p/p_0 = 3.2$ for seven ions is also included. This control data, in conjunction with some additional points, is simultaneously used to determine the peak-to-peak zigzag displacement with the location of the impurity selected to be near the centre of the crystal (Fig. 4.12(a)).

Simulations show the effect of the $^{172}Yb^{+}$ impurity on the critical anisotropy is minor, as observed.

In Fig. 4.12(b), the onset of hopping for seven ions occurs before that for six, which is natural to attribute to the relative location of the two zigzag transitions. As the zigzag transition is approached and the frequency of the lowest transverse collective mode drops to zero, thermal fluctuations of the crystal will allow for substantial transverse excursions at its central sites, in particular when large average energies are induced by compromised laser cooling. As mentioned above, the associated large transverse amplitudes of motion at the centre of the crystal will give rise to nonlinear behaviour, including strong coupling between the axial and transverse collective motions as the zigzag transition is approached. This mechanism together with the lower barrier at the centre of the ion crystal presumably enables, or at least is a significant factor in enabling, the rapid hopping at the central sites as seen in Fig. 4.9. Also, since we are modifying α by changing the end-cap voltages, it should be mentioned that there is also an accompanying effect on the energy barrier, which decreases with increasing α due to the reduction in the axial ion-spacing.

The situation is further complicated because the critical anisotropy for the structural phase transition is also predicted to depend on temperature [26]. According to the calculations in Ref. [26], the transition to the zigzag phase for a 10-ion crystal shifts from $\alpha = 0.0475$ to 0.0486 (a 2% change) when the temperature is raised from 0 to 10 mK. In other words, the transition is suppressed at finite temperature. The shift in the critical value of $\alpha^{-1/2} = \omega_y/\omega_z$ is roughly linear in temperature up to 10 mK (see Fig. 2 in Ref. [26]). For the sake of argument, if we extrapolate this linear dependence to a temperature typical in our hopping experiments (~ 40 mK), the critical value of α would shift by about $\sim 10\%$ from the zero-temperature value. The actual change may be even larger due to deviation from linearity in $\alpha^{-1/2}$. . If roughly the same 10% fractional change applies to our cases of seven- and six-ion crystals, we can say that the observed onset of hopping in a sense occurs even earlier relative to the onset of the zigzag transition than one might assume from Fig. 4.12. (The ordering of the transitions for seven and six ions would still remain the same.)

Even though not our main purpose, it is interesting to consider briefly if our datasets of ion crystals show any evidence for the suppression of the zigzag transition at higher average kinetic energies (higher temperature). In Fig. 4.13, we compare the images of a seven-ion

crystal under different laser cooling conditions for the same anisotropy parameter, $\alpha = 0.0982$. This value of α is higher than the critical value of 0.0883 calculated in Chp. 2 in the absence of thermal fluctuations. We show in Fig. 4.13(a1) a typical image of the ion crystal at a high average energy where the hopping is already turned on. From the image, it seems that the crystal is in a linear configuration. At low average energy, that is, for good Doppler cooling, the crystal is clearly observed to be in one of the two zigzag configurations (Fig. 4.13(a2) and (a3)). In transitioning between these two cases by adjusting the laser cooling, we observe as we increase the laser power that the transverse switching between the two symmetric zigzag configurations is the first dynamics to be activated. Then, at yet higher powers, the hopping between sites is activated. Perhaps the most critical question is: can a time-averaged image (sequence) of a crystal that is rapidly switching between 'zig' and 'zag' configurations (and undergoing hopping) be reliably distinguished from an actual linear configuration?

To avoid effects due to fluctuations in a single image, we show the overlap of a series of images of the crystal at high average kinetic energy (a4) and at low average kinetic energy (a5), respectively. The two cases do not show a dramatic difference. In Fig. 4.13(b), a normalized horizontal cross section of the fluorescence level for the central ion in (a4) and (a5) is shown. The profile at low kinetic energy (blue), which is simply the sum of the two zigzag configurations at low kinetic energy (the green-dotted line and the green-dashed line), has two slightly resolved peaks. The higher kinetic energy case (red) shows a fluorescence profile with a single peak at the centre, but the overall width of the profile is comparable to that at low kinetic energy. Given the many systematics involved in the comparison, there is no obvious and immediate evidence of a suppressed transition from these images.

4.6 Discussion

It has been shown that site-to-site hopping can be induced in a linear ion crystal by controlling the parameters of Doppler laser-cooling, which affects the average energy of the crystal. The spatial distribution and event-by-event outcome of the hopping of a single, distinguishable impurity ion have been determined, and the hopping is observed to be concentrated towards the centre of the crystal for six and seven ions. The hopping rate is also

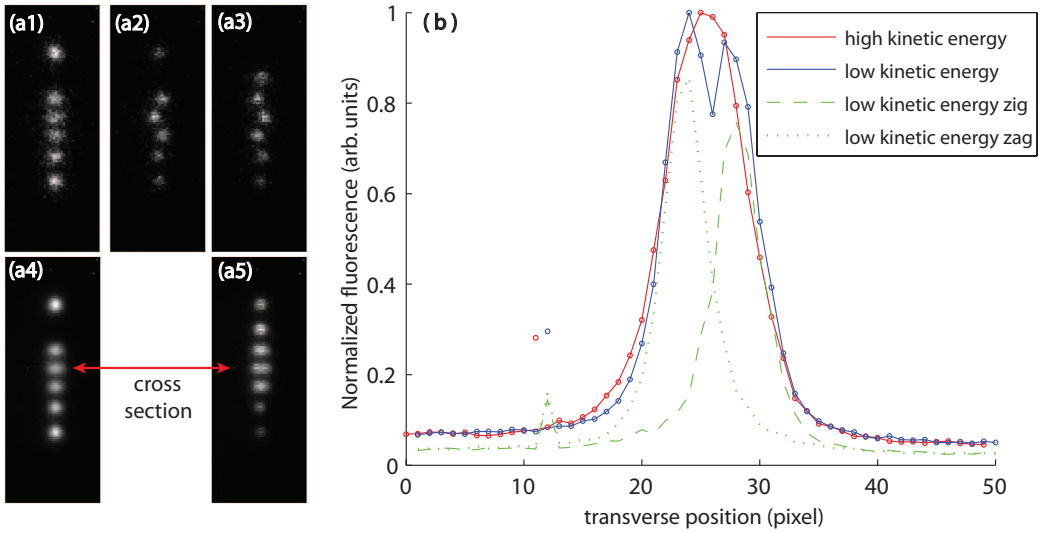

Figure 4.13: Zigzag configuration at different average kinetic energies. (a1) Typical image of the crystal at high kinetic energy corresponding to laser cooling parameters $\Delta/2\pi = -1.2$ MHz, $p/p_0 = 27$. (a2)&(a3) The two zigzag configurations at low kinetic energy corresponding to laser cooling parameters $\Delta/2\pi = -8.2$ MHz, $p/p_0 = 3.2$. (a4) Overlap of 50 images of the crystal with the same cooling parameters as in (a1). (a5) Overlap of 50 images of the crystal with the same cooling parameters as in (a2)&(a3), in which half of the images shows the zig phase and half shows the zag phase. (b) Cross section of the fluorescence profile as indicated in (a4)&(a5). The fluorescence levels are normalized to the peak value for the central ion. The green-dashed line and green-dotted line are obtained from the two sets of 25-images corresponding to the two zigzag configurations. For all the data shown, anisotropy parameter are set to $\alpha = 0.0982$.

found to be enhanced as the ion crystal is brought close to the zigzag transition, which depends on the number of ions in the crystal. That the hopping tends to be concentrated near the centre of the crystal and is enhanced near the zigzag transition are consistent with an intrinsic cause for the behaviour related to the structure and dynamics of the crystal near the zigzag transition. The softening of the zigzag collective mode as the transition is approached can lead to large thermally activated transverse amplitudes and non-linear dynamics at the centre of the crystal. As well, the higher linear density of ions at the centre of the crystal makes the barrier to hopping lowest there.

There are, however, several complications in the experiment that may influence this conclusion. The laser beam used in this experiment has a non-negligible intensity profile across the crystal and could lead to a position-dependent average energy. The highest laser intensity is at the centre of the crystal and could contribute to a higher hopping rate there. A test with a larger beam size in Sec. 4.3, however, appears to indicate that the spatial dependence of the hopping rate is not strongly sensitive to the size of the beam for the value used in these experiments. It is also noted here that the hopping behaviour for six ions as a function of trap asymmetry was similarly found to be insensitive to the change in beam size.

As alluded to in Secs. 4.3 and 4.4, the impurity may also play an active role in influencing the rate of hopping and its spatial dependence. First, the non-fluorescing impurity ion may modify the effect of the cooling laser on the crystal depending on the position of the impurity, for example in conjunction with the profile of the laser intensity. We have observed behaviour, albeit at a mild level, in the on-site probability that may be related to such an effect (Sec. 4.3). As long as the laser beam is not too small, one might not expect the hopping rate to be most strongly affected in this way for six and seven ions, where a single impurity with nearly identical mass should have a small fractional effect on the response of the crystal to the cooling laser. Second, the impurity ion may also have a different average energy than the rest of the crystal because it depends on the indirect sympathetic cooling from the surrounding $^{171}Yb^{+}$ ions. The efficiency of the sympathetic cooling can have a position dependence, due to structure of the collective modes of the crystal, and may contribute to the spatial dependence of the hopping rate. It is not clear how significant such an effect would be, summed over all the thermally excited modes of motion of the crystal. In any case, the hopping events observed are ultimately at least a two-body process involving

not only the impurity but at least one of the $^{171}Yb^{+}$ ions.

Molecular dynamics simulations are probably the easiest way to model the hopping, including the laser- and trap-induced onset and the apparent differences in behaviour between six and seven ions. Such simulations are also convenient to test for the effect of the camera frame rate, the influence of the non-fluorescing impurity on the spatial dependence of hopping, effects due to the laser beam size, and the possibility of laser-cooling effects and micro-motion heating [6] that may have a dependence on the end-cap voltage. As a preliminary step in this direction, we have performed molecular dynamics simulations of ion strings confined in an ideal harmonic confining potential and at constant energy, that is, without direct inclusion of the rf potential or of laser cooling per se. The details will be discussed in the next chapter, however, we note here, that simulations in which the ions are initially perturbed significantly from equilibrium in fact already show hopping behaviour that qualitatively matches our experimental observations, including a hopping intensity concentrated at the centre of the crystal. This is suggestive that the cause for the spatial distribution of hopping is intrinsic to the crystal structure and dynamics near the zigzag transition.

Chapter 5

Numerical Simulation of Hopping

In this chapter, we describe molecular-dynamics simulations of hopping behaviour in ion crystals. The simulations are a simple and preliminary version in which we ignore many of the technical complications in the experiment and let the crystal of ions evolve according to Newtonian dynamics with constant energy. The result reproduces several of the important features of the hopping behaviour observed in the experiment (Chp. 4), including the concentration of hopping at the centre of the crystal.

5.1 Molecular dynamics simulation

In the previous chapter, we did not include a quantitative theoretical model for the hopping behaviour of the impurity ion. In particular, we did not attempt with theory to reproduce the strong dependence of the hopping rate on the power and detuning of the Doppler-cooling laser, or on the anisotropy of the trap potential. It would have been intuitive, and our preference, to convert the laser-parameter plots to plots in terms of average kinetic energy of the crystal; however, as discussed in Chp. 4, the laser-cooling model becomes non-trivial for the range of laser parameters considered in the experiment. There are also technical factors in our experiment that could influence the final behaviour of the ion crystal. First, the impurity has a different mass from the rest of the ions. Second, residual micro-motion arising from the rf potential is a source of heating and could enhance hopping. Third, the non-fluorescing impurity complicates the situation in several ways. The cooling laser exerts light pressure on the $^{171}Yb^{+}$ ions in the downstream direction and, in effect, pushes the

impurity upstream. The cooling rate for the crystal may depend on the location of the dark impurity, and the energy of the impurity ion itself depends on the details of sympathetic cooling.

All put together, it seems simplest to resort to numerical simulation to compare the experiment to theory. Molecular dynamics (MD) simulation, in which the dynamics of the individual ions are integrated in time is a well-established and ongoing research area in the ion-trap literature. Molecular dynamics simulations have been used to study equilibrium structures [9], the order-disorder transition [16, 18], the closely related issue of micromotion heating [18, 66] and laser cooling [67, 68]. The listed references are only a small sample of the literature using MD simulations for studying trapped ions and are usually applied to systems with a large number of ions. Even six ions, though, are already complicated enough!

The effect of the various complications in the experiment can be conveniently assessed with MD simulation, in which different ingredients of the complex situation can be controlled independently. For example, one can assign the same mass to all the ions including the impurity while keeping the impurity non-fluorescing, or making them all fluorescing while keeping the difference in mass. This allows us to investigate different attributes one by one, while in reality they are not separable.

Having said all this, we present in this chapter the simplest possible MD simulation as a first step towards these more complicated investigations. We in fact find that a simple solution that ignores most complications of the experiment already shows qualitatively most of the behaviour we observe in the experiment.

5.2 Implementation of the simulation

Before presenting the details of the MD simulation and its implementation, we first discuss three simplifications made to the model of N ions confined in a linear rf Paul trap, as follows:

As discussed in Chp. 2, the nominally harmonic potential in the transverse direction is generated by an oscillating rf electric field. In this initial version of MD simulations, we do not simulate the rf potential directly but consider only the effective time-averaged pseudopotential. As a result, there is no micro-motion involved. The ion motion is also limited to

two-dimensions, where we assume ideal harmonic potentials in both axial (z) and transverse (y) directions to confine the ions. As in the experimental setup, the axial confinement is weaker than the transverse one. Ignoring one transverse axis is a reasonable simplification in first order since the zigzag transition is determined by the weakest transverse direction only.

The mechanism of laser cooling and heating is also not included in these initial simulations. In the presence of the Doppler-cooling laser, the fluorescing ions constantly scatter photons, leading to laser cooling and recoil heating. The balance between these and other heating processes on average sets the kinetic energy of the ions. The inclusion of the Doppler-cooling laser in the model is a significant complication because one has to account for the stochastic behaviour of the photon scattering. Instead, a constant-energy approach is adopted in our MD simulations, where we give some initial displacement to the ions to raise their energy above equilibrium and let them evolve according to Newtonian dynamics. We find that constant energy dynamics is actually a reasonable, preliminary approach since at high excitation energies, the highly nonlinear behaviour of several trapped ions randomizes their motion and destroys, for example, the memory of initial conditions. Finally, it should be noted that, in the absence of a laser interaction in the model, the radiation pressure on the ions is automatically neglected, the distinction between the non-fluorescing impurity and the rest of the ions is neglected, and effects due to the laser profile are also eliminated.

As our last simplification to the simulation model, we assume that all the ions have the same mass. This of course ignores the small but non-zero mass difference between the $^{172}Yb^{+}$ impurity and the $^{171}Yb^{+}$ ions in the crystal.

In a simulation with the above simplifications, the evolution solely depends on the number of ions in the crystal, the shape (asymmetry) of the confining potential, and the size of the excitation energy. In some ways this simple situation is very convenient: Any hopping behaviors we observe in the simulation must be intrinsic to the system, and not due to technical experimental details.

The model: The model we implement is a set of coupled Newton's-Law equations for N ions confined in a two-dimensional harmonic trap and interacting via pair-wise Coulomb forces. The dimensionless differential equations of motion for the rescaled positions $\{\mathbf{r}_\mathbf{i}'\}$

of the ions are as follows:

$$\frac{d^2\mathbf{r}_i{}'}{dt'^2} + y_i'\hat{\mathbf{y}} + \alpha z_i'\hat{\mathbf{z}} = \sum_{j=1,j\neq i}^{N} \frac{\mathbf{r}_i{}' - \mathbf{r}_j{}'}{|\mathbf{r}_i{}' - \mathbf{r}_j{}'|^3}. \tag{5.1}$$

Here, we have used the characteristic length $a_0 = (q^2/4\pi\varepsilon_0 m\omega_y^2)^{1/3}$ from Sec. 2.2 in Chp. 2 to rescale the positions so that $\mathbf{r}_\mathbf{i}' = \mathbf{r}_\mathbf{i}/a_0 = (y,z)/a_0$. Time is rescaled by ω_y^{-1} to the dimensionless parameter $t' = \omega_y t$. In this system of length and time scales, the energy of the system is expressed in units of $E_0 = q^2/(4\pi\varepsilon_0 a_0) = (m\omega_y^2)^{\frac{1}{3}}(q^2/4\pi\varepsilon_0)^{\frac{2}{3}}$ (see Sec. 2.2). If we use the mass of the $^{171}Yb^+$ ion, then the energy scale is $E_0 \approx 1.69\times 10^5\hbar\omega_y$. Finally, note that the only free parameter in the rescaled Eqn. (5.1) is the trap anisotropy $\alpha = (\omega_z/\omega_y)^2$.

Implementation: We use MATLAB software to perform the molecular dynamics simulation. The code is based on software for modeling a gas of particles with pair-wise interactions, originally written by Bill Magro in FORTRAN90 and rewritten in MATLAB by John Burkardt [69]. Modifications (including corrections) were made to adapt the code to our case of N ions interacting through Coulomb repulsion. The program is very simple and integrates the coupled Newton's equations for N ions using the velocity-Verlet algorithm.

Variable input parameters for the program include the number of ions N, the trap anisotropy parameter α, and the initial conditions that we use to introduce a displacement from equilibrium in either position or velocity. The displacements do not include a centre-of-mass (COM) component since the COM motion of the ion crystal is completely separable from the other internal dynamics in an ideal harmonic trap and so has no effect on the hopping for any amplitude. The initial displacement corresponds to excitation energy ΔE measured relative to equilibrium value. As will be shown, the details of the initial conditions do not matter except for the excitation energy. Nevertheless, we prefer to excite the ion crystal with the transverse zigzag mode because it matches most closely the steady-state probability distribution for the positions of the ions in the simulation. This is not surprising since the soft transverse zigzag mode has the lowest frequency by far near the onset of the zigzag phase transition and, all things being equal, will have a large amplitude of excitation.

Although performing MD simulations for different numbers of ions and under different conditions is straightforward in principle, the length of computation time required is somewhat prohibitive. We therefore limit the discussion here to the case of a crystal with

six ions. We also focus on a single trap with anisotropy parameter $\alpha = 0.1152$, which is just below the critical value $\alpha_{\text{crit}} = 0.1157$ predicted by theory. For convenience of all discussions below, we consider the simulation results in terms of an actual trap with secular frequencies $\omega_y/2\pi = 426.26$ kHz and $\omega_z/2\pi = \sqrt{0.1152} \times 426.26$ kHz $= 144.7$ kHz in the transverse and axial direction respectively. These frequencies are close to typical values that we use in the experiment.

For our simulation model, the size of the time step is roughly determined by the highest-frequency collective mode of the ion crystal being considered. As already pointed out in Chp. 2, the mode with the highest frequency in the transverse direction is the COM mode with a value of $\omega_y^{(N)} = \omega_y$. At or near the critical asymmetry α_{crit}, however, the *axial* zigzag mode is the mode with overall highest frequency and has a value of roughly $\sqrt{2}\omega_y$ for six ions. We choose a simulation step-size that divides the transverse trap period, $T_y = 2\pi/\omega_y$, into 1000 steps. For $\omega_y/2\pi = 426.26$ kHz, the actual time for one step is $(1000 \times \omega_y/2\pi)^{-1} = 2.346$ ns. We have checked that a decrease in time step by a factor of 2 does not significantly affect the hopping statistics, although the trajectories diverge after a relative short simulation time for the excitation energies studied. This appears to be a standard circumstance that arises in molecular dynamics simulations due to system nonlinearity [70, 71]; more details will be provided at the end of this chapter.

The non-parallelized MD simulation is performed on a desktop computer with a 2.50-GHz processor. For the time step noted above, a computation time of about 40 hrs is required to simulate 1 sec of dynamics. Lengthy computation times are a standard issue with MD simulations where there is a wide range of time scales. While the collective modes compel us to integrate the equations with a time step on the order of nanoseconds, a study of the dynamics of interest, namely hopping, requires simulations on the order of seconds or more.

A simulated time of 1 sec is still well short of the typical data collection time of 10 min that was used in the experiment to acquire sufficient hopping statistics. To obtain reasonable hopping statistics from the MD simulations, we have raised the excitation energy to drive faster hopping rates, which are well outside the range of those measured in the experiment (see below). In the future, we will consider the use of parallel computing facilities such as WestGrid to implement simulations that should more closely approximate the conditions of the experiments.

After every 1800 time steps in a 1-second simulation, the MD simulation saves the two-dimensional positions for all six ions. This allows tracking of the ion trajectories, from which the statistics of hopping can be extracted. In contrast to the experiment, the ions in the simulation are distinguishable so we can monitor the behaviour for each by following its trajectory. The simulation also occasionally outputs the kinetic and potential energy of the system. The constancy of the total energy provides a direct test of the integration accuracy. Although the total energy shows a small fluctuation about its initial value due to the finite step size, the fractional error is always at the same level of $\sim 10^{-7}$ and is not accumulated through the simulation.

5.3 Simulation results

5.3.1 Simulation tests and basic hopping behaviour

As noted above, our simulations focus on a six-ion crystal in a trap potential with an anisotropy parameter α of 0.1152, just below the critical value of 0.1157. The hopping can be activated easily in the experiment with such a potential, and we seek to see if this is the case for the simulations.

Before attempting to simulate hopping, we have first performed several simple tests to validate our simulation software. In particular, we have given (somewhat) small displacements to the ions ($\Delta E = 0.0177 E_0$, or about 20% of the hopping barrier (3 % per ion) mentioned in Sec. 2.2.3) to activate various collective modes of vibration of the crystal and compared the frequencies of oscillation to theoretical expectations. Selecting excitation of a given mode of course requires the correct symmetry for the initial displacements and we make use of the table of eigenmodes published in Ref. [35]. For example, in Fig. 5.1, the transverse positions of the ions are shown as a function of time after an initial excitation of the transverse "bow-tie" mode (see also the "streak-camera" image in Fig. 5.1(b)). As expected, each of the ions undergoes simple harmonic motion in the transverse direction with the same oscillation frequency and with a fixed relative amplitude whose value depends on the eigenmode. The mode frequency obtained from a fit to the oscillations is $0.9406\omega_y$, consistent with the value of $0.9406\omega_y$ obtained from the theory of small oscillations in Sec. 2.2. We also show in Fig. 5.2 an excitation of the *axial* bow-tie mode for six ions.

The mode frequency obtained from a fit to the oscillations is $0.5881\omega_y$, again matching the theoretical prediction of $0.5880\omega_y$ pretty well.

After the tests in the small oscillation limit, we move on to give the crystal a larger initial displacement from equilibrium to see if hopping can be induced in the MD simulations. As we increase the initial displacement, the resulting amplitudes of oscillatory motion increase and eventually the oscillations become highly nonlinear and complex. However, each ion still moves around its equilibrium position most of the time and hopping is absent or very rare. At still larger displacements, site-to-site hopping is observed in the simulations. In Fig. 5.3, we show the axial motion of the six-ion crystal when the simulation is started with a large transverse zigzag displacement, corresponding to an excitation energy of $\Delta E = 0.2870E_0$ above the equilibrium value of $7.9956E_0$. The trajectories of the ions are color coded according to the initial site to allow each ion to be followed in time. Substantial site-to-site hopping occurs in the four interior crystal sites, among which the centre two sites are most active. Moreover, if we focus on any one ion in this interior region, for example the one indicated by the red line, we see that it visits all the interior sites over the course of the simulation. This behaviour can be compared with that of the outer two ions, which oscillate but never leave their original site through a hopping event.

The general trend of faster hopping near the centre of the crystal is the same as what we see in the experiment in Chp. 4, even though the hopping rates are much higher overall in the simulation. For the simulation in Fig. 5.3, each ion has, on average, an excitation energy of $\sim 10^4\hbar\omega_y$, which is roughly comparable to the values in the experiment (see Sec. 4.4); however, in the simulation we are adjusting the excitation energy to get significant hopping within an easily simulated time rather than attempting to make a direct match to the hopping rates in the experiment. If we reduce the excitation energy, we could presumably obtain a hopping rate on par with that in the experiment (1-10 s^{-1} at the centre of the crystal). We will address the dependence on excitation energy in a later section.

Figure 5.3 shows only the axial motion of the ions during the simulation. In place of a separate plot of the transverse motion, Fig. 5.4 shows a stroboscopic plot of the 2-D locations of the ions for different ranges of time in the simulation. Figure 5.4(a) shows the initial behaviour of the ions during the time range of $t = 0 - 10$ μs. The motion of the ions still bears a strong resemblance to the initial transverse zigzag excitation, but some of the motion is already being transferred into the axial direction. As mentioned above,

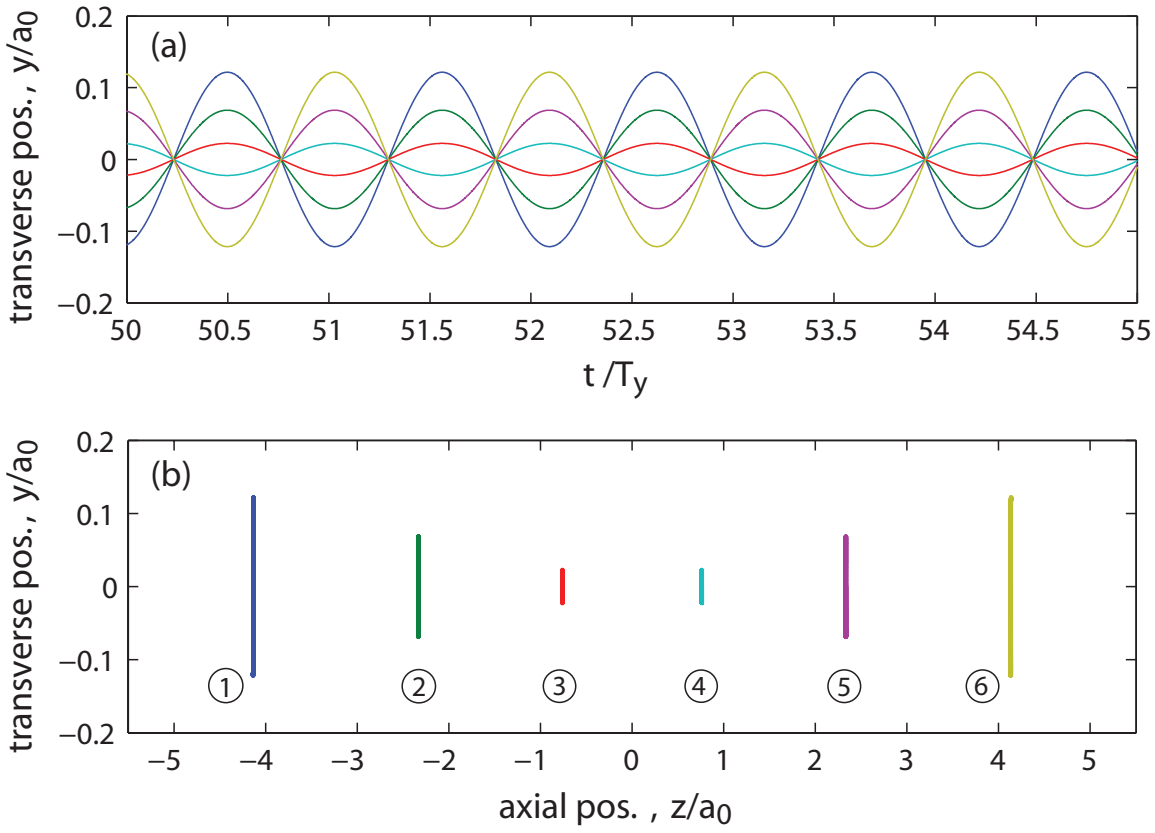

Figure 5.1: Molecular-dynamics simulation of the transverse bow-tie mode in a six-ion crystal. A small-amplitude initial displacement with excitation energy $\Delta E = 0.0177E_0$ is used to excited the mode. (a) Transverse positions of the ions as a function of time, showing the simple harmonic oscillator behaviour. Colors correspond to different ions. Positions are scaled to length a_0 (see text), and time is scaled to the transverse secular trap period $T_y = 2\pi/\omega_y$. The mode frequency determined from the simulation is $0.9406\omega_y$, consistent with the value of $0.9406\omega_y$ obtained from small-oscillation analysis. (b) Time sampling of the two-dimensional positions of the ions, showing their trajectories. Lengths are scaled to a_0.

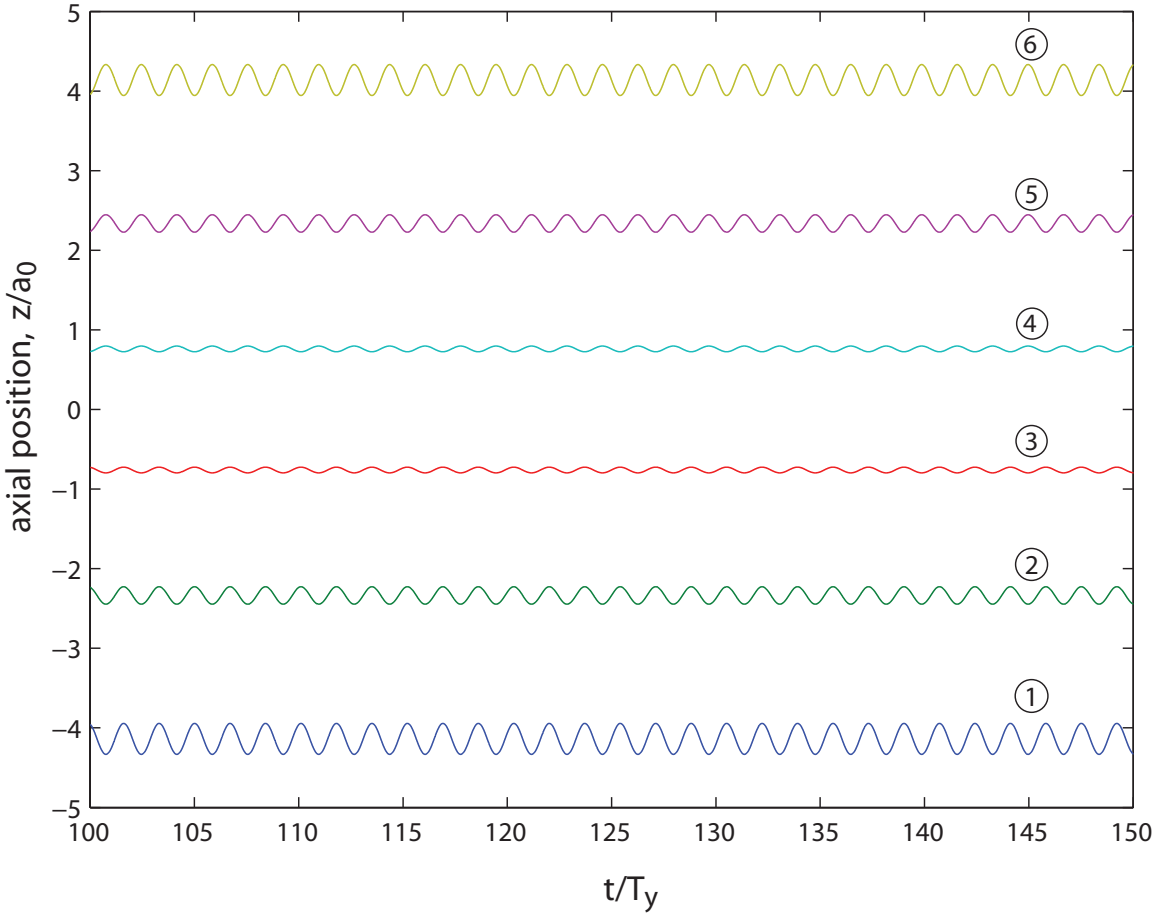

Figure 5.2: Molecular-dynamics simulation of a small-amplitude excitation of the axial bow-tie mode in a six-ion crystal. A small initial velocity kick with excitation energy $\Delta E = 0.0177E_0$ is used to excite the mode. Colors correspond to different ions. Positions are scaled to a_0 (see text) and time is scaled to the transverse secular trap period $T_y = 2\pi/\omega_y$. The mode frequency determined from the simulation is $0.5881\omega_y$, consistent with the value of $0.5880\omega_y$ obtained from small-oscillation analysis.

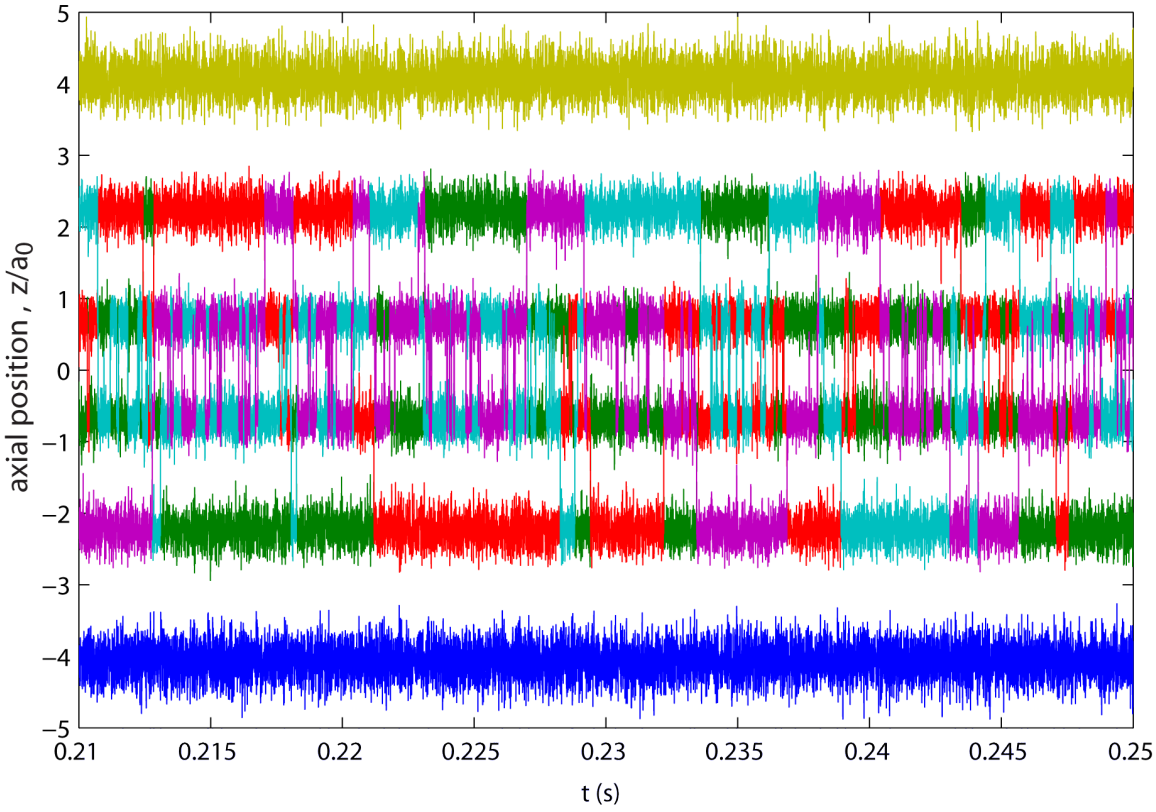

Figure 5.3: Simulated axial positions of the ions in a strongly excited six-ion crystal undergoing hopping between sites. An initial transverse zigzag displacement with excitation energy $\Delta E = 0.2870E_0$ is used to excite the ion-crystal. The trap asymmetry is $\alpha = 0.1152$ and the simulation step size is $\Delta t = T_y/1000$. For concreteness, the scaled simulation time has been converted into real units ($\Delta t = 2.346$ ns) by assuming a potential with secular trap frequencies of $\omega_y/2\pi = 426.26$ kHz and $\omega_z/2\pi = 144.7$ kHz for the transverse and axial direction, respectively. The trajectories of the ions are color-coded to allow the site-to-site hopping to be seen.

the nonlinearity at large amplitudes of oscillation leads to complex behaviour including coupling between the two axes of motion. In the subsequent Figs. 5.4(b)-(e), we show stroboscopic plots spanning times ranging from 0–50 μs to 0–1.1 s to illustrate the evolution of the spatial probability distribution of ions in the trap. After 2 ms (Fig. 5.4(d)), the initial coherent oscillation has been lost to "random" motion and the distribution is largely stable (compare to (e), where the sampling range is 0–1.1s).

In regard to the apparent randomness of the motion, we note in passing that Blumel *et al*. [18] have considered the motion for two ions in a 3-D harmonic potential and studied the onset of chaos using Poincare surfaces of section. We have not considered any such analysis. Our primary concern is that the hopping dynamics of the ion crystal at constant energy should not be artificially constrained by initial conditions. We use the zigzag transverse displacement as the initial excitation since it is closest to the final distribution in Fig. 5.4(e) (and to the shape of a thermal distribution), but we have verified that various initial conditions with the same energy lead to the same final distribution (see below).

The shape of the steady-state distribution in Fig. 5.4(e) is suggestive of the local potential experienced by the ions. The distribution is significantly wider in the transverse direction at the centre of the crystal, which is what one expects near α_{crit}. The regions of highest point-density correspond to the locations of lowest potential energy – the equilibrium positions for the ions. The empty regions between the clouds of points indicate the potential barriers that separate the sites. Each of the outer two clouds consists of only one color, pointing to the fact that no hopping happens there. The interior four sites however, are mixtures of points with different colors, meaning that as time goes by, one site is occupied by different ions. Here we also see some "tails" connecting the four inner clouds. These identify the passages for ions to hop from one site to another. The lower point-density in the tails indicates the higher potential energy there compared to the cloud centers, but, when hopping takes place, it is still easier for the ions to use these saddle potentials than to surmount the very high barriers (blank regions) between the clouds.

To illustrate the details of individual hopping events, Fig. 5.5(a) shows a magnified view of a small time interval from Fig. 5.3. As can be seen, the hopping events occur over a very short time scale, and it is clear that the hopping events are pairwise events involving only two ions (at this energy anyways). To look into how exactly the hopping takes place in two-dimensional space, one can trace the trajectories of the ions over a very short time

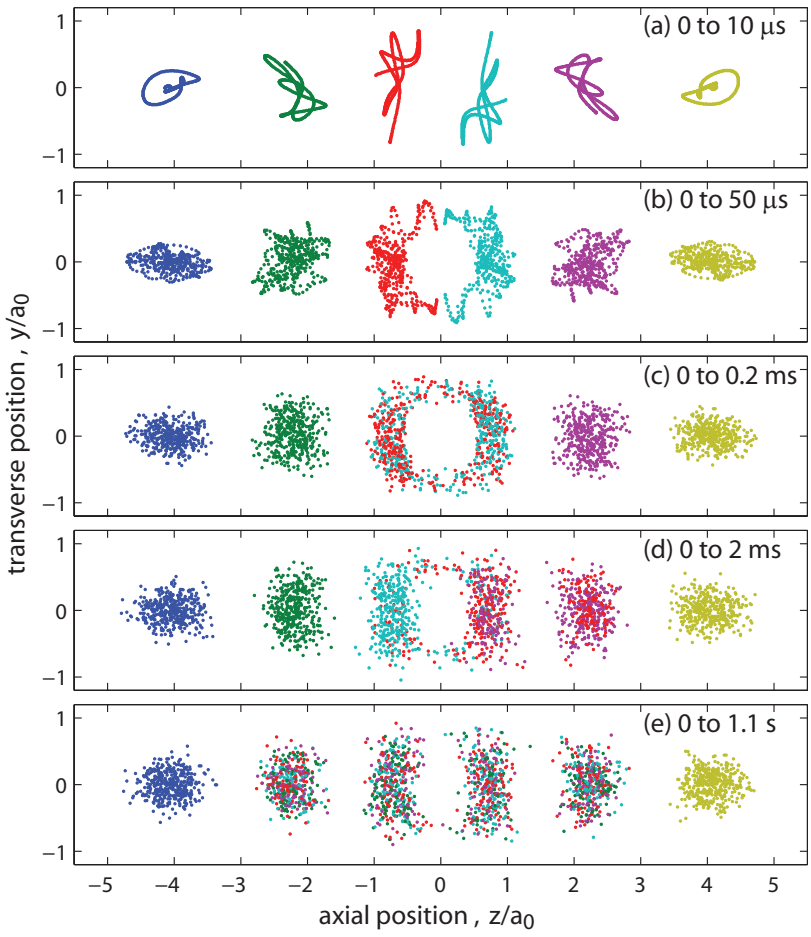

Figure 5.4: Time-sample of the ion positions in a strongly excited six-ion crystal undergoing hopping. Each of the plots consists of 400 sets of the six ions' positions evenly sampled through the time ranges as indicated. Simulation parameters are same as in Fig. 5.3. The distribution has already reached a steady state at 2 ms (d), as can be seen by comparison to (e).

near one of the hopping events. For a hopping event involving the centre two sites, as indicated in Fig. 5.5(a), the ions' trajectories are shown in Fig. 5.5(b). Consistent with the discussion before, the central two ions adopt a circle-like path which helps to keep their distance from each other and thus is energetically favorable. This is a general feature of the way hopping happens, and trajectories of the same kind are observed for hopping events at different times and between different sites.

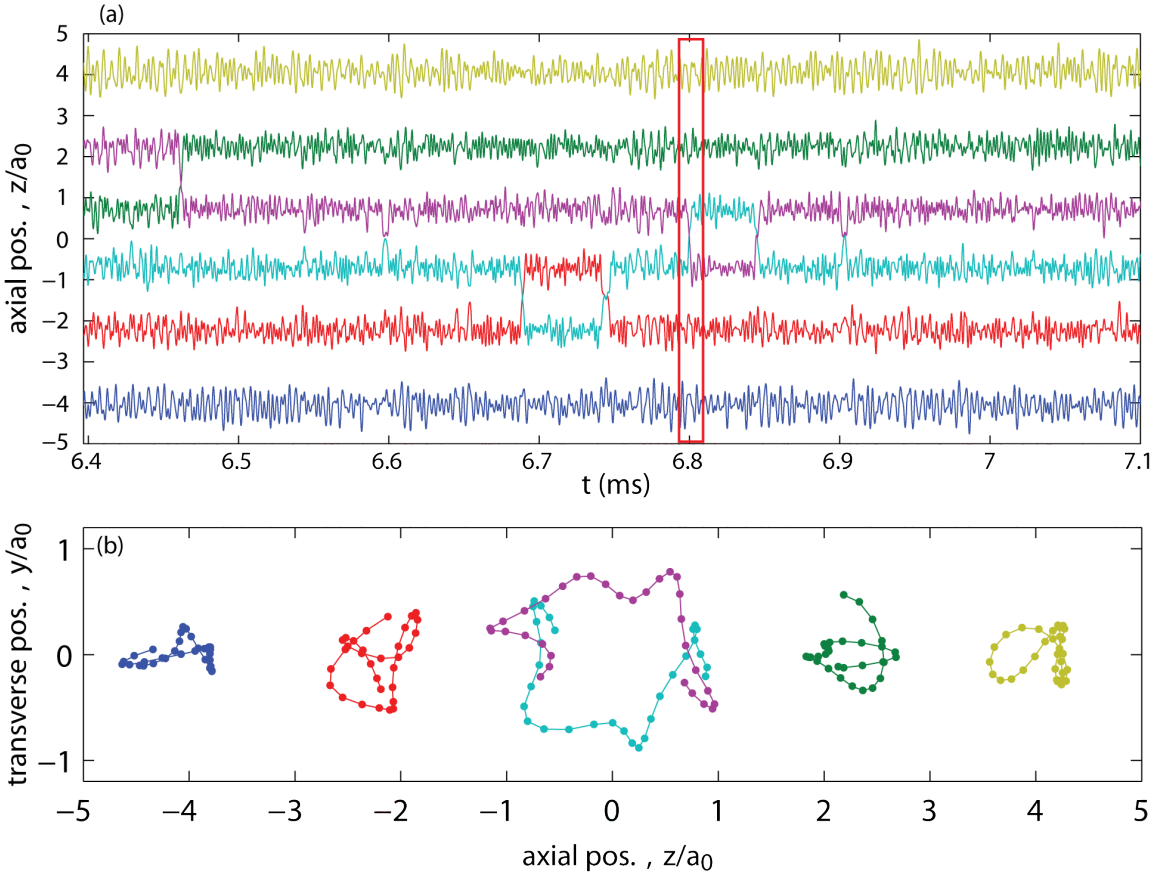

Figure 5.5: A hopping event in detail. (a) Magnified view of a small time interval in Fig. 5.3 to resolve a single hopping event, indicated by the boxed region. (b) Two-dimensional trajectory during the hopping event at around 6.803 ms indicated in (a) and involving two central ions. The trajectory points have a time interval of 7 μs. The direction of the central ions' paths is counter-clockwise.

5.3.2 Hopping characteristics from simulation

Like in the experiment, we are also interested in the statistics of where an ion will go in a hopping event. Extracting such data from the simulation requires a way to determine the site at which an ion is located at any time through the simulation. In Fig. 5.5(a), we see that, for most of the time, the ions are oscillating around the equilibrium positions that define each site, and the motion of the ions is well enough localized that their axial positions maintain the same order. Only when hopping happens do the ions change their positional order. Therefore, an easy way to define which sites the ions are at is simply to sort their positions: whichever ion has the smallest axial position is defined to be at site 1, and so on. Using such an algorithm, we extract the statistics of relocation for all hopping events in a 1-s simulation with the same parameters as in Fig. 5.3, and plot the results in Fig. 5.6(a). The hopping is observed to be concentrated at the centre of the crystal. Overall the distribution of hopping outcome is quite similar to the one we get from experiment – compare Fig. 4.9(b) – even though the hopping rate in the simulation has been chosen to be much higher. This seems to suggest that the simple simulation already captures the essence of the hopping behaviour in the experiment. It should be noted that to obtain higher statistics for Fig. 5.6(a), we are showing a combination of data from all four inner ions. Since these ions all move substantially between the inner four sites in the simulation (Fig. 5.3), we assume that the four ions are equivalent; that is, that the simulation time is long enough that the initial condition of an ion is a negligible effect. In fact, we have looked at the statistics for individual ions, and they all have distributions of the same characteristic shape.

Also, we notice in Fig. 5.6(a) that all the hopping events are between nearest neighbours, while, in the experiment, we observe hopping events that involve non-neighbouring sites. In fact, the finite camera frame rate in our experiment necessarily implies that a certain fraction of sequential nearest-neighbour hopping events in rapid succession will be regarded as one single non-nearest-neighbour hopping event. In Fig. 5.6(b), we show the same data in (a) but filtered with the camera exposure and readout mechanism, where roughly the same ratio of camera frame-rate to hopping rate as in the experiment is introduced. In this case, the outcome does show some non-nearest-neighbour hopping events. For example, 50 events are registered in the $3 \rightarrow 5$ hopping channel. However, this only

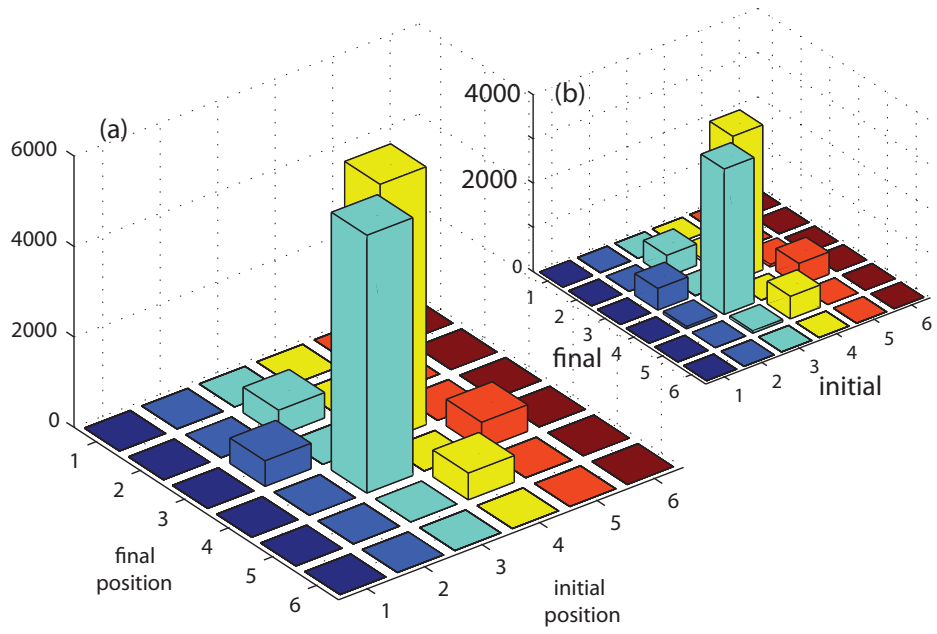

Figure 5.6: (a) Distribution of hopping outcome as a function of initial ion position in a crystal of six ions from MD simulation. The simulation parameters are the same as in Fig. 5.3. The total duration of the simulation is 1.09 s. (b) The same data in (a) but filtered with the camera mechanism, where the exposure time is set to 4.22×10^{-5} s and readout time set to 2.96×10^{-5} s.

corresponds to 1.3% of the total number of hopping events starting from site 3. On comparing with the experimental data of Fig. 4.9(b), it is apparent that the mechanism of the camera does not fully explain the behaviour observed in the experiment.

For the same 1-s simulation with parameters as in Fig. 5.3, we also assess the statistics of the dwell time at each site (that is, how long an ion stays in a certain site before hopping to a different one) in order to compare with the experiment data in Chp. 4. In Fig. 5.7, we plot the distributions of the dwell time for each of the inner four sites in the six-ion crystal. As before, we use the combined statistics from the trajectories of the four inner ions. The outer two sites are not shown due to lack of hopping there. A decreasing probability distribution towards longer dwell times is observed for each site. The distributions for the sites are also symmetric about the centre of the crystal, with the central two sites limited to much shorter dwell times. Exponential fits match the distributions reasonably well and give a decay constant of {1.94(6), 0.145(3), 0.144(3), 1.99(8)} ms for site 2 through site 5 respectively. For an exponential distribution, the decay constant corresponds to the average dwell time. The average dwell times for each site, as calculated directly from the raw data, are {1.937, 0.1741, 0.1734, 1.848} ms, matching the decay constants from the fits to 20% or better. It is interesting that the largest discrepancy occurs for the two interior sites with the largest hopping statistics and that the direction of the discrepancy is the same as that observed in the experiment, where the average dwell time typically exceeded the fit decay constant by a factor of 1.2–2 (see Sec. 4.3). Furthermore, the trend in the residuals for the interior two sites in Fig. 5.7 look remarkably similar to those observed for exponential fits to the experimental data (Fig. 4.6). How meaningful this is or not is not clear at this time. Overall, we can still say that the dwell-time distributions in both the simulation and the experiment are qualitatively consistent with exponential distributions with shorter average dwell times at the central sites.

Following Sec. 4.3, we continue to use the inverse of the average dwell time on a certain site to characterize the hopping rate there. In Fig. 5.8, we plot hopping rate as a function of crystal site for the six-ion simulation of Fig. 5.3. As already noted above, the hopping rate is sharply peaked at the centre of the crystal, consistent with what we have observed in the experiment. One difference in the simulation compared to the experiment is that the simulation shows a sharper peak – compare the right-hand column of Fig. 4.10 – and the peak gets even sharper for simulations where the hopping rate at the centre of the crystal

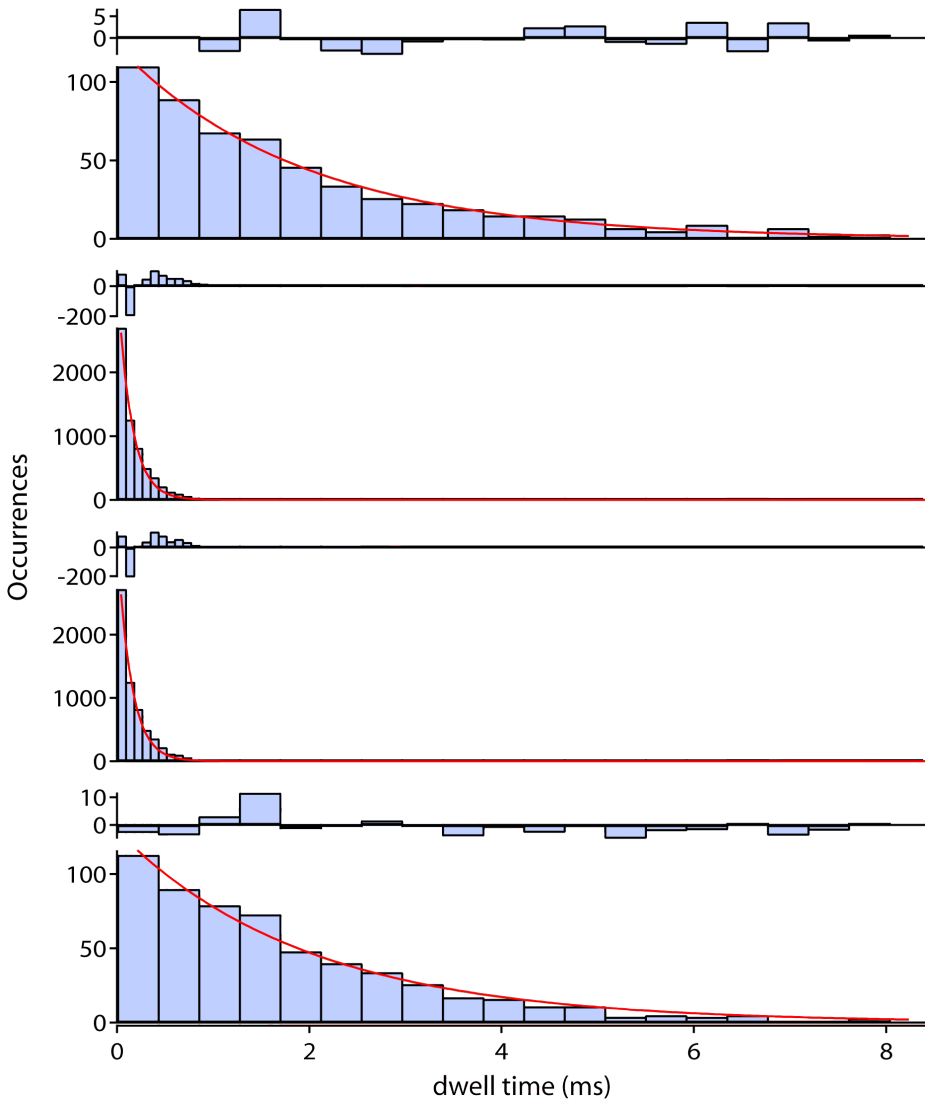

Figure 5.7: Distributions of dwell times for an ion at the central four sites of a six-ion crystal, as obtained from molecular dynamics simulation. The simulation parameters are the same as in Fig. 5.3 and the duration of the simulation is 1.09 s. Distributions for the outer two sites are not shown due to lack of statistics. Bin sizes are adjusted according to the amount of statistics to properly show the distributions. Exponential fits (shown in red) give time constants of {1.94(6), 0.145(3), 0.144(3), 1.99(8)} ms for site 2 through site 5.

approaches that in the experiment. A second difference is that the distribution of hopping rate in the simulation is symmetric about the centre of the crystal, which is expected since radiation pressure effects are not included. Again, it is worth noting that the hopping rate in the simulation has been chosen, for computational convenience, to be much faster than the experiment (by a factor of $\sim 10^3$), but our sole purpose here is to demonstrate qualitative features.

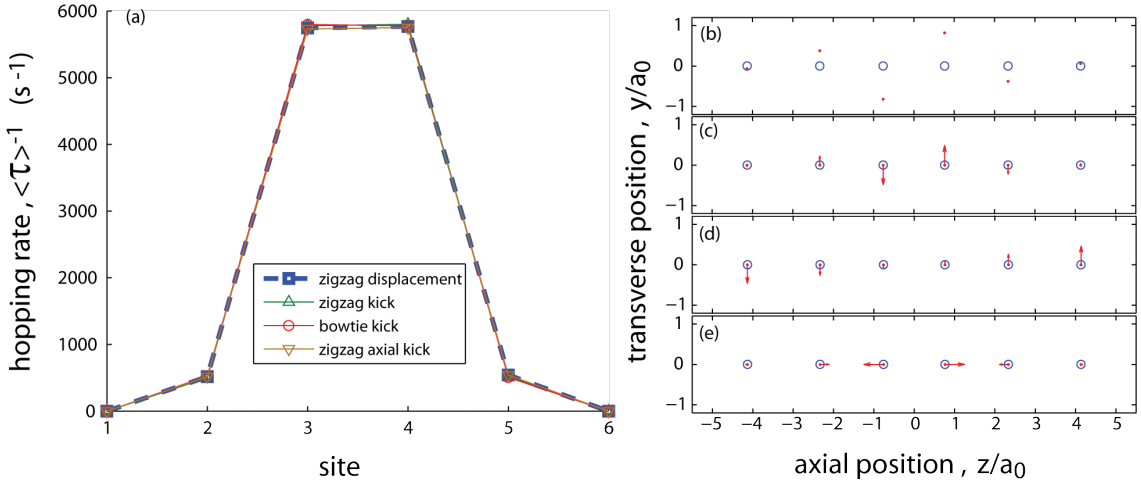

Figure 5.8: (a) Site-dependent hopping rate in a six-ion crystal, as obtained from molecular-dynamics simulation. Lines join the data-points to accentuate the spatial dependence. The four datasets shown in (a) correspond to different initial conditions used for excitation to demonstrate insensitivity of the simulation to initial conditions. The initial conditions are indicated in the legend and shown in (b)–(e) in the same vertical order as the legend. All excitations have the same excitation energy $\Delta E = 0.2870 E_0$. Other simulation parameters for the four datasets are the same as in Fig. 5.3. Total simulation time for all datasets is 1.09 s. The zigzag displacement in (b) is the same initial condition as used in Fig. 5.3.

As we have alluded to above, we expect the hopping characteristics presented so far to depend only on the excitation energy, and not the details of the initial condition for the MD simulation, for sufficiently long simulation times. The distribution of hopping rate in Fig. 5.8 provides a convenient quantitative test for sensitivity to initial conditions. Fig-

ure 5.8(b) shows the initial condition for the simulation of Fig. 5.3 and all the hopping results that we have presented so far. The displacement is applied to each ion to give a large excitation of the transverse zigzag mode. Separate simulations have been performed with different initial excitations as shown in Figs. 5.8(c) to (e) and the corresponding distributions of hopping rate are compared in Fig. 5.8(a). Figure 5.8(c) shows an excitation of the transverse zigzag mode but using an initial *velocity* kick, which is equivalent to exciting the mode at a different phase. Figure 5.8(d) and (e) show excitations of the transverse bowtie mode, and the axial zigzag mode, also using velocity kicks. Of course, the excitation energy for all these different initial conditions is chosen to be the same and in all cases no COM mode is excited. As can be seen in Fig. 5.8(a), the different initial conditions lead to nearly identical spatial distributions of hopping rate (with at most an 8% difference for sites 2 and 5, and a 0.5% difference for site 3 and 4). This makes sense because, at large amplitude of excitation, the different modes are coupled and energy is able to transfer between them. Based on the time evolution of the spatial distribution shown in Fig. 5.4, we expect any transient effects to be gone fairly quickly (in ~ 2 ms) compared to the typical 1-s duration of the simulations considered here.

5.3.3 Hopping as a function of control parameters

In the chapter so far, we have looked at the various characteristics of hopping in the simulation in analogy with what we have considered in the experiment. We have also seen that simulations with different initial conditions lead to the same site-dependent hopping rate as long as the same initial energy is used (and for the relatively high excitation energy used). Here, we move on to investigate how the hopping rate differs when the excitation energy is changed. The analogy in the experiment would be a study of hopping rate as a function of the laser-cooling parameters. The computation time required to repeat the simulation over a range of excitation energies would be substantial with our current simulation setup on a desktop computer. We leave a complete quantitative study for the future; however, we qualitatively compare a single simulation at a higher excitation energy of $\Delta E = 0.3796 E_0$ to the ones that we have already shown at $\Delta E = 0.2870 E_0$. This corresponds to an increase in the excitation energy by a factor of 1.32. The spatial distributions of hopping rate for the two excitation energies are compared in Fig. 5.9. Figure 5.9(a) is a direct comparison

of the rates at each site. We see that the higher excitation energy leads to a higher hopping rate for all sites, as expected. Quantitatively, the rate at the centre sites is 2.7 times higher, somewhat but not substantially higher than the factor of 1.32 increase in the excitation energy. The sensitivity of the hopping rate to the excitation energy is perhaps not as strong as we might have expected. To explore this further, we have also performed a simulation at an excitation energy, $\Delta E = 0.1435E_0$, which is a factor of two *lower* than the one that we have discussed in detail. We do not show the results here because of the low statistics in a 1-s simulation, but the hopping is indeed dramatically reduced to a rate of only $\sim 1-10$ s^{-1} for the central two ions. Ultimately, we need to consider more values of the excitation energy to see if the nonlinear response to the excitation energy can correctly account for the hopping rates observed in the experiment. Having said all this, what we see is consistent with the trend in the experiment of increasing hopping rate at higher excitation energy.

In Fig. 5.9(b), we normalize the spatial distributions of hopping rate for the two excitation energies to their respective peak values. This permits the widths of the distributions to be compared directly by eye, and it can be seen that the higher-energy case has a wider peak. Although not shown here, at even higher energies, the two ions on the outer edges of the crystal (sites 1 and 6) become involved in the hopping over the same simulation time, and simulations with quite low energy lead to hopping only between the centre two sites for the same simulation time. Therefore, the width of the peak does increase with higher energies, which is consistent with our expectation that there is a higher energy barrier to hopping at the outer sites of the crystal due to the larger ion spacing there. It is worth noting, however, that when the hopping rate in the simulation is tuned down to match that in the experiment, the simulation gives a narrower distribution of hopping rate compared to that in the experiment.

To conclude this section, we mention briefly the effect of the confining potential on the hopping. We have performed an MD simulation for six ions at $\alpha = 0.0695$ and with the same excitation energy as in Fig. 5.3. This value of α is far from α_{crit} for the zigzag transition and close to the lowest value used in the experiment data of Fig. 4.12. The simulation shows no hopping over the course of 1 s, consistent with the expectation that the hopping is enhanced as α approaches α_{crit}.

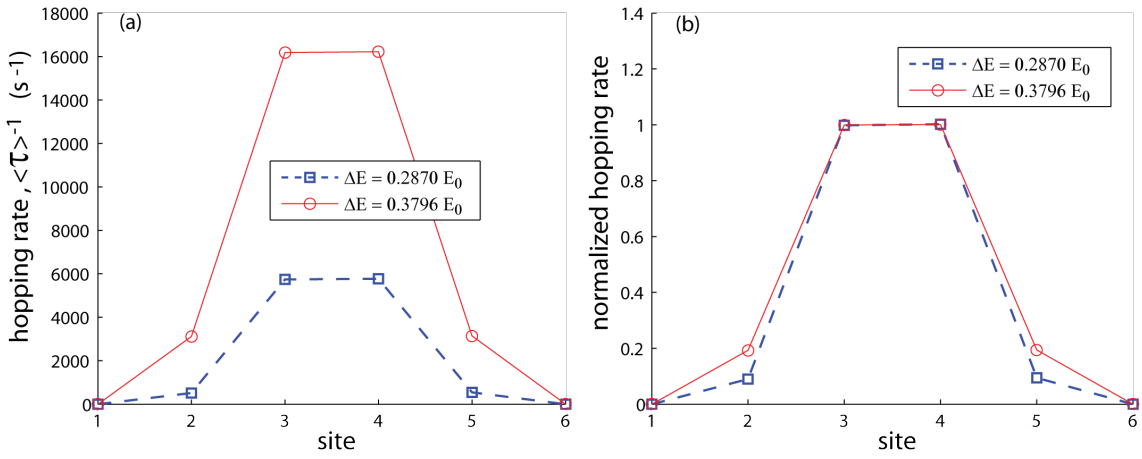

Figure 5.9: (a) Spatial distribution of hopping rate from simulations of a six-ion crystal with different initial excitation energies ΔE, as indicated in the legend. Other simulation parameters are the same as in Fig. 5.3. Total simulation time for all datasets is 1.09 s. (b) Spatial distribution of hopping rate, normalized to the peak value, for the two datasets shown in (a).

5.4 Simulation accuracy

We briefly discuss here the effect of time step on the simulations and accuracy of the solutions. A step size, dt_0, of $10^{-3}T_y$ or 2.346 ns has been used for all of the simulation results presented above. When the step size is decreased by a factor of 2 in the primary simulations used to study hopping (with $\Delta E = 0.2870E_0$), the solution does not reproduce the trajectories of the ions beyond a fairly short length of time ($\sim 100\ \mu$s, or $40T_y$), much less than the total simulation time of 1 s. A comparison between the two simulations with different step sizes shows that the difference in trajectories after the first time step (corresponding to the local error) is small (10^{-10} in scaled units) but diverges exponentially and results in a complete loss of global accuracy after a time, which we refer to as the 'divergence time', of about 100 μs. One can push the local error to lower values and the divergence time in the trajectories to somewhat later times by using a smaller dt; however, since the discrepancy in the trajectories grows exponentially, one cannot hope in practical terms to achieve an accurate trajectory for the long times necessary to assess hopping [70, 71].

In fact, for the initial condition shown in Fig. 5.8(c), a change of the step size from $10^{-1}T_y$ to $10^{-3}T_y$ suppresses the local error in the ion trajectories from 10^{-3} to 10^{-10}, and pushes the divergence time from 20 μs to 62 μs, corresponding to a factor of 3 improvement. Decreasing the step size by two decades further to $dt = 10^{-5}T_y$ yields a local error of 9×10^{-16}, already approaching the machine precision of 2.2×10^{-16}; however, this only improves the divergence time of the trajectories to 97 μs, about a factor of 1.6 larger than for $dt = 10^{-3}T_y$. Furthermore, two simulations differing in their initial conditions by the machine precision but with the same step size around the value $10^{-3}T_y$ are observed to diverge in their trajectories with unity global error reached at 140 μs. Therefore, we are unable in practical terms to achieve a divergence time much longer than 100 μs for simulations at the excitation energy $\Delta E = 0.2870E_0$.

The exponential instability in particle trajectories is a well known problem in molecular dynamics simulations [70, 71]. The non-linearity of the system itself prevents one from being able to follow a trajectory accurately over long times. This is a fundamental problem to any algorithm used to integrate the trajectory. However, many evidences suggest that one may still trust the statistical properties (such as the hopping rate in our case) even though the particle trajectories themselves are not reliable over long times [70, 71]. A comparison between simulations with step size of $10^{-3}T_y$ and half that value, again with the initial conditions in Fig. 5.8(c), already show hopping rates that match sufficiently closely for our purposes. The fractional discrepancies for the rates in the four interior sites are {0.70%, 0.42% -0.02%, -4.1%}, within the 1-σ uncertainty of {7.9%, 2.3%, 2.3%, 7.9%} expected from the amount of statistics available and assuming no correlations. It is worth noting as well that the total energy of the system, which affects the hopping rate, remains stable for the duration of the simulations, as noted in Sec. 5.2.

Since the divergence time and the average dwell time at the centre of the crystal are comparable in size for the simulations shown above at $\Delta E = 0.2870E_0$, we have performed one additional test at a lower excitation energy to check for any correlation between the divergence time and hopping rates. At an excitation energy of $\Delta E = 0.2296E_0$ where the central hopping rate is about 1800 Hz, roughly a factor of 3 lower than the central hopping rate at $\Delta E = 0.2870E_0$, the divergence time is only 1.6 times longer, suggesting that the divergence time and hopping rate are not correlated. In other words, the fact that the average dwell time at the centre of the crystal and the divergence time are of the same order for the

primary simulations presented in this chapter seems to be only a coincidence.

In conclusion, we have argued that long term accuracy of the ion trajectories is unattainable for practical purposes in the hopping simulations, and that the step size, dt_0, of $10^{-3}T_y$ is already sufficient to extract physically sensible results.

5.5 Discussion

From our simple, constant-energy simulations of a six-ion crystal, we find that hopping is activated with a large enough initial excitation and is enhanced near the critical α. We have assessed the characteristics of the hopping in the simulation and find several qualitative similarities to the experimental data of Chp. 4: the distribution of dwell times at each site follows a roughly exponential shape; the spatial distribution of hopping outcome shows a similar shape as in the experiment; and, finally, the spatial distribution of hopping rate shows a peak at the centre of the crystal. These similarities between the simple simulation and experiment suggest that technical issues including micro-motion, laser cooling and heating, and laser profile are not the primary determining factors in the hopping behaviour in the experiment, although such issues might contribute to the quantitative dependence of hopping on the laser and trap parameters.

For future work, with the current version of the simulation, tests with a range of initial excitation energy and trap anisotropies would be helpful. Beyond that, the rf trap could be included in the simulation to see how micro-motion affects the hopping. One should also bring in the laser cooling and heating mechanisms, including effects of the laser direction, laser profile and non-fluorescing impurity, in order to make a final comparison to the experiment.

Chapter 6

Conclusion

In this thesis, we have studied the hopping mobility in ion crystals in linear rf Paul traps. Our studies extend earlier ones with two ions to look at crystals of up to seven ions, the structure of which adds new features to the behaviour.

Our experimental technique involves tracking a distinguishable $^{172}Yb^{+}$ impurity in a crystal of $^{171}Yb^{+}$ ions. We have been able to resolve the hopping behaviour of the impurity into individual events, which allows us to extract a range of characteristics including the hopping rate at each crystal site, and the hopping destination. Using these techniques to assess the hopping, we have demonstrated that the hopping rate can be controlled by tuning the power and detuning of the Doppler-cooling laser applied to the $^{171}Yb^{+}$ ions. The laser parameters affect the average kinetic energy of the $^{171}Yb^{+}$ ions and in turn that of the $^{172}Yb^{+}$ impurity through sympathetic cooling. At kinetic energies approaching a significant fraction of the Coulomb interaction energy, the hopping is observed to be activated.

Analysis of the hopping statistics shows that the hopping rate is highest at the centre of the crystal. Hopping is also found to be enhanced when the anisotropy of the trap is tuned closed to the critical value for the zigzag structural phase transition. These two observations are consistent with an intrinsic cause related to the crystal structure and dynamics. When the transition is approached, the transverse zigzag mode tends to zero frequency and can have a large, thermally activated amplitude, leading to large transverse excursions and nonlinear dynamics at the centre of the ion crystal. Furthermore, the barrier to hopping is lowest at the centre of crystal due to the higher linear density of ions there.

Several technical complications, however, including micro-motion arising from the rf

potential, the non-uniform profile of the laser beam, and sympathetic cooling of the non-fluorescing impurity, may influence the outcome of the experiment. Although these factors may modify the quantitative dependence of the hopping on the laser and trap parameters, we argue that they are not the primary cause for the spatial distribution of hopping or the enhancement of the hopping near the zigzag transition. We lend evidence to this argument by performing a preliminary series of molecular dynamics simulations, in which we give an initial energy to an ion crystal in a harmonic potential and let the system evolve according to Newtonian dynamics. These simple simulations at constant energy remove many of the technical complications that are not easy to avoid in the experiment, but reproduce important qualitative features of the observed hopping behaviour: the shape of the distributions of dwell time at each site; the concentration of hopping at the centre of the crystal; and the enhancement of hopping near the zigzag transition.

In future experiments, it would be interesting to extend our studies to crystals with more ions, in particular to study how the on-site hopping rate depends on the size of the crystal, and to assess if the hopping persists as a phenomenon primarily between nearby sites. It would also be interesting to study the effect of a larger-mass impurity that can induce a substantial distortion in the centre of the crystal or to investigate the case with more than one impurity, where the average energy relies more on the sympathetic cooling. Using the current setup, it seems natural to proceed to study the thermal activation of the zigzag switching, which would be helpful in advance of related proposed experiments in the quantum regime [29, 27]. The thermal activation of the zigzag switching may also provide a means to investigate recent predictions for the temperature dependence of the structural phase transition [26].

Our molecular dynamics simulations can be improved by introducing the rf potentials to study the effect of the micro-motion of the trapped ions, and by introducing the interaction with the Doppler-cooling laser to investigate the role of the laser profile in hopping behaviour and the effect of sympathetic cooling on the impurity. To simulate hopping behaviour at a range of laser parameters and trap anisotropies, we envision the use of the parallel computer resources of WestGrid. The ultimate goal of these simulations is to make a direct comparison to our experiment and to provide insight for future related studies.

Bibliography

[1] F. Diedrich, E. Peik, J. M. Chen, W. Quint, and H. Walther. Observation of a phase transition of stored laser-cooled ions. *Phys. Rev. Lett.*, 59(26):2931–2934, Dec 1987.

[2] D. J. Wineland, J. C. Bergquist, Wayne M. Itano, J. J. Bollinger, and C. H. Manney. Atomic-ion coulomb clusters in an ion trap. *Phys. Rev. Lett.*, 59(26):2935–2938, Dec 1987.

[3] S. L. Gilbert, J. J. Bollinger, and D. J. Wineland. Shell-structure phase of magnetically confined strongly coupled plasmas. *Phys. Rev. Lett.*, 60(20):2022–2025, May 1988.

[4] G. Werth, V. N. Gheorghe, and F. G. Major. *Charged Particle Traps II Applications*. Springer-Verlag, 2009.

[5] J I Cirac and P Zoller. Quantum computation with cold, trapped ions. *Phys. Rev. Lett.*, 74(20):4091–4094, May 1995.

[6] D J Wineland, C Monroe, W M Itano, D Leibfried, B E King, and D M Meekhof. Experimental issues in coherent quantum-state manipulation of trapped atomic ions. *J. Res. Nat. Inst. Stand. Tech.*, 103:259–328, May 1998.

[7] A. Friedenauer, H. Schmitz, J. T. Glueckert, D. Porras, and T. Schaetz. Simulating a quantum magnet with trapped ions. *Nat Phys*, 4:757–761, Jul 2008.

[8] K. Kim, M.-S. Chang, S. Korenblit, R. Islam, E. E. Edwards, J. K. Freericks, G.-D. Lin, L.-M. Duan, and C. Monroe. Quantum simulation of frustrated ising spins with trapped ions. *Nature*, 465:590–593, Jun 2010.

[9] Daniel H. E. Dubin and T. M. O'Neil. Trapped nonneutral plasmas, liquids, and crystals (the thermal equilibrium states). *Rev. Mod. Phys.*, 71(1):87, Jan 1999.

[10] G Birkl, S Kassner, and H Walther. Multiple-shell structures of laser-cooled mg-24(+) ions in a quadrupole storage ring. *Nature*, 357(6376):310–313, May 28 1992.

[11] M. G. Raizen, J. M. Gilligan, J. C. Bergquist, W. M. Itano, and D. J. Wineland. Ionic crystals in a linear paul trap. *Phys. Rev. A*, 45(9):6493–6501, May 1992.

[12] M. Drewsen, C. Brodersen, L. Hornekær, J. S. Hangst, and J. P. Schifffer. Large ion crystals in a linear paul trap. *Phys. Rev. Lett.*, 81(14):2878–2881, Oct 1998.

[13] J. P. Schiffer. Phase transitions in anisotropically confined ionic crystals. *Phys. Rev. Lett.*, 70(6):818–821, Feb 1993.

[14] Daniel H. E. Dubin. Theory of structural phase transitions in a trapped coulomb crystal. *Phys. Rev. Lett.*, 71(17):2753–2756, Oct 1993.

[15] D. G. Enzer, M. M. Schauer, J. J. Gomez, M. S. Gulley, M. H. Holzscheiter, P. G. Kwiat, S. K. Lamoreaux, C. G. Peterson, V. D. Sandberg, D. Tupa, A. G. White, R. J. Hughes, and D. F. V. James. Observation of power-law scaling for phase transitions in linear trapped ion crystals. *Phys. Rev. Lett.*, 85(12):2466–2469, Sep 2000.

[16] R Blumel, J M Chen, E Peik, W Quint, W Schleich, YR Shen, and H Walther. Phase-transitions of stored laser-cooled ions. *Nature*, 334(6180):309–313, Jul 28 1988.

[17] J. Hoffnagle, R. G. DeVoe, L. Reyna, and R. G. Brewer. Order-chaos transition of two trapped ions. *Phys. Rev. Lett.*, 61(3):255–258, Jul 1988.

[18] R. Blümel, C. Kappler, W. Quint, and H. Walther. Chaos and order of laser-cooled ions in a paul trap. *Phys. Rev. A*, 40(2):808–823, Jul 1989.

[19] R. G. Brewer, J. Hoffnagle, and R. G. DeVoe. Transient two-ion chaos. *Phys. Rev. Lett.*, 65(21):2619–2622, Nov 1990.

[20] D Leibfried, R Blatt, C Monroe, and D Wineland. Quantum dynamics of single trapped ions. *Rev. Mod. Phys.*, 75:281, Mar 2003.

[21] K Abich, A Keil, D Reiss, Ch Wunderlich, W Neuhauser, and P E Toschek. Thermally activated hopping of two ions trapped in a bistable potential well. *J. Opt. B: Quantum Semiclass. Opt.*, 6(3):S18, 2004.

[22] D Kielpinski, B E King, C J Myatt, C A Sackett, Q A Turchette, W M Itano, C Monroe, D J Wineland, and W H Zurek. Sympathetic cooling of trapped ions for quantum logic. *Phys. Rev. A*, 61:032310, March 2000.

[23] Shmuel Fishman, Gabriele De Chiara, Tommaso Calarco, and Giovanna Morigi. Structural phase transitions in low-dimensional ion crystals. *Phys. Rev. B*, 77(6):064111, Feb 2008.

[24] In principle an optically pumped $^{171}Yb^{+}$ ion may be used but is less convenient.

[25] J. Liang and P. C. Haljan. Hopping of an impurity defect in ion crystals in linear traps. *Phys. Rev. A*, 83:063401, Jun 2011.

[26] Zhe-Xuan Gong, G.-D. Lin, and L.-M. Duan. Temperature-driven structural phase transition for trapped ions and a proposal for its experimental detection. *Phys. Rev. Lett.*, 105(26):265703, Dec 2010.

[27] H. Landa, S. Marcovitch, A. Retzker, M. B. Plenio, and B. Reznik. Quantum coherence of discrete kink solitons in ion traps. *Phys. Rev. Lett.*, 104:043004, Jan 2010.

[28] Gabriele De Chiara, Adolfo del Campo, Giovanna Morigi, Martin B Plenio, and Alex Retzker. Spontaneous nucleation of structural defects in inhomogeneous ion chains. *New Journal of Physics*, 12(11):115003, 2010.

[29] A. Retzker, R. C. Thompson, D. M. Segal, and M. B. Plenio. Double well potentials and quantum phase transitions in ion traps. *Phys. Rev. Lett.*, 101(26):260504, Dec 2008.

[30] P K Ghosh. *Ion Traps*. Clarendon Press, Oxford, 1995.

[31] S. Ejtemaee, R. Thomas, and P. C. Haljan. Optimization of Yb^{+} fluorescence and hyperfine-qubit detection. *Phys. Rev. A*, 82(6):063419, Dec 2010.

[32] D. J. Berkeland and M. G. Boshier. Destabilization of dark states and optical spectroscopy in zeeman-degenerate atomic systems. *Phys. Rev. A*, 65(3):033413, Feb 2002.

[33] S. Olmschenk, K. C. Younge, D. L. Moehring, D. N. Matsukevich, P. Maunz, and C. Monroe. Manipulation and detection of a trapped Yb^+ hyperfine qubit. *Phys. Rev. A*, 76(5):052314, Nov 2007.

[34] D. J. Berkeland, J. D. Miller, J. C. Bergquist, W. M. Itano, and D. J. Wineland. Laser-cooled mercury ion frequency standard. *Phys. Rev. Lett.*, 80(10):2089–2092, Mar 1998.

[35] D James. Quantum dynamics of cold trapped ions with applications to quantum computing. Jul 1998.

[36] D G Enzer, M M Schauer, J J Gomez, M S Gulley, M H Holzscheiter, P G Kwiat, S K Lamoreaux, C G Peterson, V D Sandberg, D Tupa, A G White, and R J Hughes. Observation of power-law scaling for phase transitions in linear trapped ion crystals. *Phys. Rev. Lett.*, 85:2466–2469, Sep 2000.

[37] H. Lehmitz, J. Hattendorf-Ledwoch, R. Blatt, and H. Harde. Population trapping in excited yb ions. *Phys. Rev. Lett.*, 62(18):2108–2111, May 1989.

[38] A. Bauch, D. Schnier, and Chr. Tamm. Collisional population trapping and optical deexcitation of ytterbium ions in a radiofrequency trap. *J. Mod. Opt.*, 39(2):0950–0340, Aug 1992.

[39] M. M. Schauer, J. R. Danielson, A.-T. Nguyen, L.-B. Wang, X. Zhao, and J. R. Torgerson. Collisional population transfer in trapped Yb^+ ions. *Phys. Rev. A*, 79(6):062705, Jun 2009.

[40] Stig Stenholm. The semiclassical theory of laser cooling. *Rev. Mod. Phys.*, 58:699–739, Jul 1986.

[41] W. Neuhauser, M. Hohenstatt, P. Toschek, and H. Dehmelt. Optical-sideband cooling of visible atom cloud confined in parabolic well. *Phys. Rev. Lett.*, 41:233–236, Jul 1978.

[42] D J Wineland and W M Itano. Laser cooling. *Physics Today*, 40(6):2–8, Jun 1987.

[43] F Diedrich, J C Bergquist, W M Itano, and D J Wineland. Laser cooling to the zero-point energy of motion. *Phys. Rev. Lett.*, 62(14):403–406, Oct 1989.

[44] D J Wineland and W M Itano. Laser cooling of atoms. *Phys. Rev. A*, 20(4):1521–1540, Oct 1979.

[45] Wayne M. Itano and D. J. Wineland. Laser cooling of ions stored in harmonic and penning traps. *Phys. Rev. A*, 25(1):35–54, Jan 1982.

[46] J. Javanainen. Light-pressure cooling of trapped ions in three dimensions. *Appl. Phys. A*, 23:175–182, Jun 1980.

[47] The heavy particle limit places an additional requirement on the thermal energy of the ion, which our experiment satisfies even at $k_B T/\hbar\omega_y \sim 10^4$.

[48] Ji Cirac, Lj Garay, R Blatt, As Parkins, and P Zoller. Laser cooling of trapped ions: The influence of micromotion. *Physical Review A*, 49(1):421–432, 1994.

[49] J. Javanainen and S. Stenholm. Laser cooling of trapped particles i: The heavy particle limit. *Applied Physics A: Materials Science & Processing*, 21:283–291, Mar 1980. 10.1007/BF00886180.

[50] Giovanna Morigi and Jürgen Eschner. Doppler cooling of a coulomb crystal. *Phys. Rev. A*, 64:063407, Nov 2001.

[51] D. J. Larson, J. C. Bergquist, J. J. Bollinger, Wayne M. Itano, and D. J. Wineland. Sympathetic cooling of trapped ions: A laser-cooled two-species nonneutral ion plasma. *Phys. Rev. Lett.*, 57(1):70–73, Jul 1986.

[52] P. Bowe, L. Hornekær, C. Brodersen, M. Drewsen, J. S. Hangst, and J. P. Schiffer. Sympathetic crystallization of trapped ions. *Phys. Rev. Lett.*, 82(10):2071–2074, Mar 1999.

[53] S. Ejtemaee. A fluorescence study of single trapped ytterbium ions for quantum information applications. *Simon Fraser University Thesis*, Fall 2010.

[54] Chr. Balzer, A. Braun, T. Hannemann, Chr. Paape, M. Ettler, W. Neuhauser, and Chr. Wunderlich. Electrodynamically trapped Yb^+ ions for quantum information processing. *Phys. Rev. A*, 73(4):041407, Apr 2006.

[55] Pierre Dubé and Michael Trinczek. Hyperfine-structure splittings and absorption strengths of molecular-iodine transitions near the trapping frequencies of francium. *J. Opt. Soc. Am. B*, 21(6):1113–1126, Jun 2004.

[56] Kazuhiko Sugiyama and Jun Yoda. Production of YbH^+ by chemical reaction of Yb^+ in excited states with H_2 gas. *Phys. Rev. A*, 55(1):R10–R13, Jan 1997.

[57] D. J. Berkeland, J. D. Miller, J. C. Bergquist, W. M. Itano, and D. J. Wineland. Minimization of ion micromotion in a paul trap. 83(10):5025–5033, 1998.

[58] W. Nagourney, G. Janik, and H. Dehmelt. Linewidth of single laser-cooled 24Mg+ ion in radiofrequency trap. *Proc. Natl. Acad. Sci. U.S.A.*, 80(2):643–646, 1983.

[59] In principle an optically pumped $^{171}Yb^+$ ion may be used but is less convenient.

[60] A good estimate of the average dwell time can also be obtained with fewer statistics than are required to elucidate and to fit the distribution of dwell times.

[61] W. Alt, M. Block, P. Seibert, and G. Werth. Spatial separation of atomic states in a laser-cooled ion crystal. *Phys. Rev. A*, 58(1):R23–R25, Jul 1998.

[62] G. Morigi and H. Walther. Two-species coulomb chains for quantum information. *Eur. Phys. J. D*, 13(2):261–269, 2001.

[63] J Javanainen. Light-induced motion of trapped ions. ii. arbitrary intensity. *J. Phys. B: Atom. Mol. Phys.*, 14(21):4191, Nov 1981.

[64] Giovanna Morigi and Jürgen Eschner. Is an ion string laser-cooled like a single ion? *Journal of Physics B: Atomic, Molecular and Optical Physics*, 36(5):1041, Mar 2003.

[65] A transverse voltage bias of up to $\sim$20 mV that introduces micromotion but no effect on the cooling laser does not show an observable effect on the hopping.

[66] Vladimir L. Ryjkov, XianZhen Zhao, and Hans A. Schuessler. Simulations of the rf heating rates in a linear quadrupole ion trap. *Phys. Rev. A*, 71:033414, Mar 2005.

[67] R. Casdorff and R. Blatt. Ordered structures and statistical properties of ion clouds stored in a paul trap. *Applied Physics B: Lasers and Optics*, 45:175–182, 1988.

[68] M. Marciante, C. Champenois, A. Calisti, J. Pedregosa-Gutierrez, and M. Knoop. Ion dynamics in a linear radio-frequency trap with a single cooling laser. *Phys. Rev. A*, 82:033406, Sep 2010.

[69] http://people.sc.fsu.edu/∼jburkardt/m_src/md/md.html.

[70] Michael Griebel, Stephan Knapek and Gerhard Zumbusch. *Numerical Simulation in Molecular Dynamics*. Springer, 2007.

[71] Daan Frenkel and Berend Smit. *Understanding Molecular Simulation: From Algorithms to Applications*. Academic Press, 2002.